CENTRAL RESEARCH LIBRARY
DOCUMENT COLLECTION

OAK RIDGE NATIONAL LABORATORY
operated by
UNION CARBIDE CORPORATION
NUCLEAR DIVISION
for the
U.S. ATOMIC ENERGY COMMISSION

LOCKHEED MARTIN ENERGY RESEARCH LIBRARIES
3 4456 0513753 5

ORNL-TM-2617

cy 1.

PHOTOELECTRIC DETERMINATION OF ELECTRON ATTENUATION LENGTHS IN MAGNESIUM AND ALUMINUM

(Thesis)

T. F. Gesell and E. T. Arakawa

OAK RIDGE NATIONAL LABORATORY
CENTRAL RESEARCH LIBRARY
DOCUMENT COLLECTION
LIBRARY LOAN COPY
DO NOT TRANSFER TO ANOTHER PERSON
If you wish someone else to see this document, send in name with document and the library will arrange a loan.
UCN-7969
(3 3-67)

Submitted by T. F. Gesell as a dissertation to the Graduate School of the University of Tennessee in partial fulfillment of the requirements for the degree of Doctor of Philosophy.

This report was prepared as an account of work sponsored by the United States Government. Neither the United States nor the United States Atomic Energy Commission, nor any of their employees, nor any of their contractors, subcontractors, or their employees, makes any warranty, express or implied, or assumes any legal liability or responsibility for the accuracy, completeness or usefulness of any information, apparatus, product or process disclosed, or represents that its use would not infringe privately owned rights.

ORNL-TM-2617

Contract No. W-7405-eng-26

HEALTH PHYSICS DIVISION

PHOTOELECTRIC DETERMINATION OF ELECTRON ATTENUATION LENGTHS IN MAGNESIUM AND ALUMINUM

T. F. Gesell and E. T. Arakawa

Submitted by T. F. Gesell as a dissertation to the
Graduate School of the University of Tennessee
in partial fulfillment of the requirements
for the degree of
Doctor of Philosophy

JUNE 1971

OAK RIDGE NATIONAL LABORATORY
Oak Ridge, Tennessee
operated by
UNION CARBIDE CORPORATION
for the
U.S. ATOMIC ENERGY COMMISSION

LOCKHEED MARTIN ENERGY RESEARCH LIBRARIES

3 4456 0513753 5

ACKNOWLEDGEMENTS

The author would like to express his gratitude for the thoughtful leadership provided by Dr. E. T. Arakawa during the course of this research. The special interest shown by Drs. T. A. Callcott, R. H. Ritchie, J. C. Ashley, R. D. Birkhoff, and R. N. Compton is also deeply appreciated. Gratitude is expressed for the computational aid provided by Dr. R. N. Hamm, Mr. V. E. Anderson, and Mrs. Betty McGill and for the technical support afforded by J. A. Harter. The author is indebted to Mrs. Beverly Varnadore for technical help in the preparation of the manuscript.

The patience and understanding shown by the author's wife, Diane, has helped to make the work enjoyable.

The author is grateful for financial support provided by the Atomic Energy Commission and by the U. S. Public Health Service.

ABSTRACT

A model for volume photoemission is given which relates photoelectron energy distributions and yields to a number of parameters. The parameters are the thickness, optical constants, and densities of states of the photoemitter, the optical constants of the substrate, the wavelength, polarization and angle of incidence of the exciting radiation, and an energy dependent electron attenuation length. Two methods for obtaining the electron attenuation length are given.

Near normal incidence reflectance measurements on magnesium ($2 \leq h\nu \leq 12$ eV) are given together with an interpretation based upon the Drude model and surface plasmon excitation.

Absolute photoelectric yield measurements on magnesium are given as a function of photon energy ($6 \leq h\nu \leq 12$ eV). A strong peak just below the surface plasmon energy is attributed to surface plasmon-one electron transitions. Photoelectron energy distributions ($7.5 \leq h\nu \leq 15$ eV) are given for magnesium. Distributions taken at lower energies are reminiscent of the expected parabolic density of states of magnesium while distributions taken at higher energies are dominated by large numbers of scattered electrons.

Experimental electron attenuation lengths are obtained for magnesium in the 5-11 eV range and for aluminum in the 11-19 eV range. The attenuation lengths are obtained by analyzing reflectance, yield and

energy distribution data. In addition, measurements of the relative photoelectric yield of aluminum as a function of angle are analyzed to obtain the attenuation length for all electrons photoemitted by 21.2 eV photons. Reasonable agreement with theory is found for attenuation length measurements provided the energy of the exciting radiation is well removed from the surface plasmon energy of the metal under study. Differences between the theory and data taken with photon energies near the surface plasmon energy are shown to be due to surface plasmon-one electron transitions.

Photoelectric yield measurements taken as a function of wavelength and angle upon a thin magnesium film are analyzed to obtain a bulk plasma energy of 10.46 eV.

It is shown that a fresh magnesium surface will emit electrons in the absence of light when exposed to low pressures of oxygen or water vapor.

TABLE OF CONTENTS

CHAPTER	PAGE
I. INTRODUCTION	1
II. THEORETICAL CONSIDERATIONS	6
Introduction	6
A Model for Volume Photoemission	7
Extraction of the Attenuation Length	33
Theoretical Attenuation Lengths	38
Non-ideal Surface Effects	48
Photoelectric Manifestation of the Optical Plasma Resonance	58
Recent Advances in Photoemission Theory	62
III. EXPERIMENTAL APPARATUS	63
General Considerations	63
Sources of Radiation	65
Monochromator	68
The Beam Monitor	69
The Window Assembly	69
The Experimental Chamber	73
Electronic Equipment	76
Additional Equipment	80
IV. EXPERIMENTAL PROCEDURES	82
General Considerations	82
Preliminary Preparations	85

CHAPTER PAGE

Measurement of Reflection 91

Simultaneous Measurement of Reflectance and Absolute Yield . . 92

Measurement of Photoelectron Energy Distribution Curves. . . . 93

Relative Yield of a Thin Sample 95

Relative Yield of a Thick Sample 96

V. RESULTS AND DISCUSSION 98

Introduction 98

Temporal Effects 99

Reflectance, Yield, and Energy Distribution Measurements of Magnesium 106

Electron Attenuation Lengths 124

Photoelectric Manifestation of the Optical Plasmon Resonance . . 146

VI. SUMMARY AND CONCLUSIONS 149

Theoretical Results 149

Apparatus 149

Contamination Measurements 150

Reflectance, Yield, and Energy Distribution Measurements . . . 150

Attenuation Lengths 152

Photoelectric Manifestation of the Optical Plasma Resonance . . 152

Exo-Electron Emission from Magnesium 153

BIBLIOGRAPHY 154

APPENDIX 161

LIST OF FIGURES

FIGURE PAGE

1. Electron flux spectrum from ^{64}Cu beta rays absorbed in aluminum 2
2. Diagram of the optical configuration 9
3. Diagram for the photoelectric model 13
4. Diagram for the simple photoelectric excitation model 24
5. Band structure and density of states for a simple metal 30
6. Theoretical internal densities of excited electrons for a simple metal 34
7. Theoretical external electron energy distributions for a simple metal. 35
8. Theoretical electron-electron mean free paths for a free electron gas with the parameters of aluminum. 41
9. Theoretical mean free paths for electron-electron scattering, electron-plasmon scattering and the effective mean free path for both types of scattering for a free electron gas with the parameters of aluminum. 44
10. Dispersion relations for the radiative and non-radiative surface modes in a semi-infinite free electron gas. 46
11. Theoretical probability that an electron will excite a non-radiative surface plasmon upon entering a semi-infinite free electron gas with the parameters of aluminum from a vacuum. 47

FIGURE PAGE

12. Theoretical change in reflectance due to diffuse scatter and surface plasmon absorption of a free electron gas with the parameters of magnesium 59

13. Top view of the experimental apparatus 64

14. Schematic diagram of the light source. 66

15. Schematic diagram of the light source power supply 67

16. Transmission characteristics of lithium fluoride, indium, tin and aluminum windows 71

17. Side view of experimental chamber 74

18. Illustration of ac differentiation 77

19. Circuit diagram for ac measuring circuit 79

20. Circuit diagram for retarding voltage control 81

21. Photoelectron energy distributions as a function of time for magnesium (10.2 eV). 100

22. Photoelectron energy distributions as a function of time for magnesium ($h\nu$ = 7.65 eV) 101

23. Photoelectric work function of evaporated magnesium films as a function of time-pressure 104

24. Total yield for magnesium at $h\nu$ = 10.2 eV as a function of time for various gases admitted to the vacuum system 105

FIGURE PAGE

25. Near normal incidence reflectance of magnesium in the 2-12 eV range 107

26. Experimental decrease in the reflectance of magnesium due to surface plasmon absorption for three films together with a theoretical fit to each 110

27. Photoelectric yield for magnesium as a function of photoelectron energy and time 112

28. Simultaneously measured yield and reflectance data for magnesium 115

29. Photoelectron energy distributions taken as a function of time for magnesium ($h\nu$ = 10.2 eV) in the improved apparatus 118

30. Photoelectric energy distributions taken at various photon energies and normalized to total yield 119

31. Unnormalized photoelectron energy distributions for magnesium at various photon energies taken in the University of Tennessee apparatus 120

32. Photoelectron energy distributions for magnesium taken at energies above the LiF cut off together with energy distributions taken at the lower energies 122

33. Attenuation length for electrons in magnesium as a function of energy above the Fermi level obtained from the absolute yield model 127

FIGURE PAGE

34. Attenuation length for electrons in magnesium as a function of energy above the Fermi level obtained by comparing experimental and theoretical energy distribution curves 130

35. Attenuation length for electrons in aluminum as a function of energy above the Fermi level obtained from the absolute yield model. 131

36. Thickness dependence of the relative photoelectric yield as a function of angle for aluminum 135

37. Dependence of the attenuation length obtained by fitting aluminum data with the angle model upon the parameters of the model 136

38. The relative yield as a function of angle for two aluminum films together with the best three parameter absolute least squares fit plus calculated curves for $\ell = 1$ Å and $\ell = 20$ Å for comparison 139

39. The relative yield as a function of angle for an aluminum film together with the best two parameter absolute least squares fit plus calculated curves for longer attenuation lengths for comparison 140

40. Attenuation lengths for electrons in aluminum as a function of electron energy above the Fermi level obtained from the angle method and the absolute yield method plus the experimental results of other investigators. 144

FIGURE PAGE

41. Energy of the peak in the photoelectric plasmon resonance as a function of $\tan^2\theta$ together with the results of other investigators 148

42. Side view of the experimental apparatus used for exo-electron emission studies 165

43. Time development of exo-electron emission from magnesium in the presence of oxygen for various pressures 166

44. Time development of the work function and the exo-electron emission and of the photoemission ($h\nu = 1.93 \pm .05$ eV) from a fresh magnesium surface 168

45. Time to achieve a monolayer of oxygen on a surface as a function of pressure assuming until sticking coefficient together with data which show the position in time of the first peak in the oxygen emission curves as a function of pressure 170

46. The effect of shutting off and reopening the oxygen leak upon the time development of exo-electron emission 171

47. Time development of exo-electron emission in the presence of water vapor for various pressures 172

CHAPTER I

INTRODUCTION

Studies in radiation physics can be conveniently grouped into 1) the study of the sources and characteristics of electromagnetic and the various particulate radiations and 2) the study of the interactions of the various types of radiation with matter. The former is largely the province of the nuclear physicist while the latter is investigated by several branches of physics, biology, and chemistry.

One outstanding feature of the interaction of radiation with matter is the large number of secondary, tertiary and higher order electrons generated by the primary radiation. Figure 1 shows the experimental and theoretical electron flux spectrum generated by ^{64}Cu beta rays absorbed in aluminum (Spencer and Fano, 1954; McConnell et al., 1968). The high energy portion of the curve represents the primary flux of beta particles. The feature of interest for our purposes is that the flux of electrons with energies in the 10-20 eV range is over 10^4 times greater than the primary flux. Thus the study of the interaction of low energy electrons with matter is very important and is as much a part of radiation physics as the study of sources of radiation and primary interactions.

It is desirable to know the physical mechanisms by which low energy electrons interact with matter and to know with what probability a given type of interaction will occur. For volume processes, specification of the mean

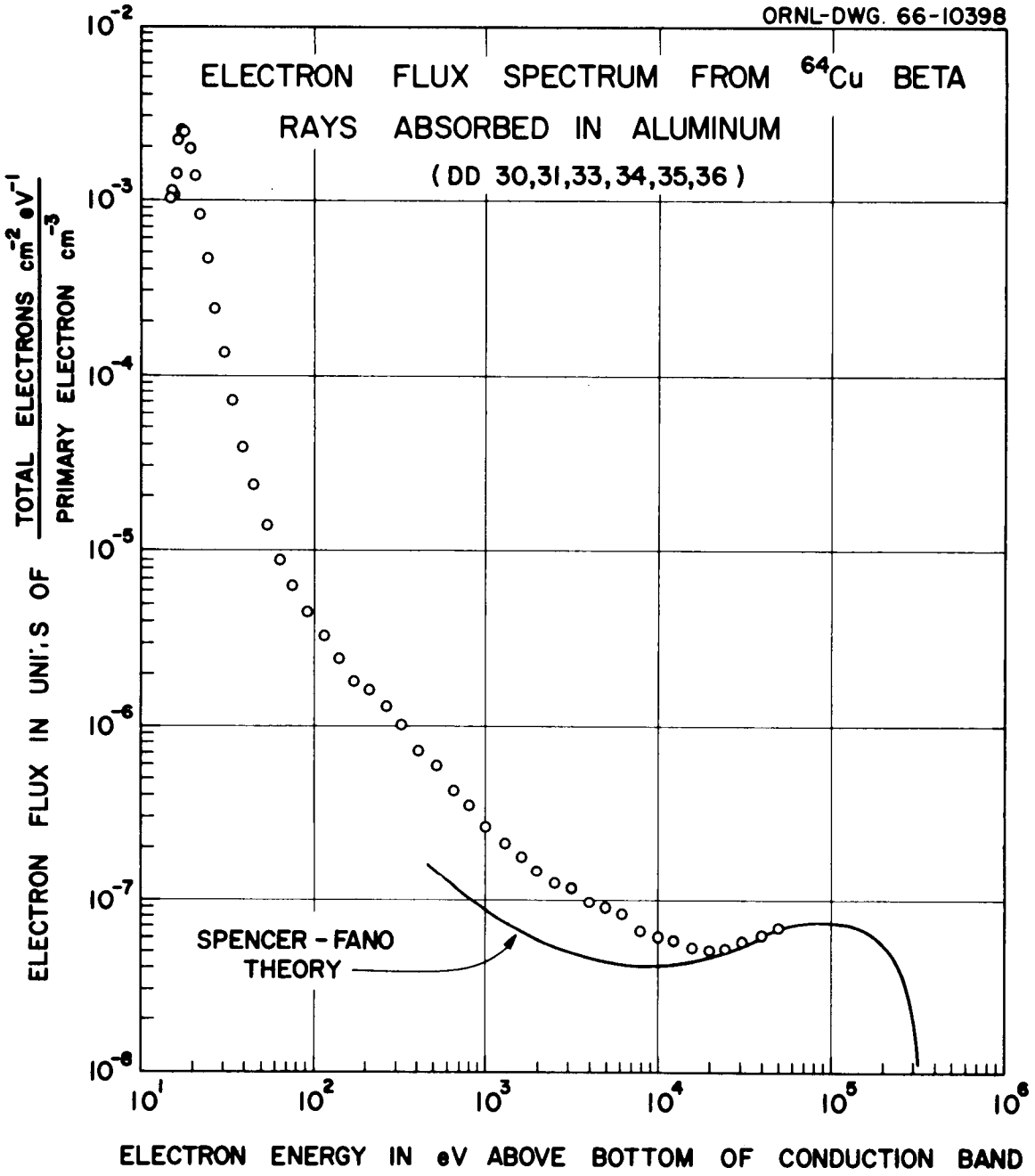

Figure 1. Electron flux spectrum from ^{64}Cu beta rays absorbed in aluminum.

The experimental data is from McConnell et al. [Rad. Res. 33, 216 (1968)] and the theory is that of Spencer and Fano [Phys. Rev. 93, 1172 (1964)].

free path for an electron to undergo a specific type of interaction is equivalent to specifying the interaction probability. The term attenuation length is often used to describe the equivalent mean free path for an electron which may interact by more than one mechanism.

This study is concerned with the interaction of low energy electrons (5-20 eV) in two free-electron-like metals. Free-electron-like metals were chosen because of their relatively simple electronic structure and because for them a great deal of theoretical work exists with which to compare the experimental results.

The most straightforward method of studying the interaction of low energy electrons with solids would be to bombard a thin free standing lamina of the solid with a beam of monoenergetic electrons and observe the emerging electrons. Kanter (1970) has been able to measure the electron attenuation length in gold and silver in the 5-11 eV range but was able to measure the attenuation length in aluminum only near 5 eV. One reason for the difficulty in these experiments is, as is shown in the next chapter, that the attenuation length for low energy electrons is predicted to be as short as 3 Å. The manufacture of free standing foils thin enough to transmit a usable fraction of the initial beam in this energy region is not possible so less straightforward methods have to be employed.

Methods that have been used to obtain low energy electron attenuation lengths include 1) a variety of schemes based upon the use of various metal-insulator or metal semi-conductor sandwiches and

2) photoemission. The methods based upon the various sandwiches have been reviewed by Garber et al. (1969). When electrons are injected into the metal from an insulator or semi-conductor, the sandwich methods are limited to electron energies less than 10 eV due to dielectric breakdown.

Another method based upon metal-insulator-metal sandwiches was employed by Garber et al. (1969). They bombarded the top metal foil of the sandwich with electrons and observed the current to both the top and bottom foils. The top foil was ~ 100 Å in thickness and thus single collision conditions were not met. Monte Carlo calculations using theoretical mean free paths gave good agreement with experiment only above 50 eV.

In photoemission, electrons are excited in the photocathode with energies ranging up to that of the photon energy and with a distribution in energy dependent upon the density of electronic states of the photocathode. The photoexcited electrons interact with the other electrons and ion cores of the photocathode, and a fraction of them escape over the surface barrier into the vacuum. Thus the emitted electrons carry information concerning the density of states of the photocathode and their interactions within the photocathode, and it is possible to extract information such as electron attenuation lengths from photoemission data.

Previous attempts to extract electron attenuation lengths from photoemission data have been based upon 1) the dependence of the quantum yield on the thickness of the photoemitter (Thomas, 1957; Sze et al., 1964; Baer et al., 1970; Pong et al., 1970); 2) the dependence of normalized

photoelectron energy distributions upon the thickness of a photoemitter evaporated upon a dissimilar substrate (Baer et al., 1970; Eastman, 1970); 3) the fitting of electron energy distribution curves to a Monte Carlo model for scattering (Stuart and Wooten, 1967); or 4) the fitting of the attenuation length to the absolute yield (Krolikowski and Spicer, 1969; 1970). Here we use a new approach in which the electron attenuation length is extracted from the angular dependence of the quantum yield as well as an approach based on the absolute yield.

During the course of the study several interesting and related topics were investigated. These topics include roughness aided photon-surface plasmon coupling, contamination effects, and exo-electron emission from magnesium. The former topics are treated within the main body of this study and the exo-electron emission from magnesium is presented in an appendix.

CHAPTER II

THEORETICAL CONSIDERATIONS

I. INTRODUCTION

In this chapter the theoretical concepts and relations used in the analysis and explanation of the experimental results are presented. The next section develops a three step model for volume photoemission that combines the recent optical excitation formalism of Pepper (1970) with the transport and escape model of Berglund and Spicer (1964a) to give what we feel is a complete model for volume photoemission of unscattered electrons. It is shown that this formalism can be extended to include emission of once-scattered electrons. Limiting cases of the new result show that it is compatible with previous results.

In Section III, two ways of obtaining experimental attenuation lengths of electrons by use of this model together with photoemission data are developed.

Section IV discusses the theories for the electron attenuation length in metals. Included in this section is a discussion of non-radiative surface plasmon creation by slow electrons.

Section V discusses the recent theories of Elson and Ritchie (1970; 1971) which describe surface roughness — aided excitation of non-radiative

surface plasmons by photons and rough surface scattering of photons. Non-radiative surface plasmon-one electron transitions are also discussed in this section.

Section VI discusses the optical plasma resonance and a method for obtaining the bulk plasma energy of a metal from photoemission data.

Section VII is a brief discussion of very recent theoretical work in photoemission.

II. A MODEL FOR VOLUME PHOTOEMISSION

In this section a model for volume photoemission from an arbitrary photoemitter is developed. The model gives the external energy distributions and the photoelectric yield in terms of the parameters of the substrate, the photoemitter and the exciting radiation. These parameters include the optical constants of the substrate, the optical constants, densities of states and thickness of the photoemitter, the wavelength, polarization and angle of incidence of the exciting radiation and an energy dependent electron attenuation length.

To begin the discussion, we will assume that we know the shape of the internal energy distribution of the photoexcited electrons, $N'(E)$, (assumed normalized) and seek to relate this to the external energy distribution of photoemitted electrons. The internal energy distribution of photoexcited electrons is discussed later in this section.

The number of electron-hole pairs created at a depth between y and y + dy in a photoemissive material is assumed to be proportional to the number of photons absorbed at that depth. If electron-hole pair creation is the dominant optical absorption mechanism then the number of electron-hole pairs created at a depth y in the material is very nearly equal to the number of photons absorbed there. The first item that we wish to find an expression for is $\eta(y)$, the number of photons absorbed per unit area at a depth between y and y + dy in the material divided by the number of photons incident per unit area of the irradiated surface.

The quantity $\eta(y)$ has been calculated by Pepper (1970). Figure 2 shows the geometry under consideration. Both the photoemissive material and the substrate are assumed to be uniaxially anisotropic absorbing media. These media have their optical axes of symmetry directed along the y axis. Thus ϵ_x describes the response of the system to the component of the electric field in the x-z plane and ϵ_y describes the response of the system to the component of the electric field along the y direction. The quantities ϵ_x and ϵ_y are the anisotropic analogs of the ordinary complex dielectric constant, ϵ, used to describe isotropic media. The calculations are completely rigorous classically and include the effects of multiple reflections between the vacuum-photoemitter interface and the photoemitter-substrate interface.

For s (perpendicular) polarization the result takes the following form

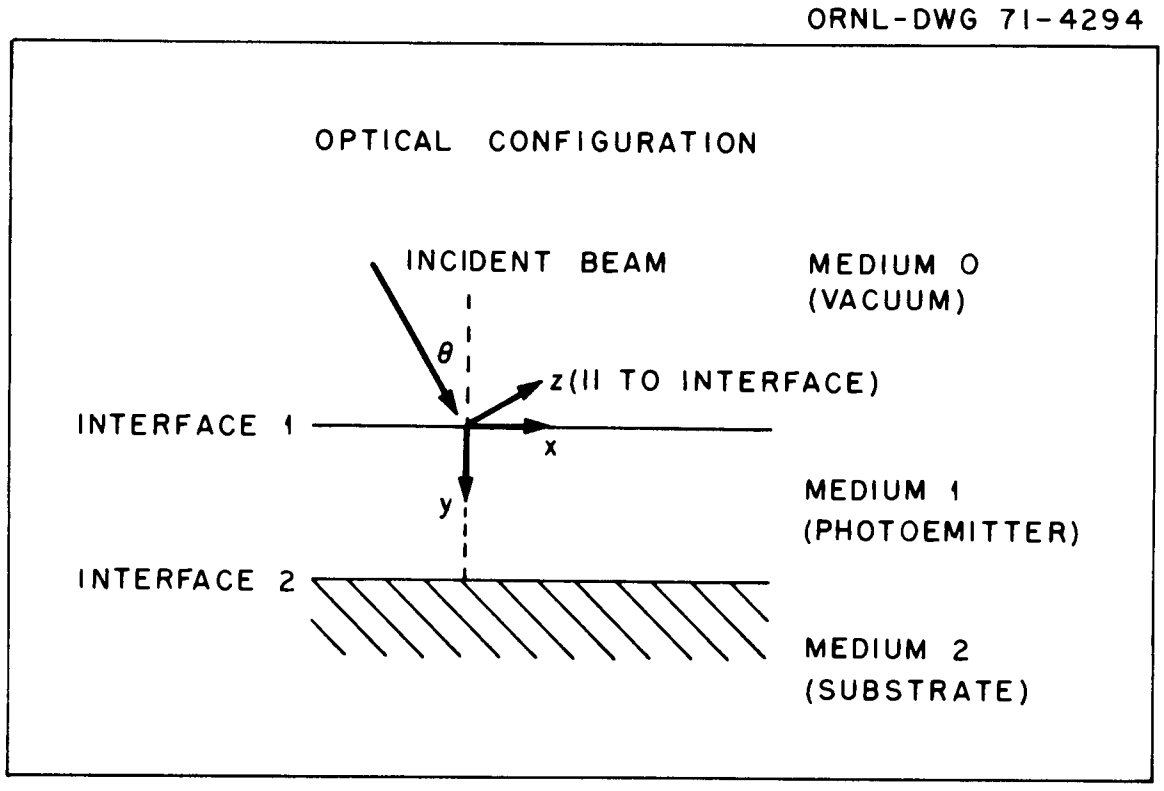

Figure 2. Diagram of the optical configuration.

$$\eta_s(y) = \frac{\left(1 - \left|r_{1,s}\right|^2\right)\alpha_s}{\left|1 + r_{1,s} r_{2,s} e^{2id\xi_{1,s}}\right|^2} \left\{ e^{-\alpha_s y} + \left|r_{2,s}\right|^2 e^{-\alpha_s(2d-y)} \right. \tag{1}$$

$$\left. + 2e^{-\alpha_s d} \operatorname{Re}\left[r_{2,s} e^{-2i\xi'_{1,s}(y-d)} \right] \right\}$$

where

$$r_{j,s} = \frac{\xi_{j-1,s} - \xi_{j,s}}{\xi_{j-1,s} + \xi_{j,s}} \qquad j = 1,\ 2 \tag{2}$$

and

$$\xi_{j,s} = \frac{2\pi}{\lambda_v} \left[\epsilon_{j,x} - \epsilon_o \sin^2\theta \right]^{\frac{1}{2}} \qquad j = 0,\ 1,\ 2 \tag{3}$$

and

$$\alpha_s = 2\xi''_{1,s} \tag{4}$$

The $\xi_{j,s}$ quantities are the y components of the complex propagation vectors for s polarized light in the three media where j = 0 corresponds to the vacuum, j = 1 corresponds to the photoemissive medium and j = 2 corresponds to the substrate. The $\epsilon_{j,x}$ terms are the complex dielectric functions for the three media corresponding to the response of the electric field in the x-z plane (parallel to the interface). The symbols λ_v and θ refer respectively to

the vacuum wavelength and angle of incidence of the radiation. The $r_{j,s}$ terms are the complex coefficients of reflectance and in this case, j = 1 refers to the vacuum-photoemitter interface and j = 2 refers to the photoemitter-substrate interface. A single prime (') applied to a quantity in the above formula denotes "real part of" and a double prime (") denotes "complex part of."

For the case of parallel (p) polarization, the equation for $\eta(y)$ takes the following form.

$$\eta_p(y) = \frac{\left(1 - |r_{1,p}|^2\right)\alpha_p}{\left|1 + r_{1,p} r_{2,p} e^{2id\xi_{1,p}}\right|^2} \left\{ e^{-\alpha_p y} \quad |r_{2,p}|^2 e^{-\alpha_p(2d-y)} \right. \tag{5}$$

$$\left. + 2e^{-\alpha_p d} \operatorname{Re}\left[r_{2,p} e^{-2i\xi'_{1,p}(y-d)}\right] \frac{\xi'_{1,p} \operatorname{Im}(\epsilon^*_{1,x}\xi_{1,p})}{\xi''_{1,p} \operatorname{Re}(\epsilon^*_{1,x}\xi_{1,p})} \right\}$$

where

$$r_{j,p} = \frac{\epsilon_{j,x}\xi_{j-1,p} - \epsilon_{j-1,x}\xi_{j,p}}{\epsilon_{j,x}\xi_{j-1,p} + \epsilon_{j-1,x}\xi_{j,p}} = t_{j,p} - 1 \qquad j = 1, 2 \tag{6}$$

and

$$\xi_{j,p} = \frac{2\pi}{\lambda_v} \left(\frac{\epsilon_{j,x}}{\epsilon_{j,y}}\right)^{\frac{1}{2}} \left[\epsilon_{j,y} - \epsilon_0 \sin^2(\theta)\right]^{\frac{1}{2}} \qquad j = 0, 1, 2 \tag{7}$$

and

$$\alpha_p = 2\xi''_{1,p} \tag{8}$$

In this equation the asterisk (*) denotes "complex conjugate of". The notation is somewhat misleading in that p and s are not true subscripts; it was felt, however, that it would be less confusing to simply retain the notation of the original author (Pepper, 1970). If unpolarized or partially polarized light is used, the excitation is described by a linear combination of the s and p components.

$$\eta(y) = a_s \eta_s(y) + a_p \eta_p(y) \tag{9}$$

where a_s and a_p are, respectively, the fraction of the radiation beam that is s or p polarized and $a_s + a_p = 1$.

We now know the number of electrons produced at a depth between y and y + dy per incident electron and have assumed that we know the shape of the energy distribution of these excited electrons. We now proceed to relate this internal density of photoexcited electrons to an external density of photoemitted electrons. The model of Berglund and Spicer (1964a) does this in a straightforward fashion.

Referring to Figure 3 the probability that an electron is excited at a depth between y and y + dy in the photoemitter by an incident photon is given by $\eta(y)dy$. The probability that an electron excited at a depth y and traveling at an angle θ to the normal reaches the surface unscattered, P_1, is

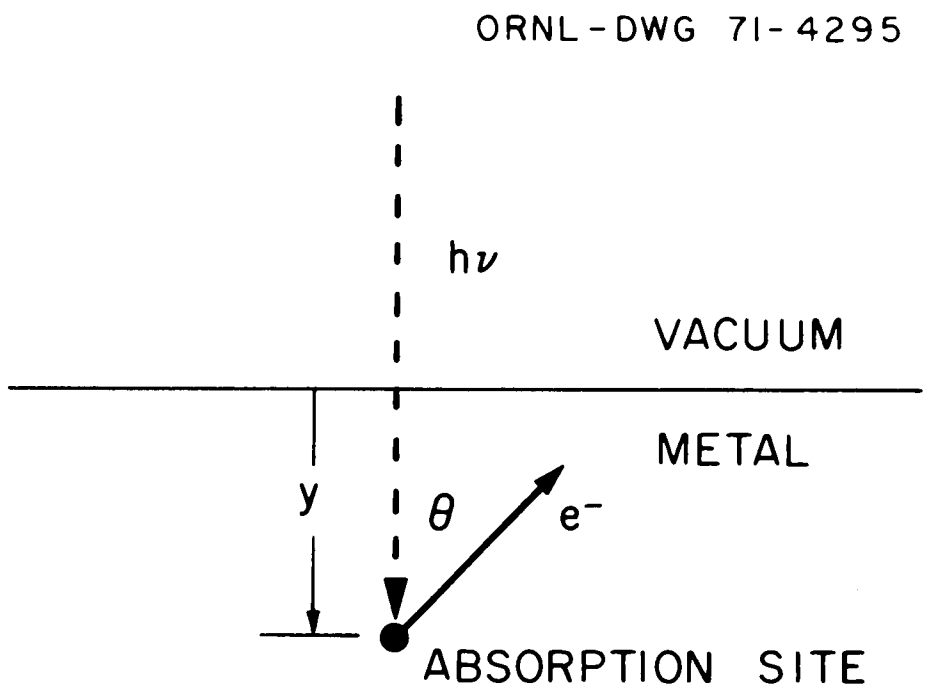

Figure 3. Diagram for the photoelectric model.

The photon is adsorbed at a depth y in the metal and an electron is excited which travels at an angle θ to the normal.

$$P_1 = \begin{cases} e^{-\frac{y}{\cos\theta} \cdot \frac{1}{\ell}} & \theta \le \frac{\pi}{2} \\ 0 & \theta > \frac{\pi}{2} \end{cases} \tag{10}$$

where ℓ is the attenuation length and is assumed to be a function only of the electron energy, E. The probability that an electron which reaches the surface escapes, P_2 is taken as

$$P_2 = \begin{cases} 1 & \theta \le \theta_c \\ 0 & \theta > \theta_c \end{cases} \tag{11}$$

where θ_c is a critical angle related to the electron momentum and is discussed later in this section. If we further assume that the electrons are excited isotropically, then the probability that an electron is directed into the annular ring between θ and $\theta + d\theta$, P_3 is

$$P_3 = \frac{1}{2} \sin\theta \, d\theta \quad . \tag{12}$$

Thus the total probability that an incoming photon will generate a photoelectron at a depth between y and y + dy which reaches the surface of the metal unscattered traveling at an angle between θ and $\theta + d\theta$ is the product of Equations 9, 10, 11, and 12.

$$\begin{aligned} P &= \eta(y) \, P_1 P_2 P_3 \, dy \, d\theta \\ &= \frac{1}{2}\eta(y) \, e^{-\frac{y}{\cos\theta} \frac{1}{\ell}} \sin\theta \, d\theta \, dy \quad . \end{aligned} \tag{13}$$

If we let $N'(E)$ represent the normalized internal distribution of photo-excited electrons, then the external distribution, $N(E)$ for a film of thickness d is given by

$$N(E) = \frac{1}{2} \int_0^{\theta_c} \int_0^{d} \eta(y)\, e^{-\frac{y}{\cos\theta}\frac{1}{\ell}} \sin\theta\, N'(E)\, dy\, d\theta \quad . \tag{14}$$

In this expression, θ_c and ℓ are functions of the electron energy and $\eta(y)$ is dependent on many variables.

The equation cannot be integrated in closed form as it stands but if the condition

$$e^{-\left(\frac{\sec\theta}{\ell} - \alpha\right)d} \ll 1 \tag{15}$$

is met for both $\alpha = \alpha_p$ and $\alpha = \alpha_s$ then the integration may be performed. This is not a trivial assumption, but the materials and experimental conditions used in this study were such that the condition was met. For a 1000 Å thick Al film illuminated by 584 Å radiation, α is .03 $(\text{Å})^{-1}$ at 90° angle of incidence (α is a maximum at 90°) and $\frac{\sec\theta}{\ell}$ 0.1 $(\text{Å})^{-1}$ so the argument of the exponent is $\sim$-60 for this case. The integration was performed by first integrating exactly over y from 0 to d, then setting the quantity $e^{-\left(\frac{\sec\theta}{\ell} - \alpha\right)d}$ equal to zero followed by an exact integration over θ from 0 to θ_c. The result of this calculation is given in the following two expressions. Note that while θ has been used to describe the angle of

incidence of the radiation as well as the angle made by the excited electron with respect to the normal, no ambiguity exists in the final result because only θ_c remains after integration.

$$N_s(E) = \frac{(1 - |r_{1s}|^2)\alpha_s}{2\left|1 + r_{1s}r_{2s}e^{2id\xi_{1s}}\right|^2} \left\{\left[\frac{1}{\alpha_s}(1 - \cos\theta_c) + \frac{1}{\ell\alpha_s^2}\ln\left|\frac{\frac{1}{\ell} + \alpha\cos\theta_c}{\frac{1}{\ell} + \alpha}\right|\right]\right.$$

$$+ |r_{2s}|^2 e^{-2\alpha_s d}\left[-\frac{1}{\alpha_s}\left(1 - \cos\theta_c\right) + \frac{1}{\ell\alpha_s^2}\ln\left|\frac{\frac{1}{\ell} - \alpha\cos\theta_c}{\frac{1}{\ell} - \alpha_s}\right|\right] \quad (16a)$$

$$\left. + 2e^{-\alpha_s d}\,\mathrm{Re}\left[r_{2s}\,e^{+2i\xi'_{1s}}\left(\frac{1 - \cos\theta_c}{2i\xi'_1} - \frac{1}{4\ell\,\xi'^2_{1s}}\ln\left(\frac{\frac{1}{\ell} + 2i\xi'_{1s}\cos\theta_c}{\frac{1}{\ell} + 2i\xi_{1s}}\right)\right)\right]\right\}$$

$$\times N'(E)$$

$$N_P(E) = \frac{\left(1 - |r_{1p}|^2\right)\alpha_p}{2\left|1 + r_{1p}r_{2p}e^{2id\,\xi_{1p}}\right|^2} \left\{\left[\frac{1}{\alpha_p}\left(1 - \cos\theta_c\right) + \frac{1}{\ell\alpha_p^2}\ln\left(\frac{\frac{1}{\ell} + \alpha\cos\theta_c}{\frac{1}{\ell} + \alpha}\right)\right]\right.$$

$$+ |r_{2p}|^2 e^{-2\alpha_p d}\left[-\frac{1}{\alpha_p}\left(1 - \cos\theta_c\right) + \frac{1}{\ell\alpha_p^2}\ln\left(\frac{\frac{1}{\ell} - \alpha_p\cos\theta_c}{\frac{1}{\ell} - \alpha_p}\right)\right] \quad (16b)$$

$$+ 2\, e^{-\alpha_p d}\, \mathrm{Re}\Big[r_{2p}\, e^{+ 2i\xi'_{1p} d} \Big(\frac{(1 - \cos\theta_c)}{2i\xi'_{1p}} - \frac{1}{4\ell\xi'^{2}_{1}} \ln\Big(\frac{\frac{1}{\ell} + 2i\xi'_{1p}\cos\theta_c}{\frac{1}{\ell} + 2i\xi'_{1p}} \Big)\Big)$$

$$\times \Big[\frac{\xi'_{1p}\, \mathrm{Im}\big(\epsilon^{*}_{1x}\, \xi_{1p}\big)}{\xi''_{1p}\, \mathrm{Re}\big(\epsilon^{*}_{1x}\, \xi_{1p}\big)} \Big]\Big\}\, N'(E)$$

For the case of unpolarized or partially polarized light the result is

$$N(E) = a_s N_s(E) + a_p N_p(E) \tag{17}$$

where a_s and a_p have the meanings assigned to them in Equation 9.

The total yield is simply the integral over the energy distribution.

$$Y(h\nu) = \int_0^\infty N(E, h\nu)\, dE \tag{18}$$

Equations 16a and 16b are quite cumbersome because of the inclusion of the effects of multiple interference and optical anisotropy. It is readily shown, however, that they correspond to earlier results when appropriate limits are taken.

For the case of an isotropic photoemitter and substrate, $\epsilon_{jx} = \epsilon_{jy} = \epsilon_j$ and the distinction between polarizations vanishes for ξ and α. If we further specialize to normal incidence, then the reflectance

coefficients, r_{js} and r_{jp} (Equations 2 and 6) become identical, If we then consider the case for which $d \gg \frac{1}{\alpha}$(semi-infinite photoemitter) then the term $e^{2i\xi_1 d}$ in the denominator of the first factor in Equations 16a and 16b vanishes because the imaginary part of ξ_1 is just $\alpha/2$. Furthermore, the factors $e^{-2\alpha d}$ and $e^{-\alpha d}$ multiplying the last two terms in Equations 16 and 17 vanish, and thus these terms also vanish. If we let the reflectivity $R = |r_{1p}|^2 = |r_{1s}|^2$, then both Equations 16a and 16b take the form

$$N(E) = \frac{(1-R)\alpha}{2}\left\{\frac{1}{\alpha}\left(1 - \cos\theta_c\right) + \frac{1}{\ell\alpha^2}\ln\left(\frac{\frac{1}{\ell} + \alpha\cos\theta_c}{\frac{1}{\ell} + \alpha}\right)\right\} \tag{19}$$

$$\times N'(E)$$

which is equivalent to the result of Berglund and Spicer (1964a) for photoemission of unscattered electrons from a semi-infinite photoemitter excited by normally incident radiation.

For the case where $\cos\theta_c \approx 1$, corresponding to near normal emission of the electrons Equations 16a and 16b should reduce to the result of Pepper (1970) multiplied by an escape probability. This result is expected because Pepper considered only electrons traveling normally to the surface and did not include the escape probability. The limit may be conveniently taken by expanding the logarithmic terms and combining the first term in each logarithmic expansion with the term preceding the logarithm. As an

example consider the first logarithmic term and its preceding term in Equation 16a,

$$\frac{1}{\alpha_s}\left(1 - \cos\theta_c\right) + \frac{1}{\ell\alpha_s^2}\ln\left(\frac{\frac{1}{\ell} + \alpha_s\cos\theta_c}{\frac{1}{\ell} + \alpha_s}\right)$$

Expanding the logarithm,

$$\ln\left(\frac{\frac{1}{\ell} + \alpha_s\cos\theta_c}{\frac{1}{\ell} + \alpha_s}\right) = \ln\left(1 - \frac{\alpha_s(1 - \cos\theta_c)}{\frac{1}{\ell} + \alpha_s}\right)$$

$$= (1 - \cos\theta_c)\frac{\alpha_s}{\frac{1}{\ell} + \alpha_s} - \frac{(1 - \cos\theta_c)^2}{2}\left(\frac{\alpha_s}{\frac{1}{\ell} + \alpha_s}\right)^2$$

$$- \frac{(1 - \cos\theta_c)^3}{3}\left(\frac{\alpha_s}{\frac{1}{\ell} + \alpha_s}\right)^3 + \text{---} \; . \tag{20}$$

We are interested in the result when $\cos\theta \approx 1$, so we may drop all terms in the expansion except the first. Combining the first term of the expansion with $\frac{1}{\alpha_s}(1 - \cos\theta_c)$ we obtain

$$\frac{1}{\alpha_s}(1 - \cos\theta_c) + \frac{1}{\ell\alpha_s^2}\ln\left(\frac{\frac{1}{\ell} + \alpha_s\cos\theta_c}{\frac{1}{\ell} + \alpha_s}\right) \approx (1 - \cos\theta_c)\left(\frac{1}{\frac{1}{\ell} + \alpha_s}\right) \tag{21}$$

When this procedure is applied to the remaining terms in Equation 16, the following is obtained.

$$N_s(E) \approx \frac{1}{2}(1 - \cos\theta_c) \frac{(1 - |r_{1s}|^2)\alpha_s}{|1 + r_{1s} r_{2s} e^{2id\xi_{1s}}|^2}$$

$$\times \left\{ \frac{1}{\frac{1}{\ell} + \alpha_s} + \frac{|r_{2s}|^2 e^{-2\alpha_s d}}{(\frac{1}{\ell} - \alpha_s)} + 2e^{-\alpha_s d} \right. \tag{22}$$

$$\left. \times \mathrm{Re}\left[\frac{r_{2s} e^{2i\xi'_{1s}}}{2i\xi'_{1s} + \frac{1}{\ell}} \right] \right\} N'(E)$$

A similar equation results if this procedure is applied to the p polarization case. Apart from the factor $\frac{1}{2}(1 - \cos\theta_c)$ these results are identical with those of Pepper (1970) if the approximation made in Equation 15 is made to Pepper's results. The factor $\frac{1}{2}(1 - \cos\theta_c)$ does not appear in Pepper's equation because he did not include the escape probability in his model.

The discussion up to this point has been limited to the excitation, transport and escape phenomena of unscattered electrons. Berglund and Spicer (1964) also treat the transport and escape of once-scattered electrons for the case of light incident normally upon a semi-infinite isotropic photoemitter. This treatment could, at least in principle, be extended to

the more general case of arbitrary polarization and angle of incidence of the exciting radiation and to anisotropic films of arbitrary thickness. The general extension would be quite difficult to perform but for the case of a semi-infinite photoemitter, the extension to arbitrary angle of incidence and polarization of the exciting radiation and to optically anisotropic films is reasonable.

For the s polarization case the contribution to the observed external energy distribution made by once-scattered electrons is given by

$$\left(N_s(E)\right)_{scat} = \frac{1}{4}\left(1 - |r_{1s}|^2\right) \int N'(E') \left\{\left(1 - \cos\theta_c\right)\right.$$

$$+ \frac{1}{\alpha_s \ell} \ln\left(\frac{1 + \alpha_s \ell \cos\theta_c}{1 + \alpha_s \ell}\right)\Bigg\} \left\{\frac{1}{\alpha_s \ell'} \ln(1 + \alpha_s \ell')\right.$$

$$\left. + \frac{\ell}{\ell'} \ln\left(1 + \frac{\ell'}{\ell}\right)\right\} P(E, E')\, dE' \quad . \tag{23}$$

In this expression the unprimed variables (ℓ, E) refer to the scattered electrons and the primed variables (ℓ', E') refer to the unscattered or primary electrons. The result for p polarization is given by replacing s by p wherever it occurs. The quantity $P(E, E')$ is the probability that an electron of energy E' will scatter to an energy E. This expression is not complete because it neglects primary electrons which strike the surface at an angle greater than the critical angle, θ_c, and are reflected back into the metal.

These reflected electrons have been treated by Krowlikowski (1967). Extending his result to non-normally incident light of arbitrary polarization we find (in our notation) that

$$(N_s(E))_{ref} = \frac{1}{8}(1 - |r_{1s}|^2) \left\{\cos\theta_c' - \frac{1}{\alpha_s \ell'} \ln(1 + \alpha_s \ell' \cos\theta_c')\right\} \tag{24}$$

$$\times N'(E) \left\{P(E, E')(1 - \cos\theta_c) \frac{\ell}{\ell'} \ln\left(1 + \frac{\ell'}{\ell}\right)\right\}$$

In this expression, θ_c is the critical angle for scattered electrons and θ_c' is the critical angle for the primary electrons and all other quentities have their previous meanings. The term contained within the first set of curly brackets {} is proportional to the number of electrons returned to the metal after striking the surface while the term in the second set of curly brackets governs the subsequent scattering, transport and escape of the returned electrons. The complete energy distributions of scattered electrons is given by the sum of Equations 23 and 24. The details of the above derivations are not given because no explicit use was made of them. The derivations were done so we would be able to give a complete extension of the Berglund and Spicer model to arbitrary angles of incidence and polarization and to anisotropic films.

We must next establish expressions for the critical angle, θ_c, and for the internal distribution of photoexcited electrons, N(E). It is convenient

to do this in terms of a model for a metal. We shall choose the free electron model because the metals used in this experiment were free-electron-like. Figure 4 depicts a simple photoexcitation model. The lower curve exhibits the $E^{\frac{1}{2}}$ density of unexcited states characteristic of the free electron gas. Also indicated is the Fermi level, E_F, and the vacuum level E_v. The work function, Φ, is just $E_v - E_F$. We shall refer to the region between 0 and E_F as the occupied part of the conduction band of the metal and to the region $E > E_F$ as the empty conduction band.

The concept of a critical angle comes from the work of Fowler (1931). An electron is assumed to be able to escape over the work function, Φ, if the component of the electron's momentum normal to the surface ($p \cos \theta$) exceeds a critical value, p_c, where

$$p_c = \sqrt{2mE_v} \tag{25}$$

and

$$p = \sqrt{2mE}$$

It should be stressed that E and E_v must be measured from the bottom of the conduction band as shown in Figure 4. The component of the electron's momentum normal to the surface is just $p \cos \theta$ where θ is the angle between the normal and the direction of the electron. Thus for an electron to escape, we require that

$$p \cos \theta \geq \sqrt{2mE_v}$$

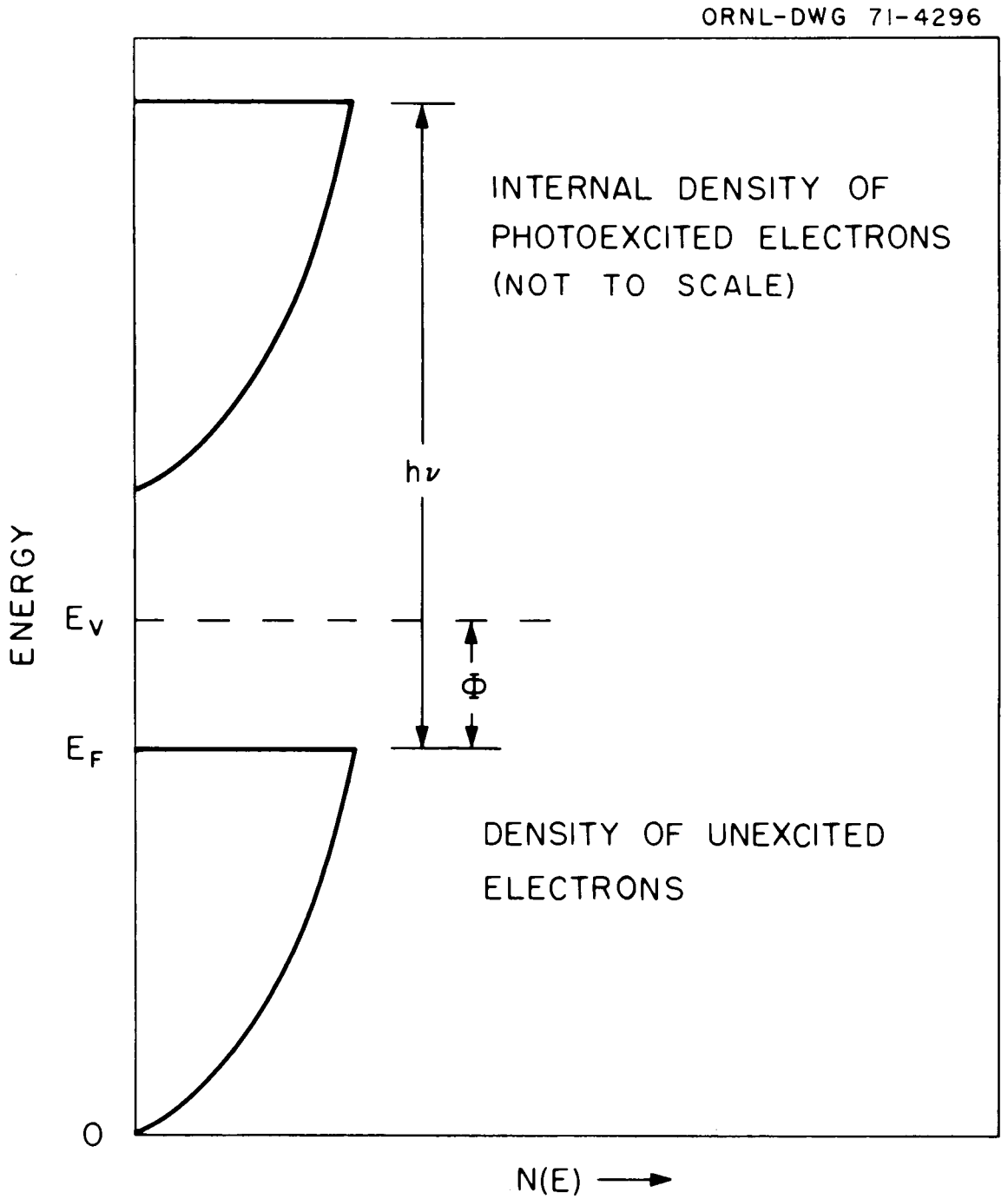

Figure 4. Diagram for the simple photoelectric excitation model

or

$$\sqrt{2mE}\cos\theta \geq \sqrt{2mE_v} \quad .$$

Thus the maximum angle that an electron can possess and still have the potential to escape, θ_c, is given by

$$\cos\theta_c = \sqrt{\frac{E_v}{E}} \quad . \tag{26}$$

The cone defined by $0 \leq \theta \leq \theta_c$ is called the escape cone.

If $\xi(\theta, \varphi)$ is the normalized directional distribution of excited electrons within the photoemitter, then the fraction of the electrons whose directions lie within the escape cone, T, is given by

$$T = \frac{1}{4\pi}\int_0^{2\pi} d\phi \int_0^{\theta_c} \xi(\theta, \varphi)\sin\theta\, d\theta \quad .$$

For the isotropic case ($\xi(\theta, \varphi) = 1$) this reduces to

$$T = \frac{1}{2}(1 - \cos\theta_c) \tag{27}$$

This function has been called the threshold function (Berglund and Spicer, 1964a). It should be noted that the possibility of quantum mechanical reflection at the surface has been neglected.

We come finally to the problem of expressing N'(E), the internal density of photoexcited electrons. Two excitation models are currently in use, the direct transition model in which the crystal momentum of Bloch

states is conserved and the indirect transition model in which the crystal momentum is not directly conserved. For materials which exhibit pronounced structure in the external photoelectron energy distributions it may be possible to distinguish between these two models (Berglund and Spicer, 1964). Lack of strong structure in the data obtained on the simple metals of this study did not permit the choice of one model over the other. We, therefore, include a description of both models. Eastman (1971) has recently given a concise description of both the direct and the indirect transition models, and we follow him.

Direct optical transitions are assumed to take place between well-defined Bloch one-electron states. Energy and crystal momentum are conserved. The quantity $E_n(\vec{k})$ is the electron energy where n is the band index and $\vec{k}$ is the crystal momentum. The imaginary part of the dielectric constant, $\epsilon_2(\omega)$ is given by

$$\epsilon_2(\omega) = \frac{e^2}{\pi m^2 \omega^2} \sum_{n,n'} \int d^3k \left[|\hat{A} \cdot \vec{P}_{n,n'}(\vec{k})|^2 \, \delta(E_{n'}(\vec{k}) - E_n(\vec{k}) - \hbar\omega) \right] . \qquad (28)$$

In this expression $|\hat{A} \cdot \vec{P}_{nn'}(\vec{k})|^2$ is the momentum matrix element connecting the initial and final states. The Dirac function assures conservation of energy. Momentum conservation is ensured by requiring $\vec{k}$ to be unchanged for the initial and final states.

The density of excited electrons, N'(E) can be evaluated from Equation 28 by placing another δ function, $\delta[E_n'(\vec{k}) - E]$ in the integrand to

pick out all transitions to energy E and then normalizing the result.

$$N'(E) = \frac{e^2}{\pi m^2 \omega^2 \epsilon_2(\omega)} \sum_{n,n'} \int d^3k \; |\hat{A} \cdot \vec{P}_{nn'}(\vec{k})|^2 \tag{29}$$

$$\delta\left[E_{n'}(\vec{k}) - E_n(\vec{k}) - \hbar\omega\right] \delta\left[E_{n'}(\vec{k}) - E\right]$$

This can be expressed in terms of a line integral which may be more convenient for evaluation.

$$N'(E) = \frac{e^2}{\pi m^2 \omega^2 \epsilon_2(\omega)} \sum_{n,n'} \int_{\substack{E_{n'}=E \\ E_n = E - \hbar\omega}} d\ell \frac{|\hat{A} \cdot \vec{P}_{nn'}(\vec{k})|^2}{|\nabla_k E_n \times \nabla_k E_{n'}|} \tag{30}$$

In lieu of a rigorous derivation of Equation 30 we merely point out that each δ function describes a surface in $\vec{k}$ space and that Equation 30 is simply the line integral around the intersection of the two surfaces. The denominator arises as a consequence of the transformation of the integral.

From Equation 30 we see that the energy distribution of the excited electrons, N'(E) is a complicated function of the one-electron energies. It is worth pointing out, however, that structure in either the empty conduction bands or occupied part of the conduction band causes structure in N'(E) through structure in $\nabla_k E_n$ or $\nabla_k E_{n'}$.

We now describe the non-direct transition model first considered by Berglund and Spicer (1964a). In this model it is assumed that either crystal momentum is not an important selection rule or that the momentum is taken up in some unspecified process (for example, phonons) which contribute momentum but negligible energy to the excitation process. Thus the matrix element $|\hat{A}\cdot\vec{P}_{nn'}(\vec{k})|^2$ is independent of $\vec{k}$ and we can write

$$|\hat{A}\cdot\vec{P}_{nn'}(\vec{k})|^2 = |P(E)|^2 \tag{31}$$

Since $\vec{k}$ is no longer conserved we can sum over energy and the imaginary part of the dielectric constant becomes

$$\epsilon_2 = \frac{e^2}{\pi m^2\omega^2}\int_0^{\hbar\omega} dE'\ \rho_v(E' - \hbar\omega)\,\rho_c(E')\ |P(E')|^2 \tag{32}$$

where ρ_v and ρ_c are the densities of states of the occupied part of the conduction band and the empty conduction band, respectively. Using the same procedure employed for direct transitions, we insert the δ function $\delta(E - E')$ to pick out all transitions to energy E and normalize. The result is

$$N'(E) = \frac{e^2}{\epsilon_2(\omega)\pi m\omega^2}\int_0^{\hbar\omega} dE'\rho_v(E' - \hbar\omega)\rho_c(E')|P(E')|^2\delta(E - E') \quad . \tag{33}$$

Integrating we find that

$$N'(E) = \frac{1}{\epsilon_2(\omega)} \frac{e^2}{\pi m^2 \omega^2} \rho_v(E - \hbar\omega)\, \rho_c(E)\, |P(E)|^2 \quad . \tag{34}$$

In practice, $|P(E)|^2$ is often grouped with ρ_v and the product termed the optical density of states. An important feature of this model is that any structure in ρ_v will move linearly with photon energy.

We now give an example of the internal and external energy distributions of photoexcited electrons using both the direct and indirect transition models. Eastman (1971) has given an example for the direct transition case and we use his example for direct transitions and then evaluate Equation 34 using Eastman's parameters to obtain the equivalent distributions in the non-direct case.

Consider a free-electron-like metal whose work function, Φ, is 4 eV and whose Fermi energy is 6 eV. Assume that for the energy region under consideration that there is only one important reciprocal lattice vector, $\vec{G}$ and that its magnitude is such that $\frac{\hbar^2 G^2}{2m}$ = 28 eV. The density of states and band structure for this simple model is shown in the reduced zone scheme in Figure 5. The equations for the two bands under consideration are

$$E_1(\vec{k}) = \frac{\hbar^2}{2m} k^2 \tag{35}$$

$$E_2(\vec{k}) = \frac{\hbar^2}{2m} (\vec{k} - \vec{G})^2 \tag{36}$$

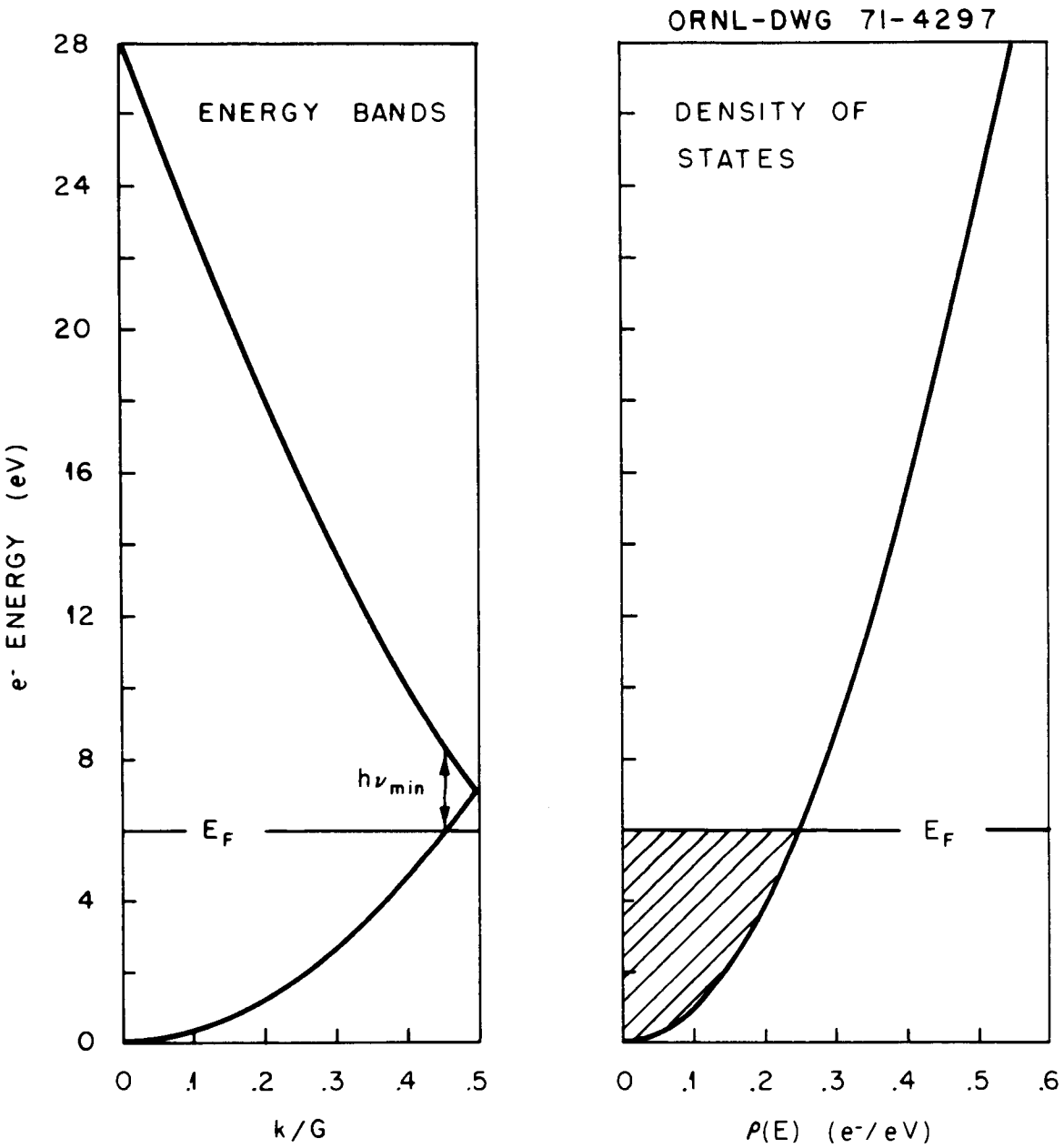

Figure 5. Band structure and density of states for a simple metal.

The metal is assumed to be free electron-like with a Fermi energy of 6 eV and an inverse lattice vector, $\vec{G}$, whose magnitude is given by $\hbar^2|\vec{G}|^2/2m = 28$ eV. [D. E. Eastman, in Techniques of Metals Research VI, ed. E. Passaglia (Interscience, New York, to be published, 1971)].

For a direct transition (vertical in the reduced zone scheme) we have

$$E_2(\vec{k}) - E_1(\vec{k}) = \hbar\omega \quad . \tag{37}$$

This gives

$$\vec{k} \cdot \vec{G} = \frac{1}{2}(G^2 - 2m\omega/\hbar \quad . \tag{38}$$

The right-hand side of Equation 38 is a constant for a particular metal and photon energy. Since $\vec{G}$ is a constant vector, the form $\vec{k} \cdot \vec{G}$ = constant gives a plane in $\vec{k}$ space perpendicular to $\vec{G}$ at a distance $\frac{1}{2G}(G^2 - 2m\omega/\hbar)$ from the origin. This plane defines the values of $\vec{k}$ which are allowed to participate in the direct transitions. The range of available $\vec{k}$'s is given by $0 \leq |\vec{k}| \leq k_F$ which defines the Fermi sphere. Thus the intersection of the plane defined by Equation 38 and the Fermi sphere gives the values of k which participate in the direct transitions. It is apparent from Equation 38 that there may be a minimum value of $\hbar\omega$ required for a direct transition to take place. Transitions begin when the plane defined by Equation 38 just touches the Fermi sphere. This minimum value is also apparent from Figure 5.

The internal distribution of photoexcited states is evaluated by first considering the range in energy of the excited electrons. From our previous discussion of allowed $\vec{k}$ states from which transitions could take place we found that the allowed $\vec{k}$'s came from the intersection of a plane given by Equation 38 with the Fermi sphere. Thus the allowed initial energies range from the Fermi energy down to $E(\vec{k}_{min})$ where $\vec{k}_{min}$ is the distance along

$\vec{G}$ that the plane lies.

$$\frac{\hbar^2 k_F^2}{2m} \geq E \geq \frac{\hbar^2}{2m} \left\{ \frac{1}{2G} \left(G^2 - 2m\omega/\hbar \right) \right\}$$

The shape of the energy distribution is obtained from Equation 30. Evaluating the denominator,

$$\left| \nabla_k E_1 \times \nabla_k E_2 \right| = \frac{\hbar^2}{m} G \, k \sin \theta$$

where θ is the polar angle with respect to the $\vec{G}$ axis. Examining Equation 29 we note that each δ function describes a sphere in $\vec{k}$ space. The integral in Equation 30 is taken about the line of intersection of the two spheres. Evaluating $d\ell$ we find that

$$d\ell = k \sin \theta \, d\varphi$$

where φ is the polar angle. Thus Equation 30 becomes

$$N'(E) \propto \int_0^{2\pi} d\varphi \, \frac{k \sin \theta}{k \sin \theta} = \text{constant} \tag{41}$$

Thus the remarkable result is that the direct transition model gives for this simple case a density of excited states which is constant between definite energy limits defined by Equation 39 and zero outside those limits.

The energy distribution obtained from the indirect transition scheme is easily evaluated from Equation 33. For this case the band structure is unimportant and the required densities of states shown in Figure 5, page 30, are

$$\rho_v \propto E^{\frac{1}{2}} \qquad 0 \le E \le E_F ,$$

$$\rho_v = 0 \qquad E > E_F \tag{42}$$

and

$$\rho_c \propto E^{\frac{1}{2}} \qquad E > E_F \tag{43}$$

Figure 6 gives the internal densities of excited states for each of the models for two energies.

Figure 7 gives the external density of photoemitted electrons for the two models. The direct transition case was evaluated by Eastman (1970) and the indirect transition case was obtained from Equation 19.

III. EXTRACTION OF THE ELECTRON ATTENUATION LENGTH

We now give two methods for extracting the electron attenuation length, ℓ, from photoemission data and the model we have developed.

The first method is based upon Equation 19 which describes photoemission from a semi-infinite isotopic sample excited by normal incidence radiation. The method is applicable only to metals for which $N'(E)$ is known or can be evaluated fairly reliably. In addition one must know (or measure)

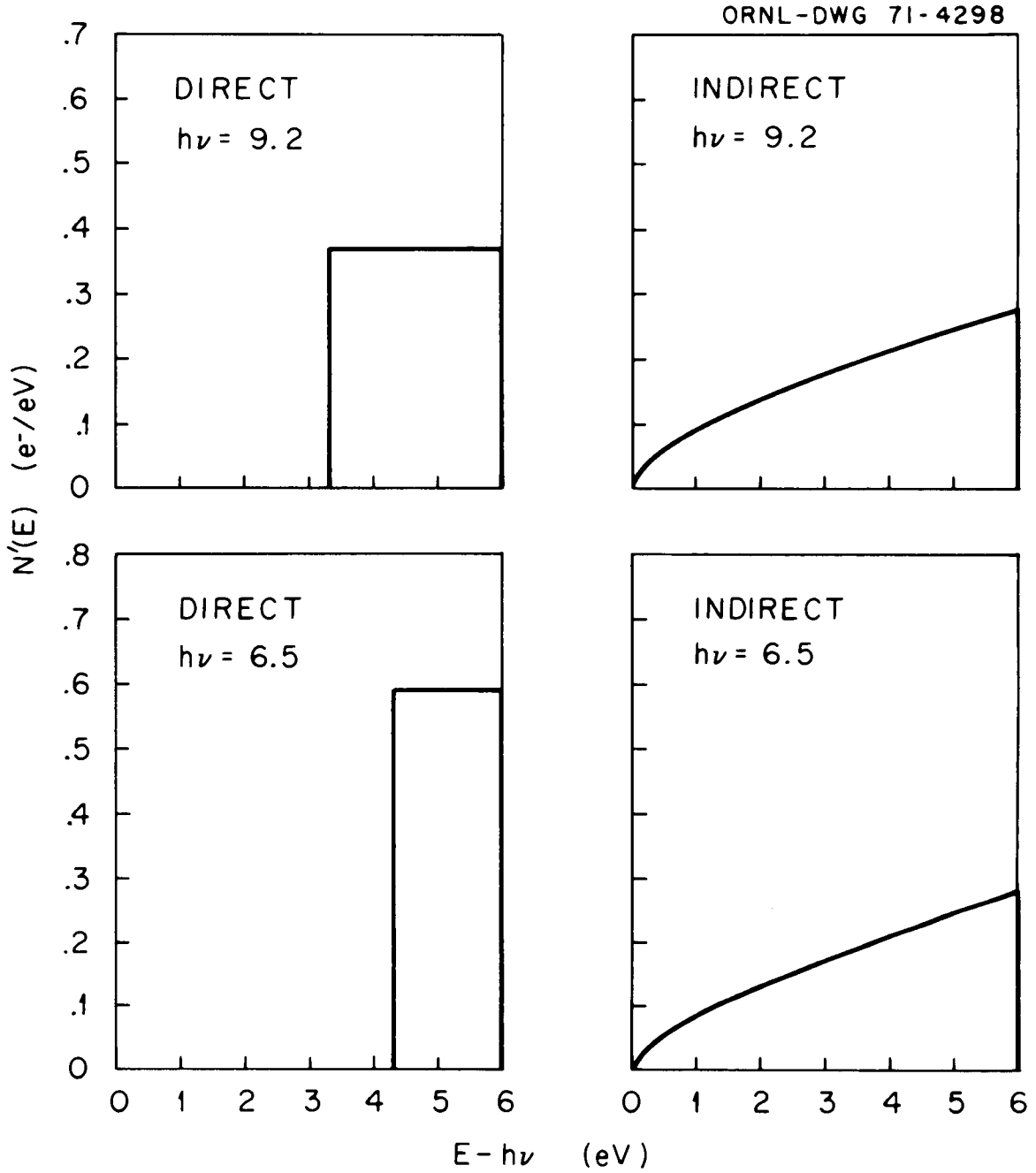

Figure 6. Theoretical internal densities of excited electrons for a simple metal.

The metal is assumed to be free electron-like with a Fermi energy of 6 eV and an inverse lattice vector, $\vec{G}$, whose magnitude is given by $\hbar^2|\vec{G}|^2/2m = 28$ eV. The internal densities of excited electrons are shown for both the direct and indirect transition cases and for the two photon energies.

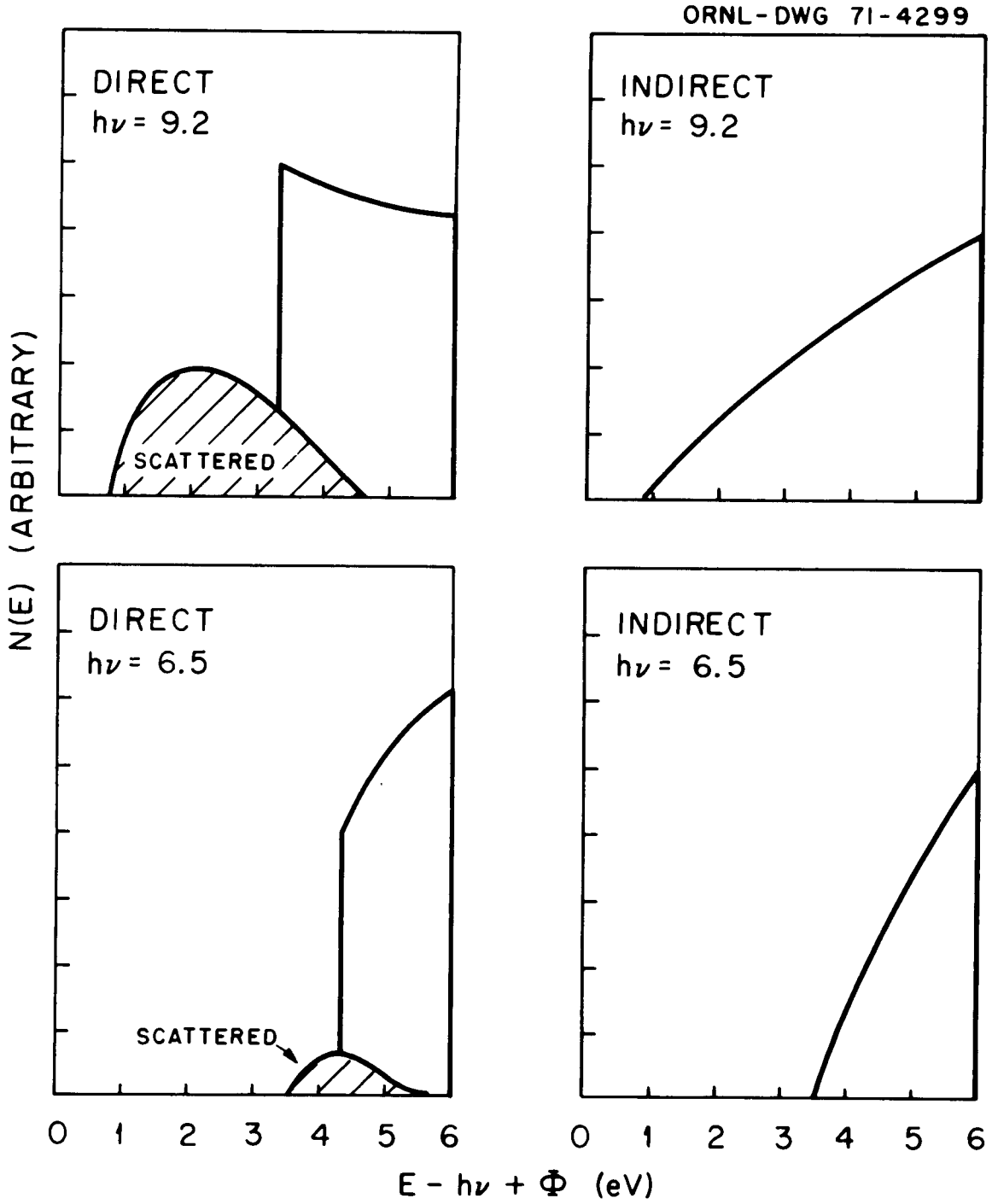

Figure 7. Theoretical external electron energy distributions for a simple metal.

The metal is assumed to be free electron like with a Fermi energy of 6 eV, a work function of 4 eV and an inverse lattice vector, $\vec{G}$, whose magnitude is given by $\hbar^2|\vec{G}|^2/2m = 28$ eV. The direct transition cases are from Eastman [D. E. Eastman, in Techniques of Metals Research VI, ed., E. Passaglia (Interscience, New York, to be published, 1971)].

the optical constants of the photoemitter and be able to estimate the energy dependence of the critical angle for electron escape, θ_c. To use the method both the absolute quantum yield and the electron energy distributions of the model must be measured.

An underlying assumption is that as electrons are scattered inelastically, they are removed from the high energy portion of the external density of photoemitted electrons. This is a reasonable assumption because as Ritchie and Ashley (1965) show, the average energy loss that an electron experiences undergoing an electron-electron collision is between $\frac{1}{2}$ and $\frac{2}{3}$ of the initial energy (measured from the Fermi level). Figure 7 shows the contribution of scattered electrons to the energy distributions in a free electron metal. It is apparent from this figure that the scattered electrons do not contribute significantly to the high energy portion of the distribution. Energy losses due to volume plasmon excitation are discrete with the electron losing an amount of energy equal to or greater than the bulk plasma energy of the metal. Thus the high energy end of a photoelectron energy distribution is composed almost entirely of primary or unscattered electrons.

The procedure used to extract the electron attenuation length is to compare the expected yield of high energy electrons with the experimental yield of high energy electrons using Equation 19, with the energy attenuation length as a parameter. In general this must be done numerically but for certain cases one can obtain approximate closed form inversion of Equation 19. An expansion of Equation 19 that is valid when the optical

attenuation length, $1/\alpha$ is greater than the electron attenuationlength, ℓ, is given by

$$N(E) = N'(E)\frac{(1-R)}{2}\left\{\frac{1}{2}\alpha\ell\,(1-\cos^2\theta_c) - \frac{1}{3}(\alpha\ell)^2(1-\cos^3\theta_c) + \frac{1}{4}(\alpha\ell)^3(1-\cos^4\theta_c) - \cdots\right\}. \tag{44}$$

For the limiting case of $\alpha\ell \ll 1$. This expression reduces to

$$N(E) = \frac{1}{4}N'(E)\,(1-R)\,\alpha\ell\sin^2\theta_c \tag{45}$$

and

$$\ell = \frac{N(E)}{N'(E)\,(1-R)\,\alpha\sin^2\theta_c} \quad . \tag{46}$$

This expression will differ from the exact expression by no more than 20% if $\alpha\ell \leq 0.1$.

A second method for obtaining electron attenuation lengths was suggested by Pepper (1970) and is based upon Equation 18. To use this method, one measures the yield of a vacuum evaporated photoemitter as a function of angle and fits the experimental data to Equation 18, using ℓ as a fitting parameter. All of the other parameters of the equation such as the optical properties of the photoemitter and its substrate, the thickness of the photoemitter and the wavelength, polarization, and angle of incidence of the radiation are independently measurable.

When applied to the total yield, the method necessarily gives an average attenuation length for all the electrons excited within the photoemitter. It is also necessary to pick an average value of the maximum escape angle, θ_c.

IV. THEORETICAL ELECTRON ATTENUATION LENGTHS

Excited electrons moving through a solid crystal can be scattered by phonons, lattice imperfections, impurities, other electrons and plasmons. The types of scattering events can be placed into two categories, elastic scattering involving momentum changes but negligable energy changes and inelastic scattering involving both momentum and energy changes. Lattice imperfection, phonon and impurity scattering is elastic; electron-electron and electron-plasmon scattering is inelastic. The relative importance of a particular type of scattering event is inversely proportional to the mean free path for that type of event. It is generally accepted for electron energies greater than a few eV, that inelastic scattering is more important than elastic scattering (Sze et al., 1964; Kane, 1967). In any case elastic scattering, because it involves negligible energy loss, influences the photoemission result only to the extent of lengthening the path that an electron must traverse to reach the surface. For these reasons we confine the discussion to electron-electron and electron plasmon scattering. A third energy loss process, surface plasmon scattering, which cannot be described by a mean free path is also discussed.

Electron-electron scattering in a free electron gas has been treated with varying degrees of refinement by Wolf (1954), Quinn (1962), Ritchie and Ashley (1965), Ritchie et al. (1969), Hamm (1968) and most recently by Kleinman (1971). These treatments are strictly valid only for a free electron gas in the high density limit, that is for $r_s < 1$ where r_s is the radius of the sphere equal in volume to the volume per electron measured in units of the Bohr radius. Better calculations are not available and these results have often been used to compare with experimental data (Quinn, 1963; Kanter, 1970) on real metals where $2 \leq r_s \leq 5$. The requirement that $r_s < 1$ is apparently not too stringent (Quinn, 1962) but Quinn (1963) has shown that the agreement that has been found between his theory (Quinn, 1962) and the values for the electron-electron mean free path in such non-free electron-like metals as Au and Ag is fortuitous.

A second type of calculation for the energy dependent mean free path is the constant matrix element calculation of Berglund and Spicer (1964a). This theory assumes that direct $\vec{k}$ conservation is unimportant and that the matrix elements connecting the initial and final states are constant. With those simplifications, the result becomes a double energy integration over the density of states of the metal. The chief advantage of this calculation is that it is not restricted to the free electron gas case but may be applied to any material whose density of states is known. It is useless, however, for absolute comparison with experimental data because the calculation gives only the energy dependence of the mean free path and not the absolute

value. Justification for the simple theory of Berglund and Spicer has been given by Kane (1967) who compared the simple theory with his own detailed calculations based upon band structure. For the case of silicon, Kane found agreement between the shapes of the two theories to within his statistical error.

Figure 8 shows the results of the several theories. Each has been evaluated for the case of aluminum using $r_s = 2$ and $E_F = 12$ eV as parameters. The Berglund and Spicer (1964a) theory was adjusted to give $\ell = 10$ Å at 15 eV. This was chosen arbitrarily to avoid confusing the figure and does not represent an estimate of the true magnitude.

Qualitative reasons for the differences in the results can be given. At the low energy end, the differences between Quinn's result and those of Ritchie and Ashley and Kleinman can be attributed to the exchange corrections introduced by the latter authors. Ritchie and Ashley used a proper antisymmetric form of the final state wave function while Kleinman evaluated certain corrections to the energy-dependent dielectric constant. These exchange corrections reduce the interaction cross section relative to the uncorrected result and give larger mean free paths.

The greater discrepancy at the intermediate energies has been attributed by Kleinman (1971) to inaccuracies in the numerical evaluations performed by Quinn (1962). At higher energies, the various theories merge into agreement.

The work of Hamm (1968) is not corrected for exchange but the effect of the exclusion principle has been applied at each intermediate state

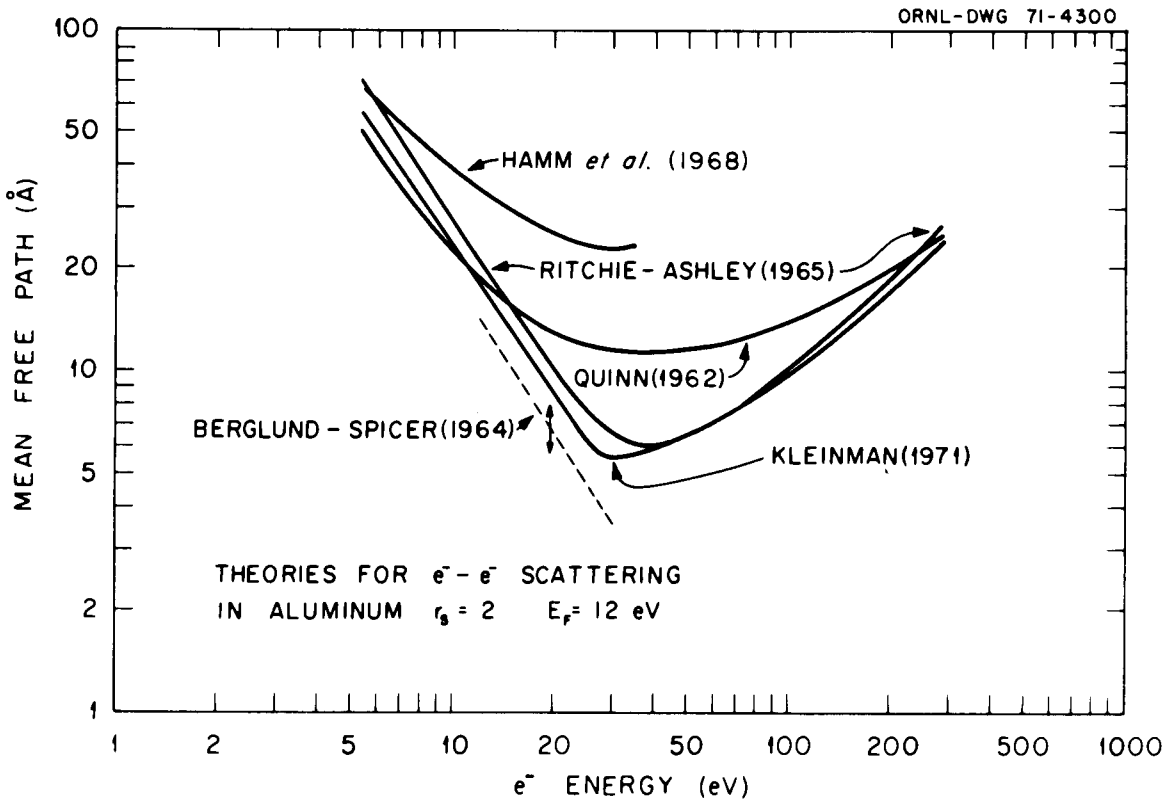

Figure 8. Theoretical electron-electron mean free paths for a free electron gas with the parameters of aluminum.

instead of only at the final state. This apparently has the effect of reducing interaction probabilities. The success of the Berglund and Spicer calculation in predicting the shape of the mean free path curve at lower energies is evident from Figure 8.

The second important type of inelastic scattering is electron-volume plasmon scattering. Electron-electron scattering can be important for electrons possessing only a few eV of energy, whereas volume plasmon scattering has a threshold that is somewhat higher than the volume plasmon energy of the metal. The mean free path for volume plasmon scattering ℓ_p, is (Ritchie et al., 1969; Quinn, 1962)

$$\ell_p = \frac{2a_o E}{E_P}\left[\ln\left(\frac{\sqrt{E_P + 1} - 1}{\sqrt{E} - \sqrt{E - E_P}}\right)\right]^{-1} \tag{47}$$

for electron energies well removed from the volume plasmon energy. In this equation, the energies are measured in units of the Fermi energy in such a fashion that E = 1 corresponds to an electron at the Fermi energy. The mean free path becomes infinite when the argument of the logarithm in Equation 47 approaches unity. Thus an estimate of the minimum energy that an electron must have to participate in an electron-plasmon scattering event, E_{min}, is obtained by setting the argument equal to unity.

$$E_{min} \approx E_P + 1 \tag{48}$$

This corresponds to an electron raised above the Fermi energy by an amount of energy equal to the plasma energy. A better estimate of the minimum energy has been given by Quinn (1962). Quinn found that near the threshold for plasmon excitation, the dispersion of the plasma oscillations results in an increase in the energy of the plasmons which can be excited by these low energy electrons. Quinn finds that

$$E'_P = E_P \left\{ 1 + \frac{6}{5E_P^2} \left[\left(1 + E_P \right)^{\frac{1}{2}} - 1 \right] \right\} \tag{49}$$

where E'_p is the corrected threshold plasma energy should be used in Equation 48 in place of E_p for accurate results. Quinn finds that if Equation 48 is used uncorrected, the threshold for volume placmon scattering in aluminum is 16 eV and if corrected by Equation 49, 19 eV. A more recent numerical calculation by Kleinman (1971), who was not restricted by the analytic approximation of Quinn gave $E_{min} = 23$ eV. Figure 9 shows the mean free path for plasmon scattering, the mean free path for electron-electron scattering (Ritchie et al., 1969) and the resultant attenuation length. A surprising result is that the attenuation length is as short as 3 Å for certain energies.

In addition to the volume losses just described, the possibility exists that an electron which crosses a metal-vacuum (or metal-dielectric) interface may excite a non-radiative surface plasmon oscillation and lose an

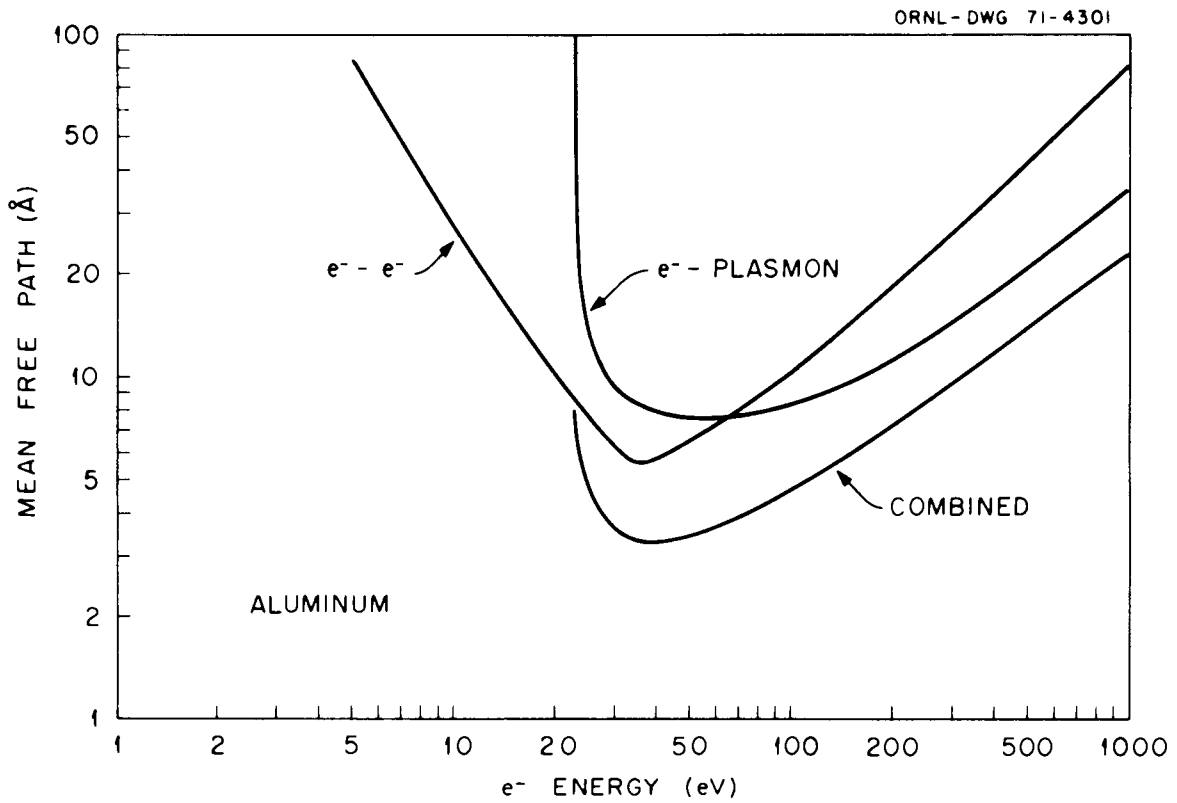

Figure 9. Theoretical mean free paths for electron-electron scattering, electron-plasmon scattering, and the effective mean free path for both types of scattering for a free electron gas with the parameters of aluminum.

amount of energy approximately equal to the surface plasmon energy. Figure 10 shows the dispersion relation for the non-radiative surface plasmon in a semi-infinite free electron gas. Although the creation of surface plasmon oscillations by high energy electrons is well established (Ritchie et al., 1969; Birkhoff, 1964; Raether, 1965), the creation of surface plasmons by relatively low energy electrons has only recently come under study. Stanford (1966), Thomas (1965) and Callcott and MacRae (1969) have suggested that surface plasmon excitation may play an important role in photoemission. Smith and Spicer (1969) have reported surface plasma losses in the alkali metals.

Several calculations have been made. Ritchie et al. (1969) have extended the higher energy (Born approximation) formalism to low energy and find that $\sim 25\%$ of 20 eV electrons incident upon a semi-infinite aluminum foil will experience a surface plasmon loss. Ngai et al. (1970) have calculated the surface plasmon effect on photoemission for ~ 10 eV photons and find for cesium that electrons which have experienced a surface plasmon loss constitute $\sim 50\%$ of the primary electrons. Grant and Ritchie (1970) find qualitative agreement with previous calculations.

The conclusions that can be drawn from the existing theoretical literature are that surface plasmon scattering is very important for electrons whose energies lie above the surface plasmon energy and that precise values of the loss probability are not presently available. Figure 11 gives the Born approximation result (Ritchie et al., 1969) for the probability

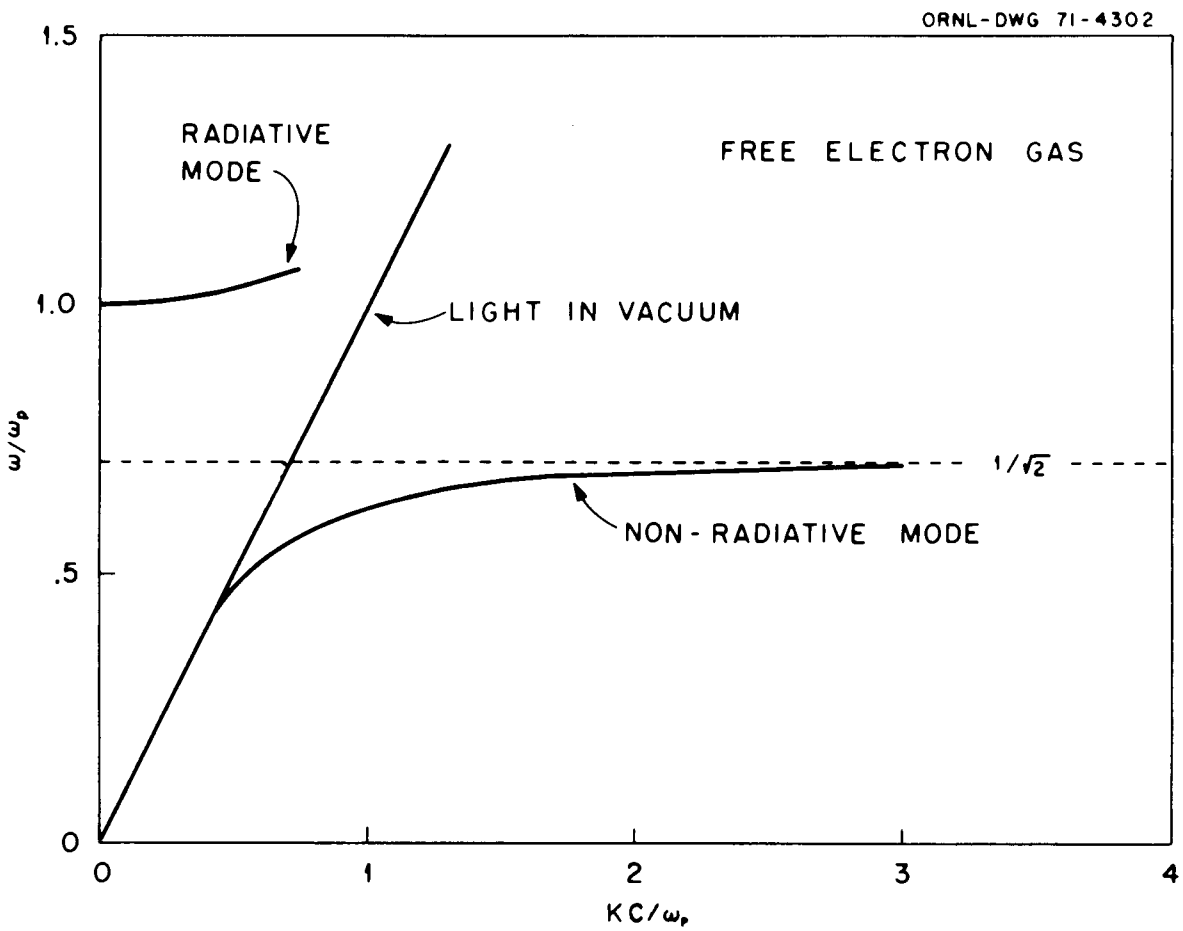

Figure 10. Dispersion relations for the radiative and non-radiative surface modes in a semi-infinite free electron gas.

These curves have been taken from Steinmann [W. Steinmann, Phys. Stat. Solidi 28, 437 (1968)].

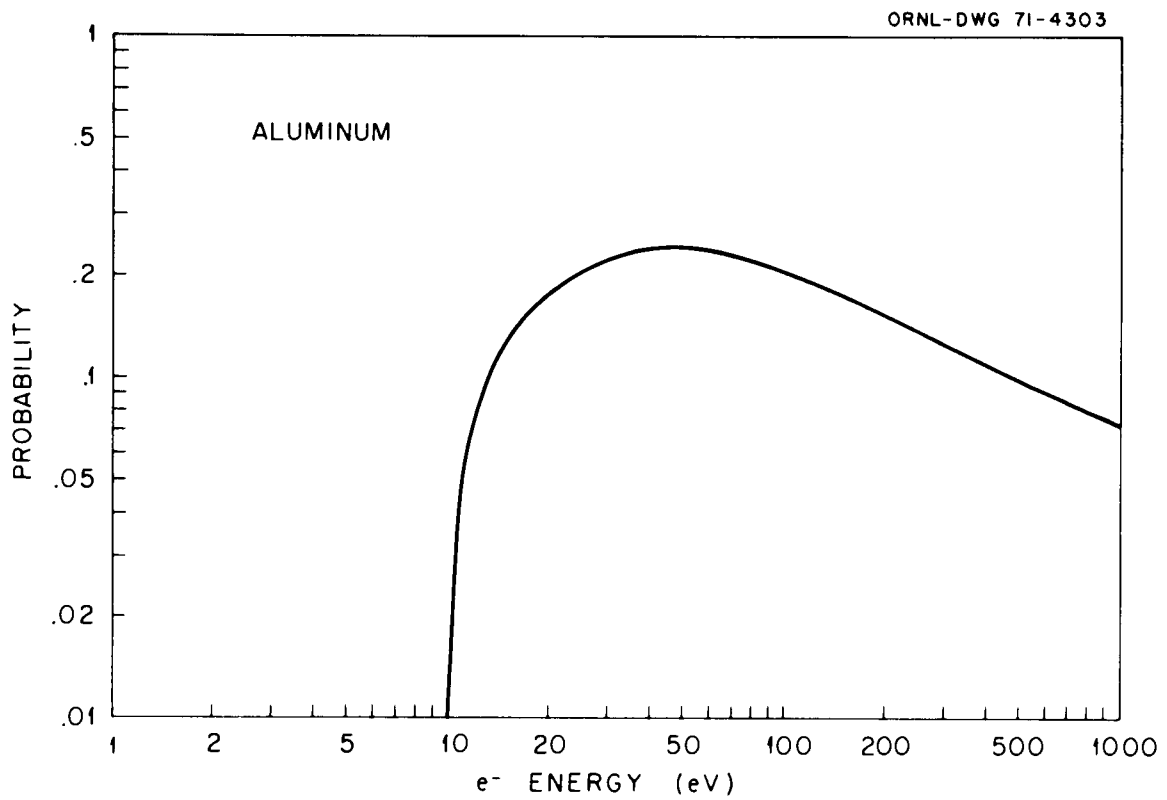

Figure 11. Theoretical probability that an electron will excite a non-radiative surface plasmon upon entering a semi-infinite free electron gas with the parameters of aluminum from a vacuum.

that an electron will excite a surface plasmon upon entering a thick aluminum foil from the vacuum. The curve should be considered correct only as to order of magnitude near 10 eV because the Born approximation becomes less valid as the threshold is approached. Although the calculation was performed for electrons entering aluminum from the vacuum, the results of Grant and Ritchie (1970) indicate that the probability of exciting a surface plasmon should be of comparable magnitude for the reverse direction.

V. NON-IDEAL SURFACE EFFECTS

The importance of the reflectivity as a parameter in the analysis of photoemission data is implied in the equations of Section II, this chapter. Although the reflectivity of an ideal (flat) metal-vacuum interface is given by Fresnel's equations, unavoidable surface roughness can lead to non-specular scattering, anomalous absorption, and absorption through excitation of non-radiative surface plasmons. Anomalous absorption has been found to be unimportant by Endriz and Spicer (1971a) for aluminum in the spectral region $\lambda > 1100$ Å and will not be treated here.

Elson and Ritchie (1970; 1971) have recently given theories which treat both scattering and absorption of photons by surface plasmons for a general surface characterized by an autocorrelation function and an rms surface height variation. The scattering theory is derived only for a free electron gas, but the surface plasmon absorption theory is applicable to a

general dielectric, and includes broadening due to the finite lifetime of the surface plasmon (lifetime broadening). We describe the results of Elson and Ritchie because their results are more general than those of previous investigators. The Ritchie and Elson papers (1970; 1971) as well as the Endriz and Spicer papers (1971a; 1971b) contain numerous references to earlier work.

Elson and Ritchie use first order perturbation theory to calculate the probability that a photon normally incident on a rough metallic surface will create a surface plasmon. They express this probability as a decrease in reflectivity, ΔR_{sp}.

$$\Delta R_{sp} = \frac{\omega^4}{c^4} \frac{\epsilon_1^2}{\left(\epsilon_1^2-1\right)^2\left[-\left(\epsilon_1+1\right)\right]^{1/2}} \left\{3(\epsilon_1-1) + \omega\frac{d\epsilon_1}{d\omega}\left[1-\left(\frac{\epsilon_1+1}{\epsilon_1}\right)^{1/2}\right]^2\right\}\delta^2 g(k) \tag{50}$$

In this equation, c is the velocity of light, ω is the photon angular frequency, ϵ_1 is the real part of the complex dielectric constant, δ is the rms surface roughness, and g(k) is the fourier transform of the auto-correlation function. The wave number, k, is related to the angular frequency, ω, by the surface plasmon dispersion relationship

$$k = \frac{\omega}{c}\sqrt{\frac{\epsilon_1}{1+\epsilon_1}} \tag{51}$$

Figure 10, page 46, shows the dispersion relation for the non-radiative surface

plasmon under consideration here as well as the dispersion relation for the radiative surface plasmon which is discussed later. The important point made in Figure 10, page 46, is that the dispersion curve for the non-radiative surface plasmon lies entirely to the right of the photon dispersion curve and therefore the momentum of the surface plasmon parallel to the surface is always greater than the momentum of a photon of the same energy. In order to achieve photon surface plasmon coupling, momentum must be added in the plane of the surface. An ideal or perfectly smooth surface cannot add momentum; however, a rough surface with bump dimensions on the order of k^{-1} can supply the required momentum. The necessity for roughness is also clear from Equation 50 which vanishes for a perfectly smooth surface ($\delta^2 = 0$).

Damping of the final states can be included in a standard fashion by folding ΔR_{sp} into a Lorentzian damping function

$$\Delta R'_{sp} = \int_0^{\omega_{sp}} \Delta R_{sp} \frac{\gamma/2}{\omega'^2 + (\gamma/2)^2} \, d\omega' \tag{52}$$

The quantity γ is the sum of the damping rates for all the damping processes.

The damping processes that have been considered up to the present are listed.

1. SP $(\omega, \vec{k}) \rightarrow e^-$: A surface plasmon decays by exciting an electron in the volume of the metal. Little momentum is transferred and

the transition is vertical in the reduced zone scheme. Surface roughness is not required (Elson and Ritchie, 1971).

2. SP $(\omega, \vec{k}) \rightarrow e^-$: A surface plasmon decays by exciting an electron in the metal. The surface plasmon momentum is significant and the transitions are non-vertical in the reduced zone scheme. This mechanism applies only to high $\vec{k}$ surface plasmons and does not require surface roughness (Elson and Ritchie, 1971).

3. SP $(\omega, \vec{k}) \rightarrow e^-$: A surface plasmon decays by exciting an electron near the interface, Momentum is conserved by the surface barrier. Surface roughness is not required (Wilems and Ritchie, 1968; Endriz and Spicer, 1971b).

4. SP $(\omega, \vec{k}) \rightarrow \hbar\omega$: A surface plasmon radiates its energy into a single photon. Surface roughness is required to conserve momentum. This process is the inverse of that described by Equation 50 (Elson and Ritchie, 1971).

5. SP $(\omega, \vec{k}) \rightarrow$ SP $(\omega, \vec{k}')$: A surface plasmon is scattered by the surface roughness into a new momentum state. Energy and $|\vec{k}|$ are unchanged (Elson and Ritchie, 1971).

Surface plasmon damping is important in photoemission for two reasons. Firstly, all of the damping mechanisms serve to broaden the dip in reflectance near the surface plasmon energy. Secondly, those processes which give rise to a single electron transition (processes 1-3) can contribute directly to the observed photocurrent. This process has been observed by

Endriz and Spicer (1970; 1971b). Damping by processes 4 and 5 which are dependent upon the surface roughness are not important for our considerations because fairly smooth foils were used. Process 2 in which momentum is supplied to the electron by the surface plasmon is important only for very high-k surface plasmons. Process 1 provides most of the damping strength which contributes to broadening of the reflectance dip, and as we shall show, processes 1 and 3 provide similar contributions to the external photocurrent.

Volume damping (process 1) in which the surface plasmon decays via a one electron transition in the metal yields a damping rate of (Elson and Ritchie, 1971)

$$\gamma_{vol}(\omega') = \frac{\omega\, \epsilon_2'}{\epsilon_1(\epsilon_1 + 1) + \frac{\omega'}{2} \left.\frac{d\epsilon_1}{d\omega}\right|_{\omega'}} \tag{53}$$

From the dispersion relation (Equation 51) we see that $k \to \infty$ as $\epsilon_1 \to -1$. Thus the solution of $\epsilon_1(\omega) = -1$ gives the asymptotic value of the surface plasmon angular frequency. Similarly, as $\epsilon_1(\omega) \to -1$ Equation 53 takes the asymptotic form.

$$\gamma_{vol}(\omega') \to \frac{2\epsilon_2}{\left.\frac{d\epsilon_1}{d\omega}\right|_{\omega'}} \tag{54}$$

Surface damping (process 3) has been treated in the first order by Wilems and Ritchie (1968) and by Endriz and Spicer (1971b). The treatment

of Wilems and Ritchie (1968) is based on first order perturbation theory. They calculate the transition rates for electron emission into the vacuum, into bound metallic states and into free metallic states. The treatment of Endriz and Spicer is semi-classical and assumes that the normal component of the surface plasmon field interacts with the metal in a fashion analogous to the surface photoelectric effect as treated by Mitchell (1934; 1936).

The Wilems and Ritchie treatment appears to be superior in that it gives the absolute magnitude of the transition probability for electrons into the vacuum. For the discussion of the Wilems and Ritchie theory, only, we use κ for the surface plasmon wave vector and k for the electron wave vector. Wilems and Ritchie find for the transition rate of surface plasmons into external electrons, γ_{FV}, that

$$\gamma_{FV} = \frac{2V_H\kappa}{\pi w^2}(w^2+1)^2 \int_{Re(w^2-1)^{1/2}}^{f} dx \frac{x^2(f^2-x^2)(x^2+1-w^2)^{1/2}}{\left[\left(x^2+1\right)^{1/2}+\left(x^2+1-w^2\right)^{1/2}\right]^2} \tag{55}$$

In this equation,

$$x = \frac{k_{oz}}{k_r}, \qquad w = \frac{k_w}{k_r}, \qquad f = \frac{k_F}{k_r}, \qquad \text{and} \quad V_H = \frac{e^2}{\hbar}$$

The z component of the electron wave vector is k_{oz}, k_w is the wave vector of an electron at the vacuum level, k_F is the wave vector of an electron at the Fermi level, and k_r is related to the surface plasmon

angular frequency through the expression

$$k_r = 2m\omega_\kappa/\hbar \tag{56}$$

The quantity ω_κ is related to the surface plasmon wave vector, κ, through the surface plasmon dispersion relation, Equation 51. Similar expressions are found for the probability of creating bound and free electrons in the metal.

The expressions described above have been evaluated by Wilems and Ritchie for the cases of magnesium (1968) and aluminum (private communication). In their notation γ_{FV}, γ_{FM}, and γ_{BM} are the transition rates for free electrons into the vacuum, into the metal and into bound metallic states, respectively. They find for magnesium that $\gamma_{BM} = 1.5 \times 10^{14}\kappa$, $\gamma_{FM} = 8 \times 10^{14}\kappa$, and $\gamma_{FV} = 1.37 \times 10^{15}\kappa$, and for aluminum that $\gamma_{BM} = 2.44 \times 10^{15}\kappa$, $\gamma_{FM} = 1.53 \times 10^{15}\kappa$, and $\gamma_{FV} = 2.22 \times 10^{15}\kappa$. In these expressions, κ is expressed in $(\mathring{A})^{-1}$ and γ in sec^{-1}.

If we let γ_T be equal to the sum of all the damping, then the probability that a surface plasmon decays by the ith process, P_i is simply

$$P_i = \gamma_i/\gamma_T \tag{57}$$

If $P_{i,e}$ is the probability that decay by the ith process results in an external electron, then the total number of external electrons observed

for each plasmon created, Q_{sp}, is just

$$Q_{sp} = \sum_{i=1}^{N} P_{i,e} \; P_i \tag{58}$$

It is interesting to compare the two dominant processes, emission from the volume (process 1, page 50) and emission by the surface (process 3, page 51) with each other and with the analogous photoelectric process. For volume decay of plasmons, $P_{i,e}$ can be evaluated from Equation 19 by assuming that the surface plasmon fields behave as photon fields for volume excitation of electrons (Endriz and Spicer, 1970). In place of the photon attenuation coefficient, α, one uses 2k because the dependence of the surface plasmon fields upon distance to the surface is just $e^{-k(z)}$ (Stern and Ferrell, 1960). For magnesium, considering 7 eV photons and surface plasmons and a typical value of k of .01 $\mathring{A}^{-1}$ (corresponding to $k/k_p = 2$ in Figure 10, page 46) we obtain the following results. The yield for photons, that is the number of external primary electrons expected per absorbed photon, is $Q_{pe} = .0130$. The quantum yield for external electrons from surface plasmon volume decay $Q_{sp,v} = .0243$ and that for external electrons from surface plasmon surface decay is $Q_{sp,s} = .0146$. The remarkable conclusion made from this calculation is that surface plasmons can be several times more efficient than photons in creating external electrons.

Diffuse scattering from a rough surface described by an autocorrelation function and an rms surface roughness has been treated recently by Elson and Ritchie (1971). The treatment is valid only for a free electron gas in the reflecting region, $\omega < \omega_p$, but represents an improvement over the earlier theories (Bennett and Porteus, 1961) because it includes the effects of the autocorrelation length on the scattering probability.

The Elson and Ritchie calculation is done for the normal incidence case. They find for light scattered with its electric vector perpendicular to the plane of observation, (s polarization) that the differential scattering probability is

$$\frac{dP^s}{d\Omega} = \frac{\delta^2}{\pi^2}\left(\frac{\omega}{c}\right)^4 \cos^2\theta \cos^2\varphi\, g\left(\frac{\omega}{c}\sin\theta\right) \tag{59}$$

The polar angle is ϕ and θ is the azimuthal angle. The differential solid angle, $d\Omega$, is $d\phi\, d(\cos\theta)$, δ is the rms roughness, and the function g is the Fourier transform of the autocorrelation function.

The equivalent expression for light scattered with its electric vector paralle to the plane of observation (p-polarized) is

$$\frac{dP^p}{d\Omega} = \frac{\delta^2}{\pi}\left(\frac{\omega}{c}\right)^4 \cos^2\theta \cos^2\phi \left\{\frac{\sin^2\theta - \epsilon}{\sin^2\theta - \epsilon\cos^2\theta}\right\}$$

$$\left[1 + \frac{2\sqrt{-\epsilon}}{\sqrt{\sin^2\theta - \epsilon\cos^2\theta}}\right]^2 g\left(\frac{\omega}{c}\sin\theta\right) \quad . \tag{60}$$

The quantity ϵ is the dielectric constant and is real because of the free electron gas approximation, that is $\epsilon = 1 - \omega^2/\omega_p^2$.

A quantity of interest for experimental purposes is the total light scattered out of the specular beam. For the near normal incidence case, this can be found by integrating Equations 59 and 60 over the solid angle not subtended by the detector. The total observed decrease in reflectance due to diffuse scatter is then

$$\Delta R_{scatt} = \int_{\Omega \neq \Omega'} d\Omega \left(\frac{dP^s}{d\Omega} + \frac{dP^p}{d\Omega} \right) \tag{61}$$

where Ω' is the solid angle subtended by the detector.

A commonly used analytic expression for the transformed autocorrelation function is the Gaussian form (Crowell and Ritchie, 1970),

$$G\left(\frac{\omega}{c} \sin \theta\right) = \pi\sigma^2 e^{-\frac{\sigma^2 \omega^2 \sin^2 \theta}{c^2}} \tag{62}$$

where σ is called the autocorrelation length. For this case, Equation 59 may be integrated in terms of the error function to give

$$P^s = \frac{2\omega\delta^2}{c\sigma} e^{-\frac{\omega^2\sigma^2}{4c^2}} \left\{ \sqrt{\pi}\ \mathrm{Erf}\left(\frac{\omega\sigma}{2c}\right) - \frac{\omega\sigma}{2c} e^{-\frac{\omega^2\sigma^2}{4c^2}} \right\} \tag{63}$$

assuming that Ω' is unimportant. No such simple form is possible for

the p component (Equation 60) and computer evaluation is necessary. Figure 12 gives an example of the broadened surface plasmon resonance as well as the effects of diffuse scatter. Here the curve labelled "scattered" is corrected for the diffuse scatter of photons out of the specularly reflected beam.

VI. PHOTOELECTRIC MANIFESTATION OF THE OPTICAL PLASMA RESONANCE

The previous discussions of surface plasmons were concerned with non-radiative surface plasmons. Coupling to the non-radiative branch must be accomplished by electrons (Section IV, this chapter) or mediated by surface roughness (Section V, this chapter). In this section we discuss the radiative mode of the surface plasmon which may exist in thin metal foils whose thickness, t, is $\leqslant \frac{c}{\omega_p}$. Figure 10, page 46, shows the radiative mode of the surface plasmon. The radiative branch is the solution of the following equation (Kliewer and Fuchs, 1967).

$$\epsilon = -\sqrt{\frac{\epsilon \frac{\omega^2}{c^2} - k^2}{k^2 - \frac{\omega^2}{c^2}}} \tan \frac{t}{2} \sqrt{\epsilon \frac{\omega^2}{c^2} - k^2} \tag{64}$$

The component of the wave vector parallel to the surface, k, is related to the angular frequency by

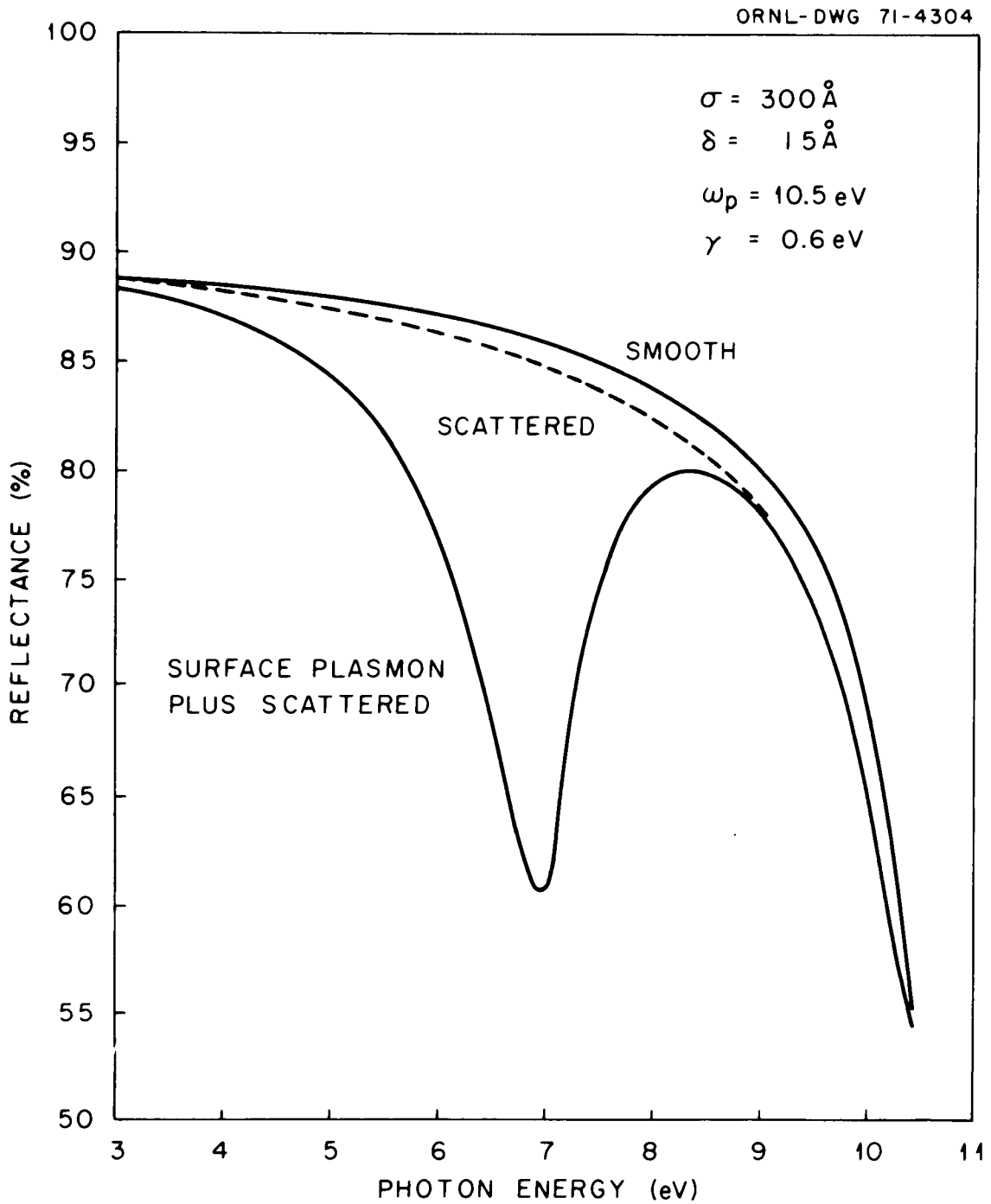

Figure 12. Theoretical change in reflectance due to diffuse scatter and surface plasmon absorption of a free electron gas with the parameters of magnesium.

$$\frac{kc}{\omega} = \sin\theta$$

where θ is the angle of incidence (or emission) of the photon. Solutions to Equation 64 are necessarily complex even though ϵ may be real; thus Figure 10, page 46, actually shows Re(ω) vs. Re(k). These complex solutions imply radiative damping. Actually Equation 64 has many solutions but only the solution shown in Figure 10, page 46, is of experimental importance; the higher order solutions are very strongly damped.

Kliewer and Fuchs (1967) have shown that for thin films ($t < \frac{c}{\omega_p}$) and small angles ($\theta < 45°$) Equation 64 has the following solutions.

$$\mathrm{Re}(\omega) = \omega_p\left(1 + \frac{\omega_p^2 t^2}{8c^2}\tan^2\theta\right) \tag{65}$$

$$\mathrm{Im}(\omega) = \frac{\omega_p^2 t}{4c}\sin\theta\tan\theta \tag{66}$$

The quantity Im(ω) is related to the lifetime for radiative damping, τ_R, by

$$\tau_R^{-1} = \frac{1}{2}\mathrm{Im}(\omega) \tag{67}$$

The radiative surface plasmon is damped either radiatively as indicated above or intrinsically by creating an electron-hole pair in the metallic film. Intrinsic damping may result in an observable current if the plasma energy of the film is greater than the work function.

Excitation of the radiative surface plasmon mode requires a component of the electric field vector normal to the surface. This requirement implies that only p (parallel) polarized light incident non-normally can excite non-radiative surface plasmons. The actual excitation probability is quite complicated (Steinmann, 1968) but rises monotonically from zero as the angle of incidence of p polarized light is increased from zero. This in turn implies that a resonance should occur in the relative photoelectric yield at angles greater than zero. Here we are defining the relative yield as

$$Y_{rel} = Y(\theta, h\nu)/Y(0, h\nu) \tag{68}$$

The location of the maximum in the resonance should be governed by Equation 65 and the width should be equal to the intrinsic width plus the width due to radiation damping (Equation 66). This resonance has been observed as early as 1938 (Ives and Briggs, 1938) but has only recently been studied quantitatively (Feuerbacher and Fitton, 1970). Plots of the resonance maximum vs. $\tan^2 \theta$ should give a straight line which should extrapolate to the bulk plasmon frequency as $\theta \to 0$. Plots of the width of the resonance vs. $\sin \theta \tan \theta$ should give a straight line whose intercept at $\theta = 0$ should give the intrinsic width. In addition the thickness of the film should be consistent with the slope of either equation.

VII. RECENT ADVANCES IN PHOTOEMISSION THEORY

Throughout this work it is tacitly assumed that volume photoemission is a three step process consisting of excitation, transport and escape. It is also assumed that the electrons are isotropically distributed in space. Both of these assumptions have much experimental evidence to support them, and the isotropic distribution assumption is especially reasonable for studies in amorphous evaporated films. Recently, however, a one step model for photoemission from an interacting electron gas has been proposed (Sutton, 1970) and the non-isotropic character of photoemission from single crystals has been treated (Mahan, 1970). The work of Mahan (1970) while very important is not relevant to the present work and our only purpose is to make note of it. The reformulation of photoemission as a one-step process, however, could be significant. The work available at the present time includes only the surface photoeffect. The author (Sutton, 1970) indicates that the work will be extended to the volume process, and experimental testing of his results will prove interesting.

CHAPTER III

EXPERIMENTAL APPARATUS

I. GENERAL CONSIDERATIONS

The experimental apparatus was designed to measure the photoelectric and optical properties of evaporated films, prepared *in situ*, in the spectral region from 500 Å to 7000 Å.

The basic apparatus is shown schematically in Figure 13. The components were a source of radiation, a means of dispersing the radiation, a beam monitor, a high vacuum experimental chamber joined optically to the monochromator with an appropriate window and the electronics necessary to handle small currents. Much of the apparatus was in existence at the beginning of the study (Stanford *et al.*, 1966; Vehse and Arakawa, 1966). The changes and additions made during the course of this study were limited to the windows, the electron retarding can, the electronics for directly measuring the photoelectron energy distributions and the film thickness monitor. The changes were made to reduce sample contamination and to increase the speed and accuracy of the measurements. For completeness the entire apparatus is described.

ORNL DWG. 70-14495

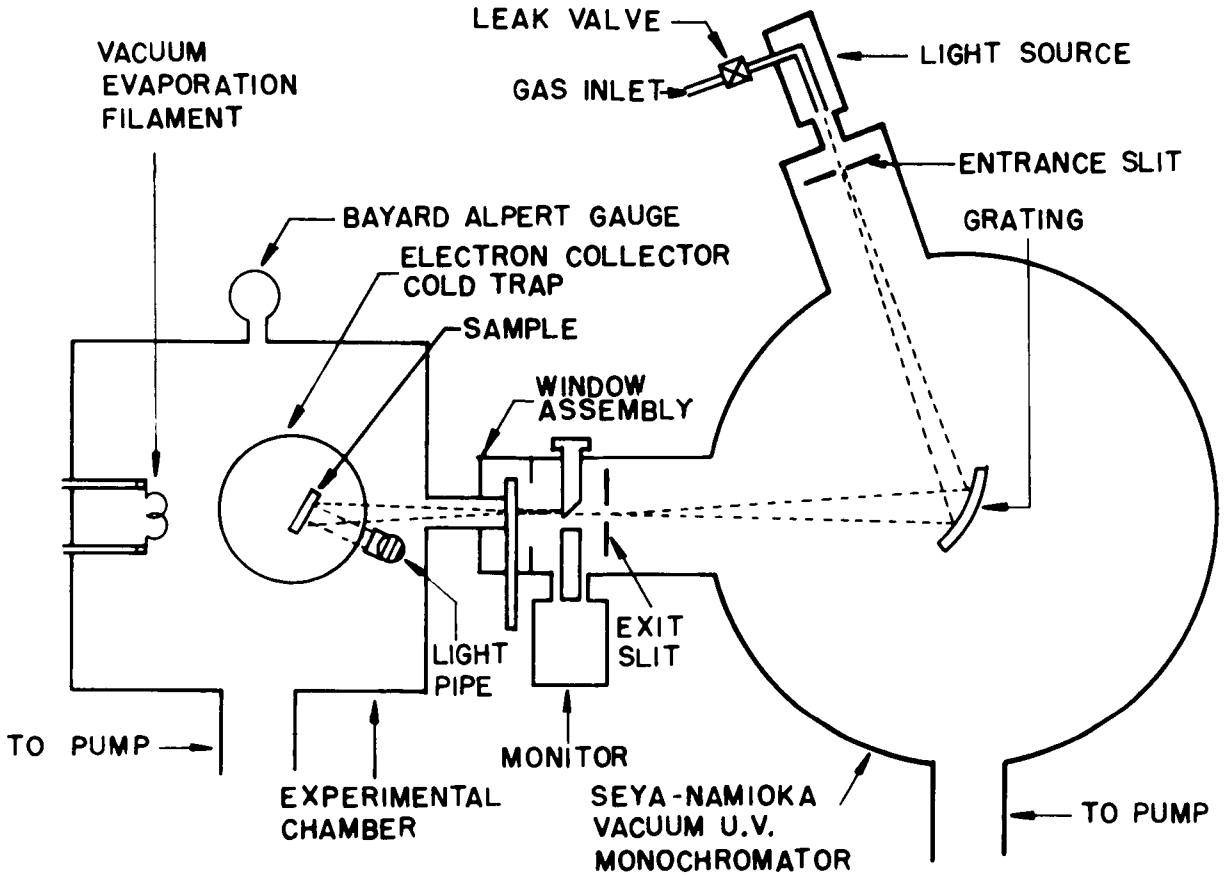

Figure 13. Top view of the experimental apparatus.

II. SOURCES OF RADIATION

Ultraviolet radiation was produced by maintaining a continuous or an interrupted electrical discharge in a gas-filled glass or boron nitride capillary tube. The arrangement is shown schematically in Figure 14.

In the continuous discharge mode, gases such as hydrogen, helium, or the nitrogen-oxygen mixture of air produced usable light to wavelengths as short as 900 Å. These gases were used at pressures of .25 - 1.0 Torr. In addition, helium produces a strong line (the well known He resonance line) at 584 Å. In general, however, for radiation below 1000 Å, an interrupted discharge was employed in gases such as nitrogen, argon, or air. The gas pressures used in the interrupted discharge mode were .05 - .2 Torr. The shorter wavelength lines produced by the interrupted discharge mode were atomic spectral lines from multiply ionized atoms.

The source of power for the light source is shown schematically in Figure 15. The D.C. high voltage supply was a Sorenson Model 2012-250 capable of producing up to 250 mA at 12,000 V. The resistor bank served three important functions. In the continuous discharge mode it permitted a large starting voltage to be built up across the light source while limiting the current when the source started. During operation, the resistor bank acted as ballast which helped to smooth out slight impedance changes in the gaseous discharge. In the interrupted discharge mode, the resistor bank functioned as the resistance of the RC charging circuit. The interrupted

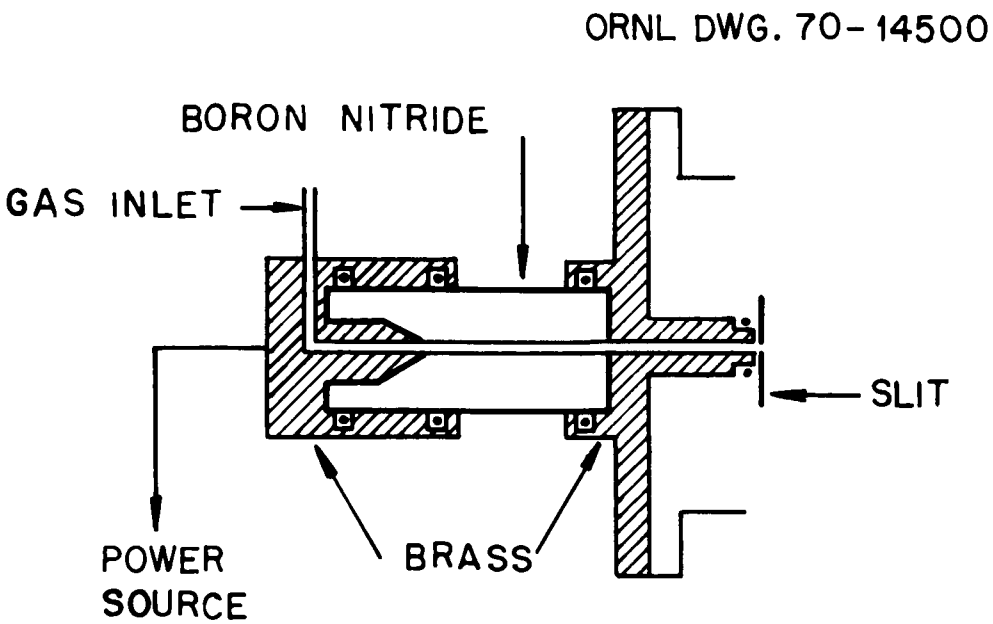

Figure 14. Schematic diagram of the light source.

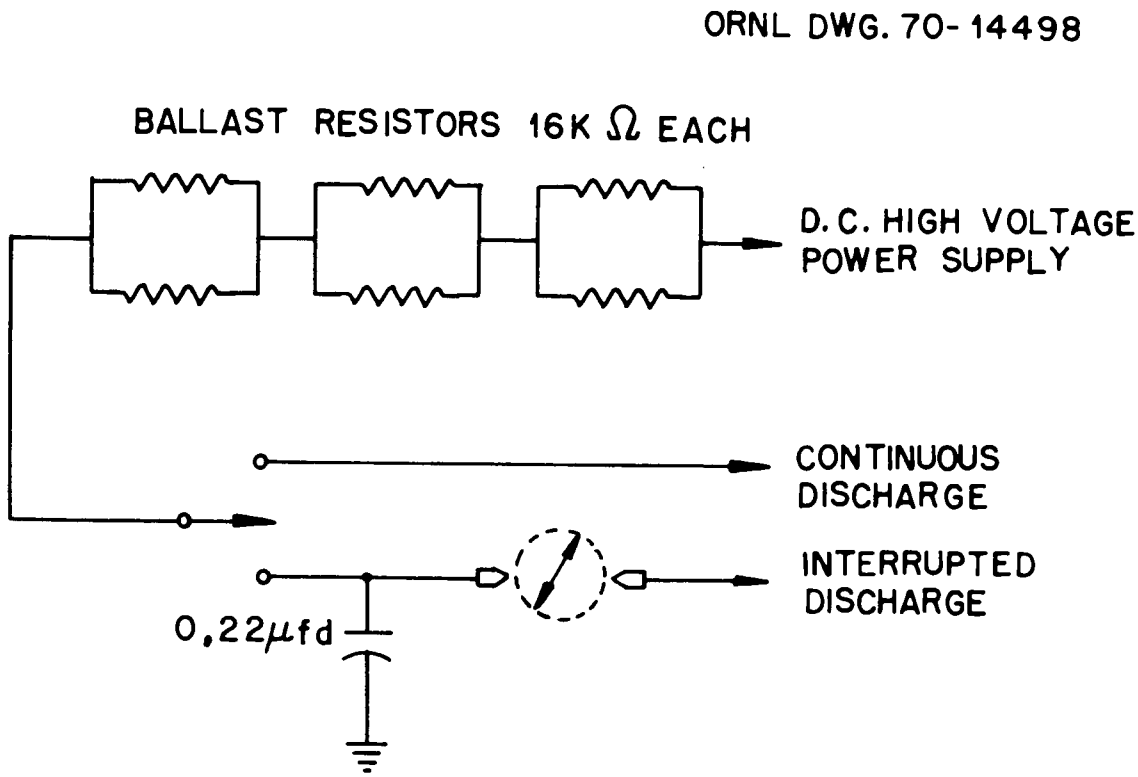

Figure 15. Schematic diagram of the light source power supply.

discharge was triggered at 53 cycles per second by the tungsten rotary spark gap unit. The capacitor used was a .22 μF radar unit designed for pulsed operation.

The use of the light source in the continuous discharge mode was entirely free from complications. Use of the interrupted discharge mode, however, was accompanied by instabilities in the intensity and by radio frequency noise which interfered with the electronics unless controlled by strict attention to shielding and grounding. The intensity instabilities were minimized by careful adjustment of the gas pressure and the spark gap clearance and by periodic cleaning of the bore of the capillary tube.

Occasionally, an Oriel Model C-60-30 high pressure xenon arc lamp was used when high intensity radiation was needed above ~2500 Å.

III. MONOCHROMATOR

Radiation from the various sources was dispersed in a Seya type vacuum ultraviolet monochromator (MacPherson Model 235). The dispersing element was a Bausch and Lomb 600 lines per mm replica grating. The grating was blazed for 1500 Å and was overcoated with aluminum and magnesium fluoride to enhance and preserve the reflectivity. The monochromator had adjustable entrance and exit slits. Linear wavelength scans could be made at a variety of speeds. No differential pumping was employed but the monochromator was equipped with a six-inch NRC Diffusion Pump to handle the gas load from the light source. The monochromator was equipped

with a valve in each arm so that the light source and/or the chamber could be let up to atmospheric pressure without disturbing the vacuum in the monochromator.

IV. THE BEAM MONITOR

The purpose of the beam monitor was to monitor the radiation issuing from the monochromator for fluctuations and to act as a secondary intensity standard. The position of the beam monitor in the equipment can be seen in Figure 13, page 64. Within the beam monitor a fraction of the beam (usually 50%) struck a sodium salicylate coated wedge. The sodium salicylate acted as a wavelength shifter and fluoresced with a broad emission spectrum centered at $\lambda = 4200$ Å. The fluorescence was directed to an end window photomultiplier tube (EMI 9524B) via a short pyrex light pipe. The coating of sodium salicylate was applied to the wedge by spraying a nearly saturated solution of 190 proof ethyl alcohol from an artist's airbrush. After this sodium salicylate had aged several months it was found to be stable enough to use as a secondary intensity standard. When the absolute maximum intensity was desired, at the expense of the beam monitoring capability, the wedge could be withdrawn allowing the entire beam to pass into the experimental chamber.

V. THE WINDOW ASSEMBLY

The main purpose of the window assembly was to optically join the monochromator to the experimental chamber while separating the mid 10^{-9}

Torr vacuum of the chamber from the $\sim 10^{-5}$ Torr vacuum of the monochromator. At longer wavelengths, certain window materials served to prevent a second order radiation from reaching the experimental chamber.

Most photoelectric experiments are performed using quartz windows down to 1600 Å and magnesium fluoride or lithium fluoride windows to 1150 Å or 1050 Å, respectively. At wavelengths shorter than 1050 Å, open window techniques are usually employed. Even though differential pumping can maintain substantial pressure differences between systems, streaming still exists, and the effective pressure on a sample aligned with the optical axis of the monochromator can be much higher than off-axis pressure measurement would indicate. For this reason, an effort was made to find and use windows in the spectral region below 1050 Å.

The position of the window assembly is shown in Figure 13, page 64. A flat stainless steel plate with three rectangular apertures was held perpendicularly to the beam against an O-ring seal slightly larger than the apertures. Window materials were sealed to two of the apertures, and the third was left open for use during pumpdown and when open window measurements were desired. A linear motion feedthrough was used to position the desired window in the beam.

The window materials found suitable for this study were quartz ($\lambda > 1600$ Å), lithium fluoride ($\lambda > 1050$ Å), indium (1000 Å $> \lambda >$ 750 Å), and tin (800 Å $> \lambda >$ 500 Å). Figure 16 shows the transmission of various windows. The aluminum was not used in this study but is shown for

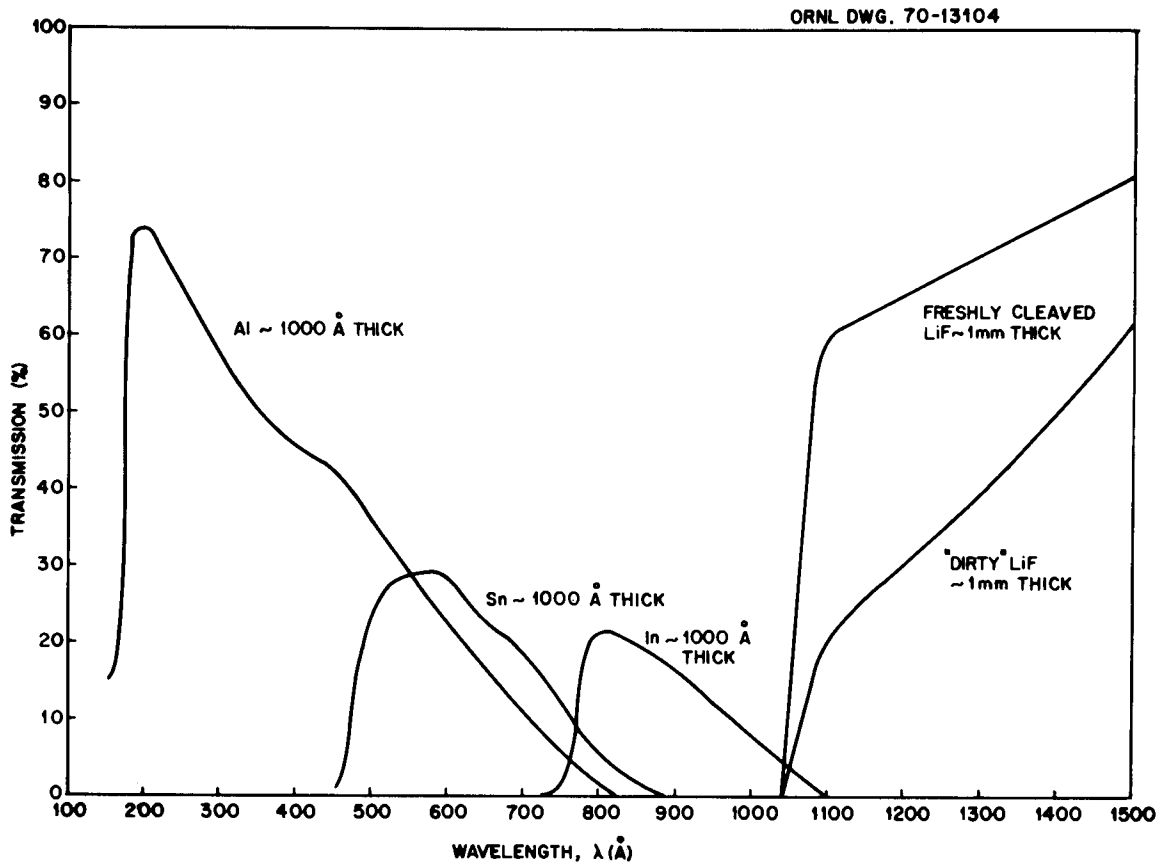

Figure 16. Transmission characteristics of lithium fluoride, indium, tin, and aluminum windows.

The transmission of aluminum and tin is from Hanson (W. F. Hanson, unpublished data).

reference. It can be seen that virtually any part of the spectrum that is of interest to investigators of photoemission processes can be transmitted through at least one of these windows.

The quartz and lithium fluoride windows were cemented to the aperture plate with Torr-Seal. The first step in the preparation of thin metallic windows was to vacuum evaporate about 1000 Å of the metal onto a sugar-coated glass microscope slide. The slide was then dipped slowly at a grazing angle into warm water where the sugar dissolved and the metallic film floated on the water. After the film was thus "floated off" it was picked up directly on the removable aperture rate of the window assembly. The effectiveness of these thin metallic windows was such that they transmitted ~20% of the light incident upon them and still separated vacuums of $\sim 10^{-9}$ Torr and 10^{-5} Torr.

The transmission characteristics of tin and the spectrum of the continuous discharge in helium (Samson, 1967) were exploited to give a very intense source of monochromatic light at 584 Å. For this case the tin window acted as a band pass filter which passed about 20% of the 584 Å He resonance line but excluded all other lines in the helium spectrum. Consequently, the normal grating was replaced with a gold mirror which afforded a factor of ten increase in the intensity and allowed us to calculate readily the polarization of the light.

VI. THE EXPERIMENTAL CHAMBER

A side view of the experimental chamber is presented schematically in Figure 17. In the figure, the cross-hatched areas represent electrical insulation. The chamber was essentially a stainless steel cube, 18 inches on a side with conflat flanges machined on five sides. Copper gaskets made the seals for the infrequently removed flanges and a viton O-ring, used without grease, made the seal on the often removed flange which contained the vacuum evaporation equipment and the observation window.

The aluminum sample holder was designed to accept a standard microscope slide as a substrate. Rotary motion permitted measurements of photoemissive and optical properties as a function of angle. Linear motion allowed the sample to be removed from the beam so that the incident light could be measured with the light pipe. A viton O-ring made the seal for the sample holder. The electrical connection from the sample holder to the outside of the chamber was made down the center of the one-half inch diameter stainless steel sample holder rod. Silver conducting paste (DuPont, silver preparation # 4817) made the connection from the sample to the sample holder.

The light pipe was fabricated from one-half inch diameter pyrex glass. The end of the light pipe was coated with ~ 1.5 mg/cm^2 of sodium salicylate to act as a wavelength shifter. The light pipe passed through a rotary viton O-ring seal at the top of the chamber. There it was joined

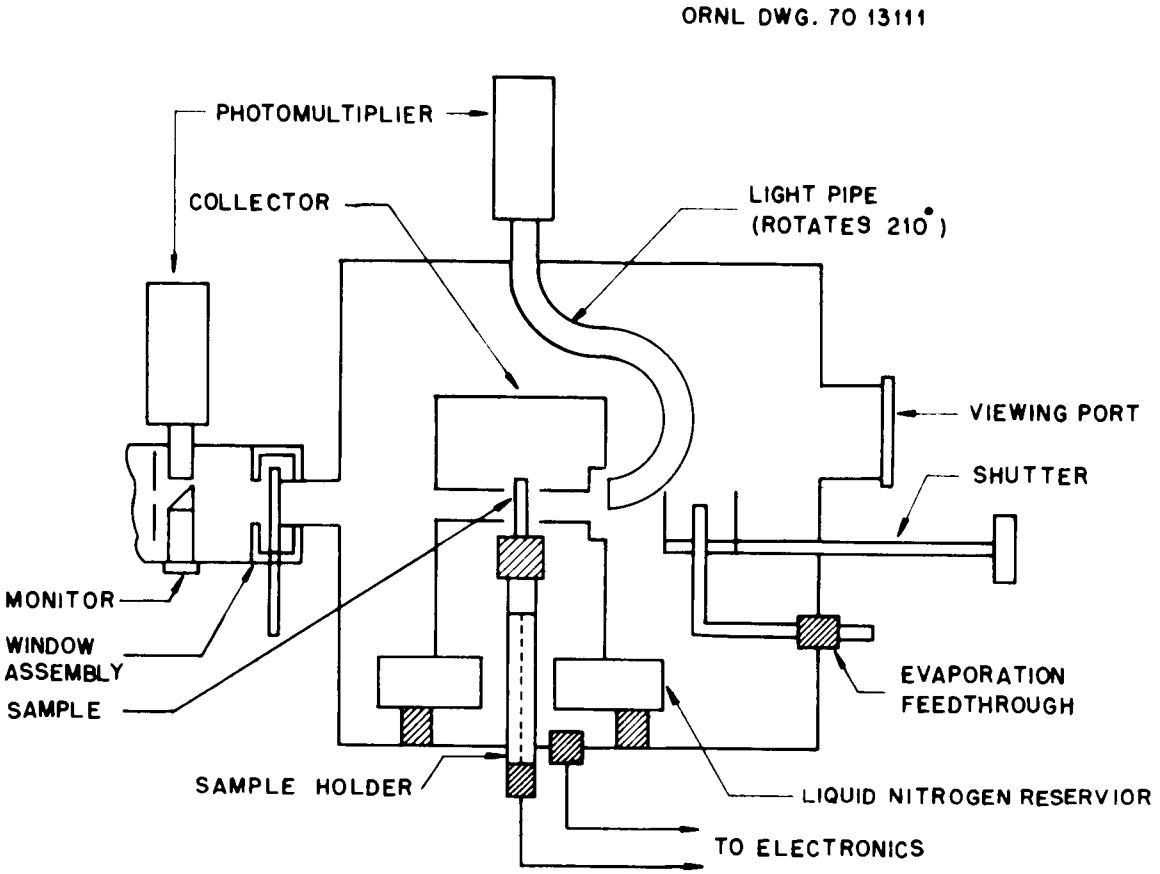

Figure 17. Side view of experimental chamber.

to an EMI 9524B photomultiplier tube with a transparent silicon compound (Dow Corning # C-2-0057). This silicon compound had the same index of refraction as glass and minimized the light loss due to reflection at the interface.

The light pipe was used to measure the incident and reflected beam intensity. Because the light pipe was outside the electron collector, reflectance and photoemission measurements could be made simultaneously without worrying about distortion of the collecting or retarding fields.

The electron collector also shown in Figure 17 was a four-inch diameter, gold plated copper cylinder. Although a point source and a spherical collector comprise the ideal geometry for the retarding potential method of measuring energy distribution, overriding considerations conspire to make the easily constructed cylinder a reasonable choice. These overriding considerations include residual magnetic fields, the necessity for a finite emitter, apertures in the collector and possible work function variations (DiSteffano and Pierce, 1970).

The collector was attached to a liquid nitrogen reservoir and acted as a cold trap to improve the vacuum in the vicinity of the sample. Unlike the screen grid that this collector-cold trap replaced, this collector could be easily cleaned each time the chamber was opened. The improvements in the energy distributions and the sample life attributed to this combination electron collector-cold trap are treated in Chapter V.

The arrangement for vacuum evaporating metal onto the substrate is also shown in Figure 17, page 74. Metals were evaporated from a resistance heated tungsten filament. The shutter had two blades on a common rotary shaft. One blade shielded the substrate and the other shielded the quartz crystal thickness monitor. The viewing port permitted visual observation of the evaporation and thickness of the film. The film thickness monitor was calibrated by comparing the monitor readings to the thickness of the films as measured interferometrically.

VII. ELECTRONIC EQUIPMENT

The electronic equipment for measuring the yields and the energy distribution curves was built or assembled from stock components during the course of this study. The design of the ac circuit for directly measuring the energy distribution curves was basically that of Eden (1970) who has treated it in great detail. This circuit represents a substantial improvement over the technique of computer differentiation of the current vs. retarding voltage curves (Vehse, 1968) or the earlier ac measurement techniques (Berglund and Spicer, 1964b).

The basic principles of the ac measuring technique can be understood by referring to Figure 18. The top curve shows a hypothetical current vs. retarding potential curve. Superimposed on the retarding potential, V_R is a small ac signal V_{ac}. This ac component causes a corresponding ac component in the current, I, which is proportional to the slope of the current vs.

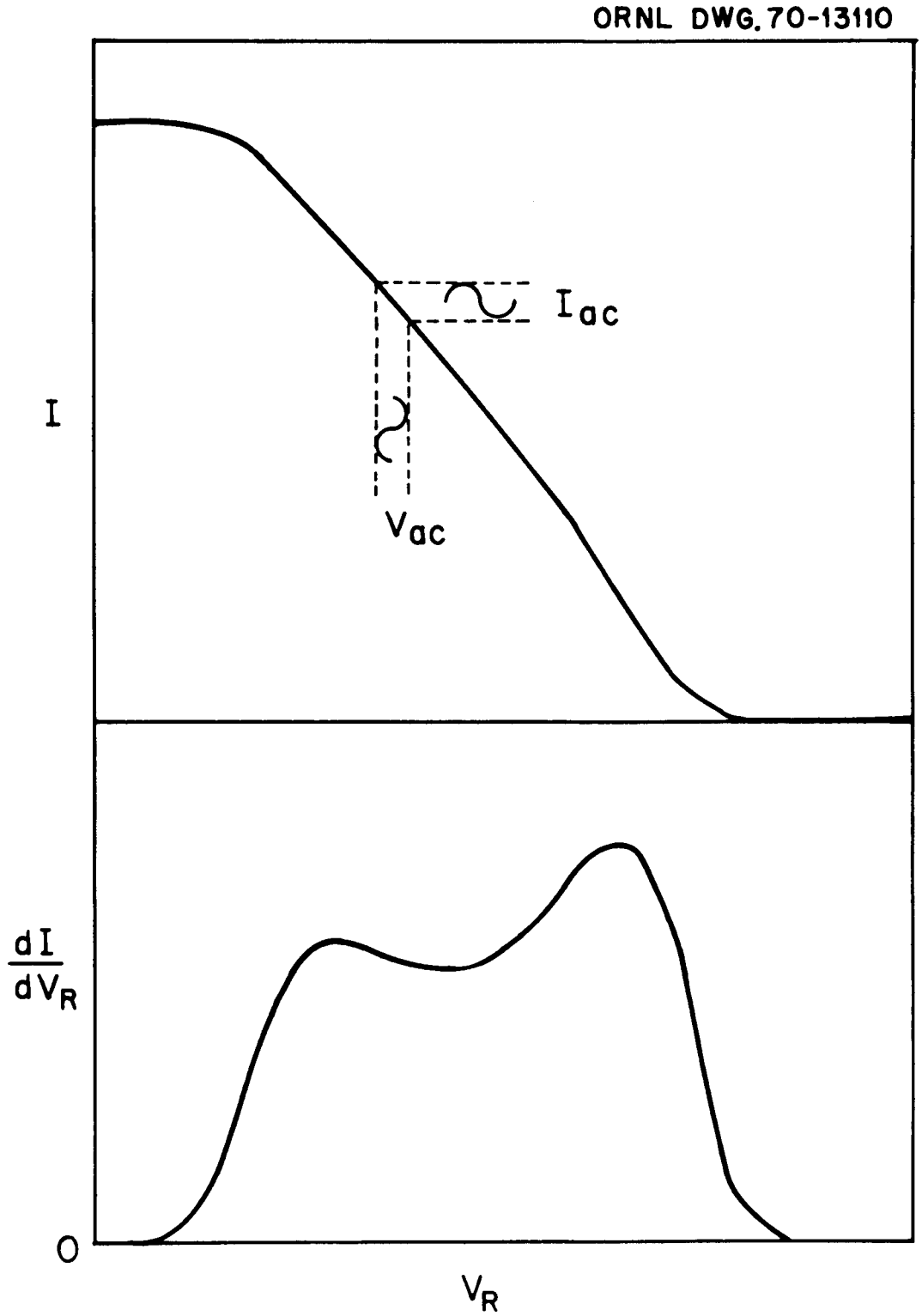

Figure 18. Illustration of ac differentiation.

retarding voltage curve. This slope is just the desired derivative or energy distribution curve, which appears in the lower curve. Thus measuring the ac component of the photoelectric current as a function of retarding voltage gives the energy distribution curve directly.

The measurements of the ac component of the photo current has two major problems associated with it. The first is that in addition to the ac component of the photo current, there is an out of phase capacitive component which must be discriminated against. The second problem is that to avoid losing resolution in the energy distribution curves, the magnitude of the ac component of the retarding voltage can be no greater than the expected energy resolution of the experiment. Consequently, the ac component of the photo current is quite small.

The circuit which solves these problems is shown in Figure 19. The heart of the system is the P.A.R. HR8 lock-in amplifier. This amplifier supplies the ac component of the retarding voltage to the retarding can via the transformer and measures the in-phase or photoelectric component after it has been amplified by the Keithly 417 picoammeter. The variable capacitor is set to equal the capacitance formed by the photoemitter and the retarding can and serves to null out most of the capacitive signal. Any capacitive signal that might remain due to slight maladjustment is rejected by the phase sensitive lock-in amplifier. The output from the lock-in amplifier was displayed on one channel of a Brown two-pen recorder. The other channel was used to display the incident or reflected light intensity or the photoelectric current.

ORNL DWG. 70-14496

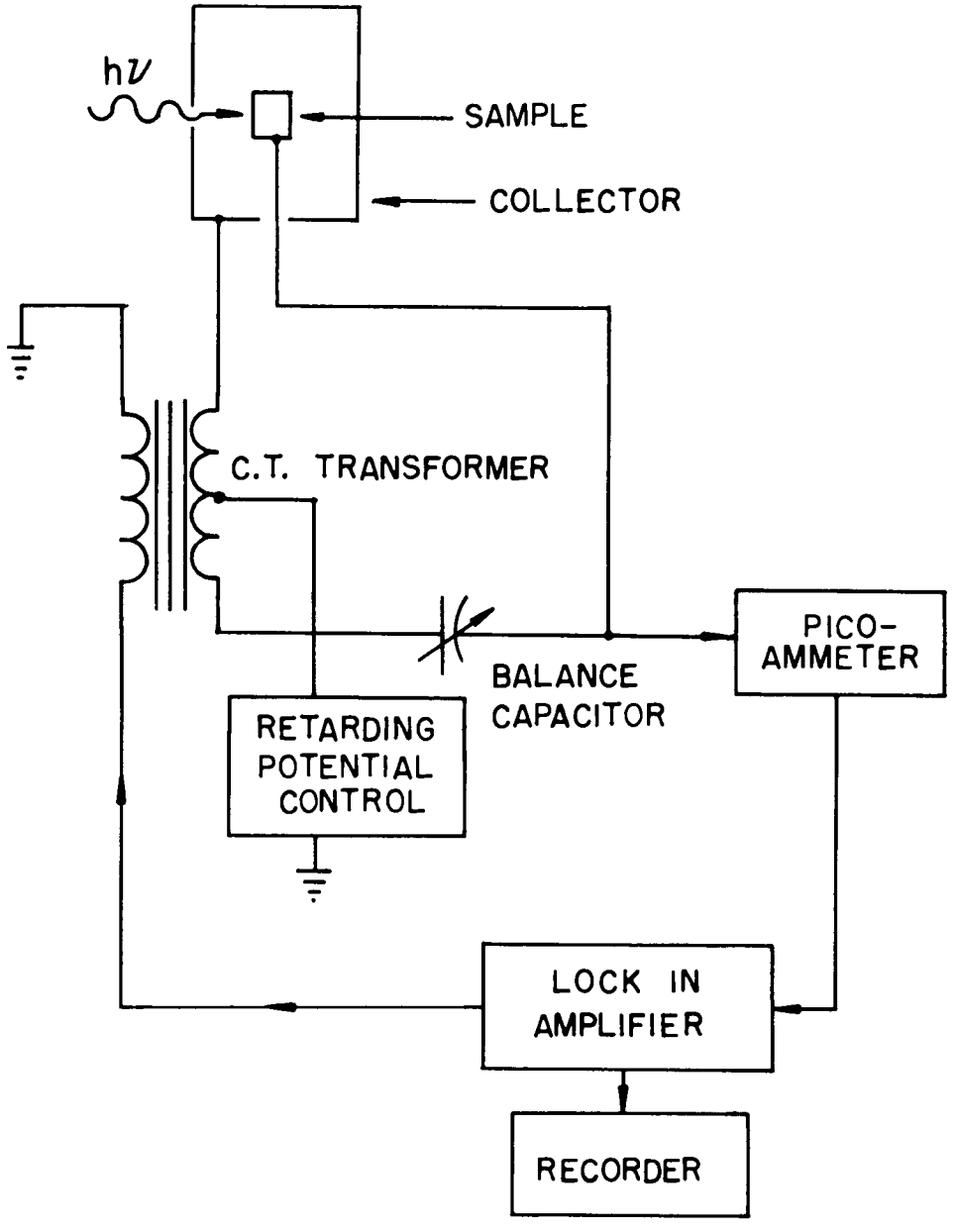

Figure 19. Circuit diagram for ac measuring circuit.

The retarding voltage control which was designed and built during this study is shown in Figure 20. This unit replaced an earlier control (Vehse, 1968) which utilized a potentiometer driven by a synchronous motor to vary the retarding voltage. The new retarding voltage control was essentially an integrating circuit which produced a linearly changing retarding potential by integrating a constant voltage. The design permitted instantaneous selection of three preset starting voltages and three pre-calibrated scanning speeds. With the 5.6 volt mercury battery switched in, the retarding voltage control was capable of producing voltages from -18 V to +6 V. The retarding voltage was measured with a non-linear systems model 481 digital voltmeter. Currents from the photomultiplier tubes were measured directly with conventional picoammeters.

VIII. ADDITIONAL EQUIPMENT

Additional equipment that was used occasionally in this study included a conventional bell jar evaporator, a Veeco Model MS-9 leak detector, a Wang 700 programmable calculator, and the ORNL-IBM System 360 Computer.

ORNL DWG. 70-14497

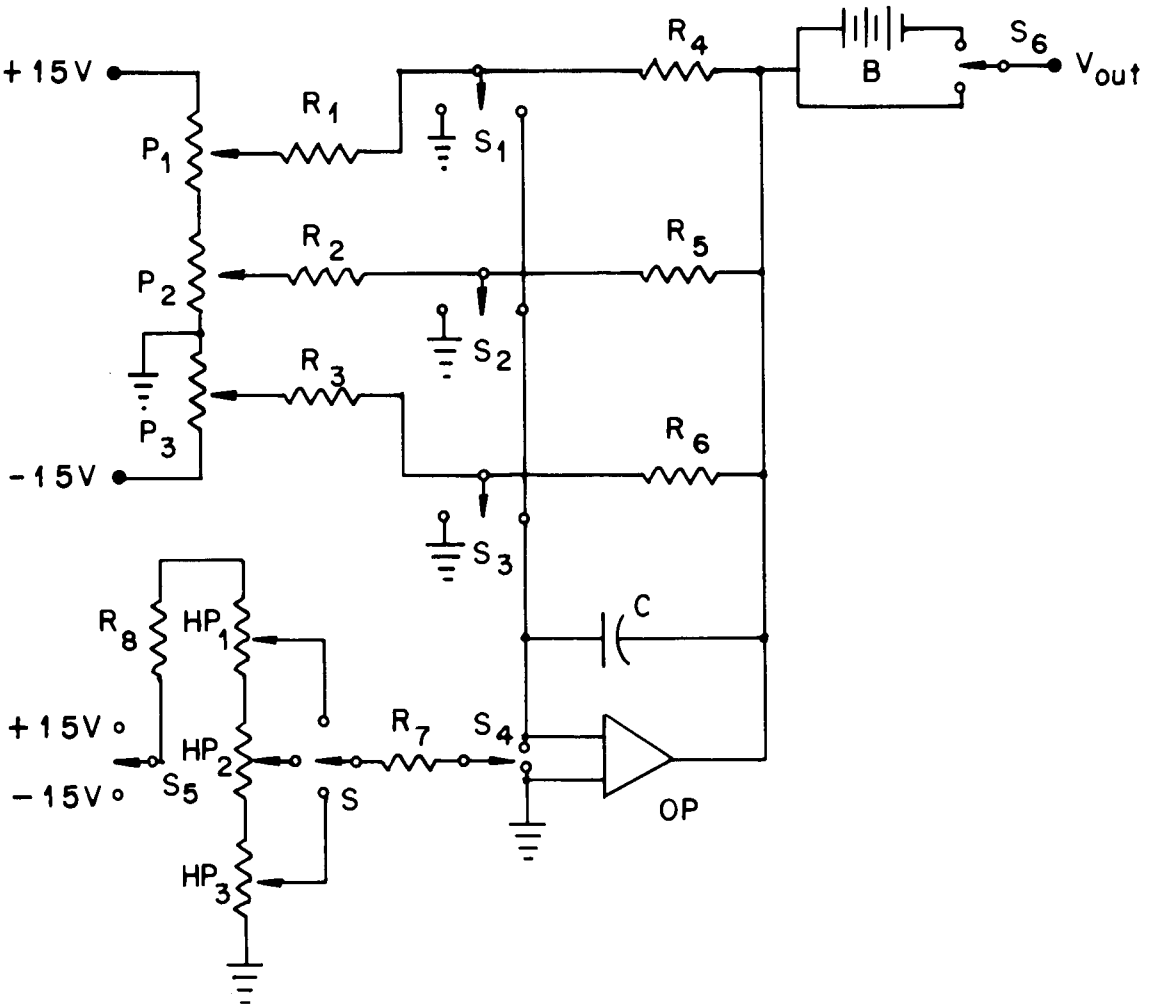

OP	PHILBRICK P2A OP. AMP.	S_1-S_3	PUSHBUTTON
R_1-R_6	120 KΩ	S_4-S_6	SPDT TOGGLE
R_7	10 MEG Ω	S_7	ROTARY
R_8	27KΩ	C	1 μfd POLYSTYRENE
P_1-P_3	10KΩ 1 TURN POTS	B	5.6V MERCURY CELL
HP_1	1KΩ 10 TURN HELIPOT		
HP_2-HP_3	500Ω 10 TURN HELIPOT		

Figure 20. Circuit diagram for retarding voltage control.

CHAPTER IV

EXPERIMENTAL PROCEDURES

I. GENERAL CONSIDERATIONS

The basic measurements performed during the course of this study can be conveniently grouped into five categories. They are (1) the measurement of the reflectance of a sample, (2) simultaneous measurement of the reflectance and absolute yield of a sample, (3) measurement of the photoelectron energy distributions of a sample, (4) measurement of the relative yield of a thin ($\sim$ 200 Å) sample as a function of photon energy for several angles of incidence, and (5) measurement of the relative yield of a thick ($\sim$ 1000 Å) sample as a function of angle for a single photon energy. The preliminary preparations were common to all five categories of measurement and are discussed in this section. In the next section, the procedures followed up to and including vacuum evaporation of each sample are discussed and in subsequent sections, the different categories of measurements are treated separately.

At the beginning of this study, the experimental chamber was baked at 200°C for several days. This procedure was repeated twice more during the course of the study when satisfactory pressures could not be reached with 24 hours of pumping.

Following the initial bake out the sample was aligned optically with the beam from the monochromator. The procedure was described by Vehse and Arakawa (1968). The result of the optical alignment was that (1) the incident and reflected beam described a horizontal plane for all angles of rotation of the sample and (2) the center of the front surface of the sample was in the center of the beam for all angles of rotation. The first condition insured that the reflected beam would strike the same spot on the light pipe as the sample and light pipe were rotated and the second condition insured that reliable measurements could be taken at the largest possible angles.

The electronic equipment for measuring the energy distributions (Figure 19, page 79) was adjusted after fabrication and installation. Only minor adjustments were needed after this initial procedure. To make the adjustment, the following steps were performed.

1. The chamber was prepared for photoemission and an oxidized sample was placed in the sample holder. The chamber was evacuated and the light source started. The picoammeter measuring the photoelectric current was placed on the appropriate scale and the retarding voltage control was set to minus one volt.

2. With the light from the monochromator blocked by the flap valve in the exit arm of the monochromator, the capacitive bridge formed by the sample and collector and by the balance capacitor (Figure 19, page 79) was deliberately unbalanced.

3. The operating frequency of the lock-in amplifier was set at a trial value.

4. The damping control on the picoammeter was set at a trial value.

5. The phase control of the lock-in amplifier was tuned to give a maximum signal.

6. The balance capacitor was tuned to give a minimum signal.

7. The phase control on the lock-in amplifier was advanced 90°.

8. The flap valve was alternately opened and closed while the phase control was adjusted for the maximum signal due to the photoelectrons.

9. The maximum signal and its attendant noise were recorded on the strip chart recorder.

10. Steps 2 through 9 were repeated with different trial values for the lock-in amplifier phase and the picoammeter damping until the maximum signal-to-noise ratio was obtained.

The best signal-to-noise ratios were achieved for lock-in amplifier frequencies of 13-17 Hz. The damping control on the picoammeter was not calibrated but a setting of about 30% of the maximum was found to be satisfactory. The picoammeter current ranges used were 3×10^{-12} through 3×10^{-10} amperes full scale. No attempt was made to calibrate the lock-in amplifier signal to the absolute value of the energy distribution curves. This was done later by normalizing the energy distribution curves to the total yield.

The operating conditions for the vacuum ultraviolet monochromator were chosen to suit the nature of the measurement. When the maximum intensity was required, the slits were opened until the gas load from the light source reached the pumping capacity of the system. If, on the other hand, better resolution was required at the expense of maximum intensity, narrower slit openings were used. The theoretical geometrical resolution (full width at half maximum) of the monochromator with the 600 lines per mm grating was 25 Å per mm of slit width. Usually slit widths of .1 to .5 mm were employed but occasionally slit widths of 1 mm were used.

Following the method of Vehse and Arakawa (1968) the monochromator background (scattered light) levels were measured by observing the photomultiplier signals with the monochromator set at a wavelength well below that produced by the source and well away from central image. The wavelength settings at which the backgrounds were taken were ~800 Å for the H_2 continuous discharge mode and ~350 Å for the interrupted discharge mode. Any errors introduced by this method of determining background were small because the intensity of the radiation was typically 10 to 50 times background level.

II. PRELIMINARY PREPARATIONS

The procedures followed before making each set of measurements are described in this section. After letting the chamber up to atmospheric pressure with argon, the retarding potential can and sample holder were

carefully cleaned with fine steel wool. The steel wool fragments were removed and the retarding potential can and sample holder cleaned with lint-free cloth soaked with acetone. This cleaning procedure was found to be necessary to preserve good electron energy resolution. The electrical insulators inside the chamber were also cleaned because accumulated metal from several evaporations could short out the retarding potential can.

The metal to be studied was loaded into a helical tungsten filament. Aluminum was loaded by wrapping about six inches of .020" diameter 99.99% pure aluminum wire around the filament. Magnesium, because it sublimes when heated in a vacuum, was loaded inside the helical filament. Two or three strands of .030" diameter 99.9% pure metal, each equal in length to the length of the filament comprised the charge. The utmost care was used in loading the filament to insure that no contamination was transferred to the filament or the sample materials.

Changes in the window, if necessary, were made at this time. New thin metallic film windows were mounted or if crystalline windows were to be used, they were cleaned. It was found that vigorous cleaning with cotton swabs soaked with 100 proof ethyl alcohol restored the transmission of a dirty lithium fluoride window to almost that of a freshly cleaved window (see Figure 16, page 71). The thin metallic film windows could not be cleaned so they were replaced when their transmission was no longer acceptable.

When all the other preparations were complete, the substrate was prepared and loaded into the chamber. The normal substrates used were 1" by 3" microscope slides (gold seal micro slides, Clay Adams, Inc.). For some measurements a "super-smooth" quartz substrate supplied by J. L. Stanford (Michelson Laboratory, China Lake, California) was used. The microscope slides were used only once; the "super-smooth" quartz substrate was reused. Old metallic samples were removed from the "super-smooth" substrate by dipping it into chromic acid cleaning solution or concentrated sodium hydroxide solution.

The cleaning procedure followed for the substrates was similar to that of Vehse and Arakawa (1968). One difference was that substrates were cleaned just prior to loading into the experimental chamber. Attempts to clean several substrates at the same time and store them for future use were thwarted; substrates that had been stored for as few as 24 hours in an evacuated dessicator would not produce uniformly shiny magnesium samples.

The substrate, held in stainless steel forceps, was washed in detergent and water and rinsed for $\sim$ 15 minutes in flowing distilled water. The substrate was then soaked in chromic acid for $\sim$ 5 minutes, rinsed for $\sim$ 15 minutes and transferred wet into an isopropyl alcohol vapor degreaser (Holland, 1964) where it remained for several minutes. The substrate was removed from the degreaser and the lower 3/4" coated with silver conducting paste (DuPont, silver preparation # 4817). When the silver paste was dry, the substrate was placed directly into the experimental

chamber. Use of this procedure insured that the substrates were uniformly free of dust and oil.

When the substrate had been placed in the sample holder, the viton O-ring sealed flange containing the vacuum evaporation equipment was secured with a few bolts. The aperture plate in the window assembly was adjusted so that the open aperture was aligned with the optical axis. The roughing pump was started. When the pressure was below .05 Torr, the diffusion pump was started. After $\sim$ 15 minutes, the ionization gauge was turned on. When the pressure fell below 1×10^{-5} Torr, the liquid nitrogen trap nearest the diffusion pump was filled. This trap was kept full by an automatic filling mechanism until the system was to be opened. The main purpose of this trap was to prevent oil vapor from the diffusion pump from reaching the experimental chamber.

Following overnight pumpdown, the pressure was again measured with the ionization gauge. If the pressure was in the mid 10^{-8} Torr range, the elbow trap connecting the diffusion pump to the experimental chamber and the combination electron collector-cold trap surrounding the substrate were filled with liquid nitrogen. This brought the pressure down to $6\text{-}8 \times 10^{-9}$ Torr. The substrate was almost completely surrounded by a surface at near liquid nitrogen temperature so the pressure in the immediate vicinity of the substrate was certainly below that measured outside the surrounded volume. No pressure measurements were attempted in the

volume surrounded by the cold trap, however, so no quantitative pressure values can be given.

While the cold traps were being filled, the electronics and the light source were turned on and allowed to stabilize. If a single spectral line was to be used, it was selected and maximized by adjusting the monochromator and the gas pressure in the light source. If wavelength scans were to be made, a compromise value for the light source pressure was selected. The entrance and exit slits were usually adjusted to .5 mm. Larger slit openings caused an unacceptable gas load in the pumps.

The filament and its charge of sample metal were outgassed. Two outgassing techniques were used. The first consisted of warming the filament to 200-300°C and allowing it to remain heated during the overnight pumpdown. The second method was to heat the filament to a temperature close to the evaporation temperature of the metal for $\sim$20 minutes just prior to evaporation of the sample. The all night outgassing method gave the best samples (the quality of samples is discussed in Chapter V) but occasionally the filament current would inexplicably rise and evaporate the entire charge during the night.

Generally, the all night method was used for magnesium and the short time, high temperature method was used for aluminum. The short time method was considered satisfactory for aluminum because it could be outgassed in the molten state whereas magnesium, because it sublimes

(Holland, 1956), had to be outgassed in the solid state. Presumably gasses would be liberated from a molten metal faster than from a solid metal.

When all else was in readiness, the final preparations were made. The light pipe was rotated so that its sodium salicylate covered face was behind the cold trap. The substrate was rotated so that it faced the filament. The ionization gauge was turned off and covered. Occasionally the ionization gauge was left on during evaporation to monitor the pressure surge. During evaporation, the pressure usually rose momentarily to the high 10^{-7} range and then rapidly subsided to the pressure recorded prior to evaporation. The reason for turning off and covering the gauge prior to evaporation was to minimize the time between evaporation and the first measurement. To evaporate the sample, the filament containing the sample metal was brought quickly up to temperature while the quartz crystal thickness monitor was observed. The desired thickness of sample metal was usually evaporated in ~ 10 seconds. Short evaporation times insured that a minimum of residual gas was incorporated into the evaporated sample. No chemical analyses of the evaporated samples were made during the course of this study because Vehse and Arakawa (1968) demonstrated that the purity of the sample metal is preserved upon vacuum evaporation in the experimental chamber. Following the vacuum evaporation, the sample was rotated so that the freshly evaporated surface faced the light beam, and measurements were begun immediately. The various types of measurements are described in the following sections.

III. MEASUREMENT OF REFLECTION

The preliminary procedures of Section II, this chapter, were followed except that no conducting paste was applied to the substrate. Following vacuum evaporation of the sample, the sample holder was rotated to the desired angle of incidence. The light pipe was then rotated to give a maximum signal. The monochromator was scanned over the chosen spectral region while the photomultiplier current due to the reflected beam and the photomultiplier current due to the monitor were recorded simultaneously on the two-pen recorder. The scanning speed was always chosen to be compatible with the response time of the measuring circuit. For sharply peaked line sources, scanning speeds as low as 50 Å/min were used, while for slowly varying continuum sources, scanning speeds of 200 Å/min were found to be satisfactory.

After the chosen portion of the spectrum was scanned, the sample was withdrawn from the beam, and the light pipe was rotated so that the incident beam struck its face. The same portion of the spectrum was again scanned at the same speed while recording the signals due to the incident beam and the beam monitor. The reflectance of the sample, R was then given by

$$R = \left(\frac{I_R - I_R^B}{M_R - M_R^B} \right) \Bigg/ \left(\frac{I_o - I_o^B}{M_o - M_o^B} \right) \tag{69}$$

In this equation, I_R is the photomultiplier signal due to the reflected beam, I_o is the photomultiplier signal due to the incident beam. The quantities M_R and M_o are the monitor signals associated with the reflected and incident beams. A variable with a superscript B refers to the background or scattered light component of the beam. The measurement of background or scattered light levels is described in Section I of this chapter. In practice, Equation 69 was seldom needed exactly as written because the light source was sufficiently stable that M_R was equal to M_o. In this case the reflectance was given simply by

$$R = \left(I_R - I_R^B \right) \Big/ \left(I_o - I_o^B \right) \tag{70}$$

where the symbols have their previous meanings.

IV. SIMULTANEOUS MEASUREMENT OF REFLECTANCE AND ABSOLUTE YIELD

The reflectance of a photoemissive substance is an extremely important parameter in the analysis of the absolute yield. For this reason, the light pipe and electron collector were designed to permit simultaneous measurement of the yield and reflectance of the same sample.

The preliminary steps described in Section II of this chapter were followed. In addition it was necessary to apply fresh sodium salicylate to the light pipe just prior to pumpdown and to calibrate the monitor at one

wavelength. The monitor was calibrated at 1216 Å (H_2 Lyman alpha line) by comparing the monitor signal with the signal from a factory-calibrated lithium fluoride window photomultiplier tube temporarily mounted on the exit arm of the monochromator. The tube used was an EMR model 541F-08-03900 and was ~2 months old when used for calibration purposes.

Prior to evaporating the film, the selected portion of the spectrum was scanned while the beam was allowed to fall upon the freshly sensitized light pipe. The signals from the light pipe and monitor photomultipliers were recorded. Following evaporation, the sample was positioned so that the angle of incidence was 10°, and the light pipe was rotated into position and adjusted for maximum signal. The selected portion of the spectrum was again scanned while simultaneously recording the photoelectric, reflected light and monitor signals. A second single channel recorder was used in addition to the normal two channel recorder for this measurement. The sample was withdrawn from the beam and the light pipe rotated to face the beam directly. The same portion of the spectrum was again scanned while recording the signals from the light pipe and the monitor. The procedure was then repeated as many times as desired.

The reflectance was calculated from the data using either Equation 69 or Equation 70 of Section III, this chapter. The absolute yield was calculated by first calculating the yield relative to the light pipe signal and then linearly scaling the relative yield so that it matched the absolute yield at 1216 Å. The relative yield obtained in this way is accurate

to the extent that sodium salicylate has a flat spectral response in the region covered (Samson, 1967). The accuracy of the absolute yield is dependent upon the accuracy of the calibration of the photomultiplier used to calibrate the beam monitor. According to Samson (1967), the spectral response of sodium salicylate is uniform to within 20% in the spectral region from 850 to 2000 Å. Assessment of the error in the absolute yield was more difficult because no error figures were available from the manufacturer. In addition, the transmission of the window of the photomultiplier as well as the response of the photomultiplier can change in time. Fortunately, a fairly large error in the absolute yield does not seriously affect the conclusions drawn in Chapter V.

V. MEASUREMENT OF PHOTOELECTRON ENERGY DISTRIBUTION CURVES

The preliminary steps outlined in Section III were followed. In addition, the ac measuring circuit was checked for adjustment. The two-pen recorder was arranged so that the photoelectron energy distribution was traced on the first channel while the monitor current or the photoelectric current was traced on the second channel. A toggle switch permitted selection of either the photoelectric current or the monitor signal. Finally, the retarding voltage control was set to a positive collecting voltage.

Following evaporation, the sample was turned to face the beam normally. The photoelectric current was checked and the appropriate pico-ammeter scale was chosen. The retarding voltage control was set to a voltage sufficiently negative to retard all the electrons. The voltage scan was then started. The scanning speed was 4 volts/minute. After the scan was started, the second channel of the two-channel recorder was switched to the monitor signal for a few seconds and then switched back to record the photoelectric current. After the entire energy distribution had been traced, the second channel was again switched to the monitor. Thus a permanent record of the monitor signal, the photoelectric current vs. voltage and the photoelectron energy distribution was made. If a somewhat unstable light source had to be used, the second channel of the recorder was used to monitor the light during the entire tracing of the energy distribution.

VI. RELATIVE YIELD OF A THIN SAMPLE

Relative yield measurements on thin (~ 200 Å) samples of magnesium were made as a function of photon energy for several angles of incidence. From the data, the plasmon energy and the thickness of the film could be determined.

The preliminary steps described in Section II, this chapter, were followed. Following evaporation of the sample, it was rotated normally to the beam and the desired portion of the spectrum was scanned. The photoelectron current was recorded on one channel of the two-pen recorder

and the monitor signal was recorded on the other channel. The measurement was repeated for angles of incidence of 10, 20, 30, and 40 degrees. The data was tabulated as

$$Y(h\nu, \theta)/Y(h\nu, 0) \tag{71}$$

and plotted as a function of wavelength. In this expression, $Y(h\nu, \theta)$ is the photoelectric current at photon energy $h\nu$ and at angle of incidence θ.

Several attempts were made to measure the relative yield for thinner (50-100 Å) films of magnesium, but a great deal of difficulty was experienced in obtaining a good conducting film. After the conclusion of the experiments, it was learned that prior deposition of a fraction of a monolayer of silver leads to continuous conducting magnesium films as thin as 50 Å (Feuerbacher, 1970). Apparently, the silver atoms act as nucleation sites for the magnesium.

VII. RELATIVE YIELD OF A THICK SAMPLE

The relative photoelectric yields of thick (~ 1000 Å) films as a function of angle for a single photon energy were used to determine an average attenuation length for photoelectrons excited in aluminum by the 584 Å He resonance line.

In general, the preliminary preparations of Section II, this chapter, were followed. A self supporting tin film about 1000 Å thick was used as a window and as a band pass filter. The grating was replaced with a gold mirror

which reflected the light from the He discharge onto the band pass filter-window. The filter passed $\sim 20\%$ of the 584 Å He resonance line and rejected the rest of the light from the He discharge. An additional feature of this arrangement was that the polarization of the light could be calculated from Fresnel's equations.

The retarding voltage control was set to + 8 V to collect all the electrons. Immediately following evaporation, the sample was rotated normally to the beam and the strip chart recorder started. Every few seconds the sample was rotated 2°. Every 20° or so, the sample was rotated back to normal incidence and the photoelectron current at 0° remeasured. The measurements were continued to an angle of 74°. Beyond 74° the beam width was wider than the width of the sample presented to it and measurements would have been meaningless. The measurements were repeated as many times as desired. The data were tabulated as $Y(\theta)/Y(0)$ where $Y(\theta)$ is the photoelectric current at an angle of incidence θ and $Y(0)$ is the normal incidence photoelectric current.

CHAPTER V

RESULTS AND DISCUSSION

I. INTRODUCTION

This chapter gives the experimental results of the study together with their interpretation.

Section II describes the effects of aging of magnesium films evaporated in a vacuum of 3×10^{-8} upon the photoelectric yield, work function, and energy distributions. These results precipitated the decision to build the combination cold trap-electron collector which improved the sample storage life and energy resolution.

Section III gives the reflectance, yield, and energy distribution measurements for magnesium taken in the improved apparatus. The reflectance is analyzed in terms of the nearly-free-electron model, photon scattering, and non-radiative surface plasmon absorption. The energy distributions are shown to be compatible with the density of states obtained from theory and other experimental methods. Evidence is presented to show that a peak in the photoelectric yield is due to surface plasmon-one electron transitions.

Section IV gives an analysis of the yield and energy distributions of magnesium and aluminum in terms of the attenuation length for photoelectrons. Aluminum yield data taken as a function of angle are presented and analyzed

for the electron attenuation length. The experimental attenuation lengths are compared with the theoretical and experimental results of other investigators.

Section V gives the results of the determination of the plasmon energy of magnesium by photoelectric means.

II. TEMPORAL EFFECTS

Photoelectric measurements were originally carried out at $\sim 3 \times 10^{-8}$ Torr in the apparatus described by Vehse and Arakawa (1968). Rapid changes in the photoelectric yield and photoelectric energy distributions prompted an investigation of the causes of these changes. The measurements were made in accord with the descriptions in Chapters II and III except that a seven-inch diameter stainless steel grid was used in place of the combination cold trap-electron collector.

The general results of the temporal photoelectron energy distribution measurements are summarized in Figures 21 and 22 which show distributions for 10.2 and 7.65 eV photons, respectively. The distributions have been plotted against the retarding potential since there are uncertainties about the work functions of the regarding grid and the sample. These work functions must be known to locate the distributions correctly on an energy scale. A certain amount of broadening of the distributions is introduced by the non-ideal geometry of the sample and the retarding grid and by the instrumentation. In addition, any non-uniformity of the work function over the surface of the sample or the collector will lead to broadening. For a metal, the maximum

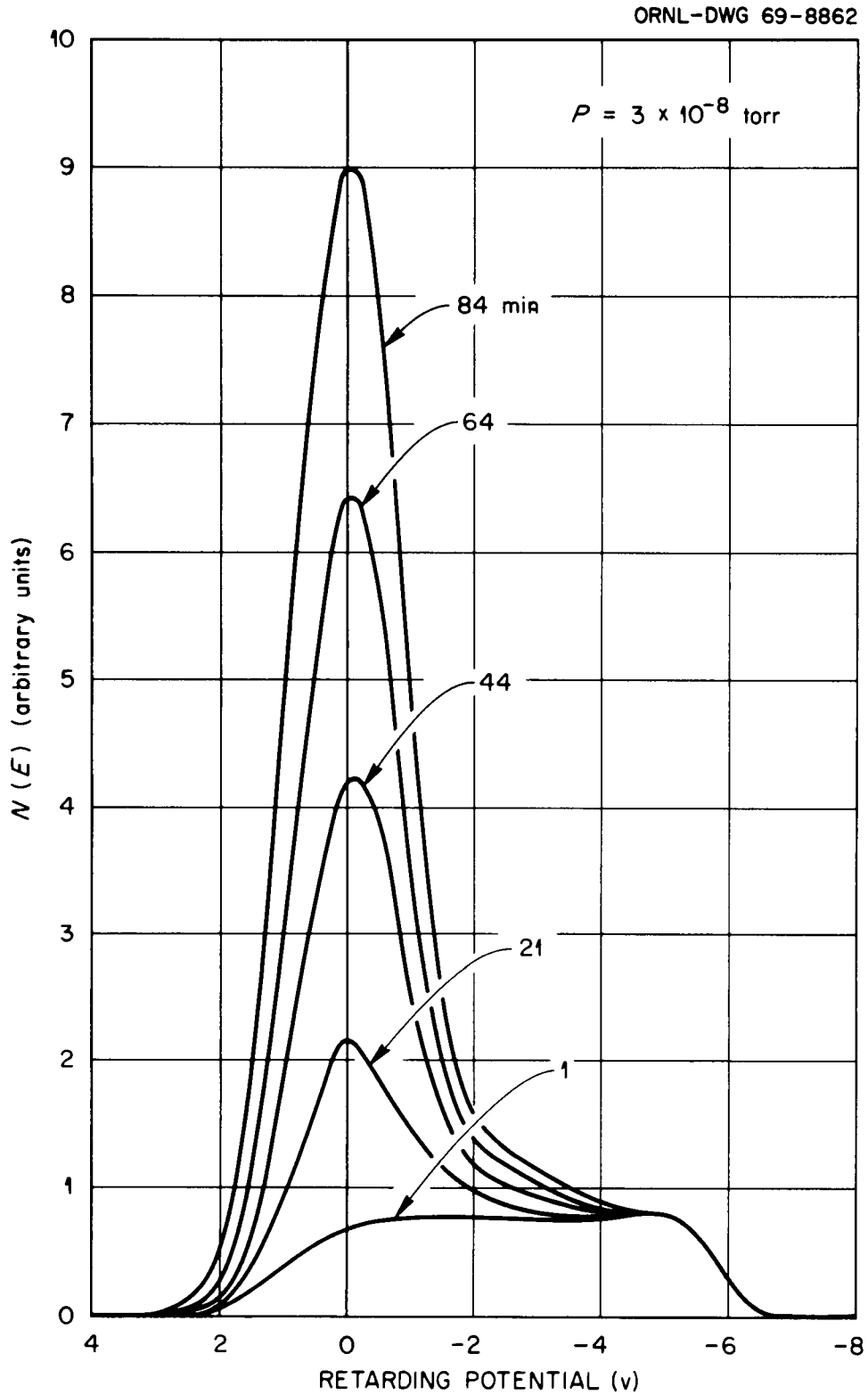

Figure 21. Photoelectron energy distributions as a function of time for magnesium (10.2 eV).

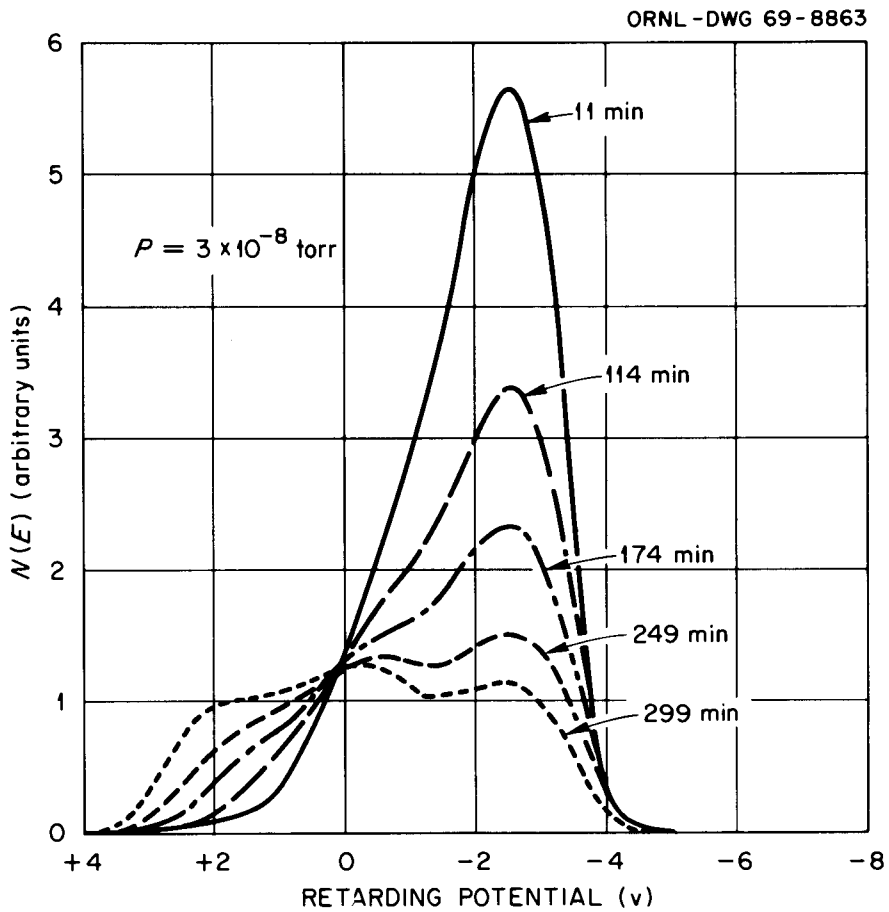

Figure 22. Photoelectron energy distributions as a function of time for magnesium ($h\nu$ = 7.65 eV).

width of the distribution, including inelastic scattering of electrons on emission, should be

$$\Delta = h\nu - \varphi \tag{72}$$

where $h\nu$ is the photon energy and φ is the photoelectric work function of the surface. Any deviations from this width may be attributed to the broadening effects mentioned.

Figure 21, page 100, shows the rapid growth of a low energy peak in the photoelectron energy distribution for 10.2 eV photons. Since the high energy end of the distribution does not change, the increasing in time of the low energy peak is presumed to originate from surface emission rather than electron energy loss processes. Figure 22 shows the time behavior of the energy distribution for 7.65 eV photons. Compared with the 10.2 eV curves, the changes in the photoelectron energy distributions are smaller for an equivalent time period. The behavior of the photoelectron energy distributions can be interpreted in terms of the growth of an insulating surface layer on the magnesium which has a band gap between 7.65 and 10.2 eV. Thus the 10.2 eV photons would cause photoelectron emission from the surface layer but the 7.65 eV photons would be unable to excite electrons across the band gap. In addition, the insulating surface layer would tend to cause reflection of the electrons excited in the metal by the 7.65 eV photons thus causing the decrease in the high energy portion of the distribution.

The change of the low energy edge of the distributions in Figure 22, page 101, can be explained by the behavior of the photoelectric work function of the film. Figure 23 shows the change in the photoelectric work function as a function of time-pressure. These measurements were made by observing the long wavelength limit of the photoemission as a function of time. As the work function gets lower (Figure 23) the width of the distribution (Figure 22) increases in accordance with Equation 72. The change in the work function and the shift in the photoelectron energy distributions of Figure 22 is about 1.5 eV for times of about 300 minutes.

In order to determine if residual gas was responsible for the changing surface conditions, separate runs were made in an atmosphere consisting of the normal background constituents plus a small amount (partial pressure 2×10^{-8} Torr) of N_2, H_2O, and O_2. The total yield at 10.2 eV, which was taken as a measure of the surface contamination is plotted in Figure 24. It is clear that of the gases tested, oxygen causes the largest increase in yield over time. This suggests that the formation of magnesium oxide on the surface is a principle contamination mechanism. The photoelectron energy distributions are consistent with this view since MgO has a band gap of about 8 eV (Williams and Arakawa, 1967). Contamination effects in photoemission, while interesting, are far from novel so our efforts were directed toward improving the sample environment and the resolution of the electron energy analysis. It is seen in the next section that use of the combination cold

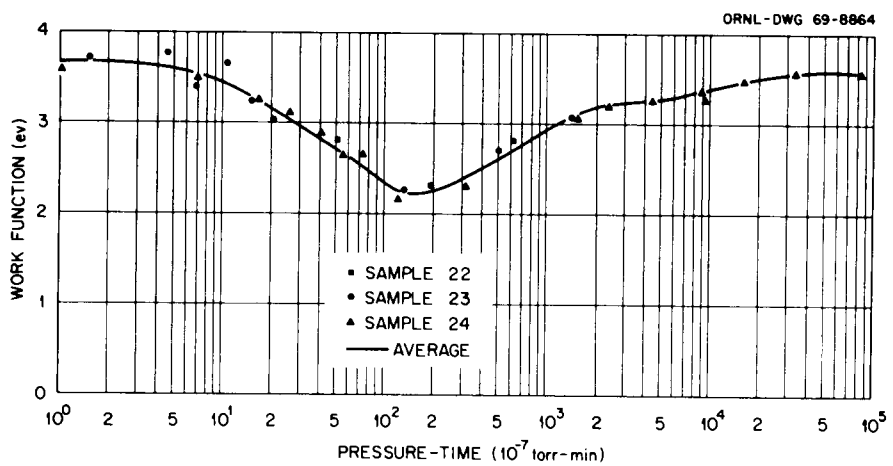

Figure 23. Photoelectric work function of evaporated magnesium films as a function of time-pressure.

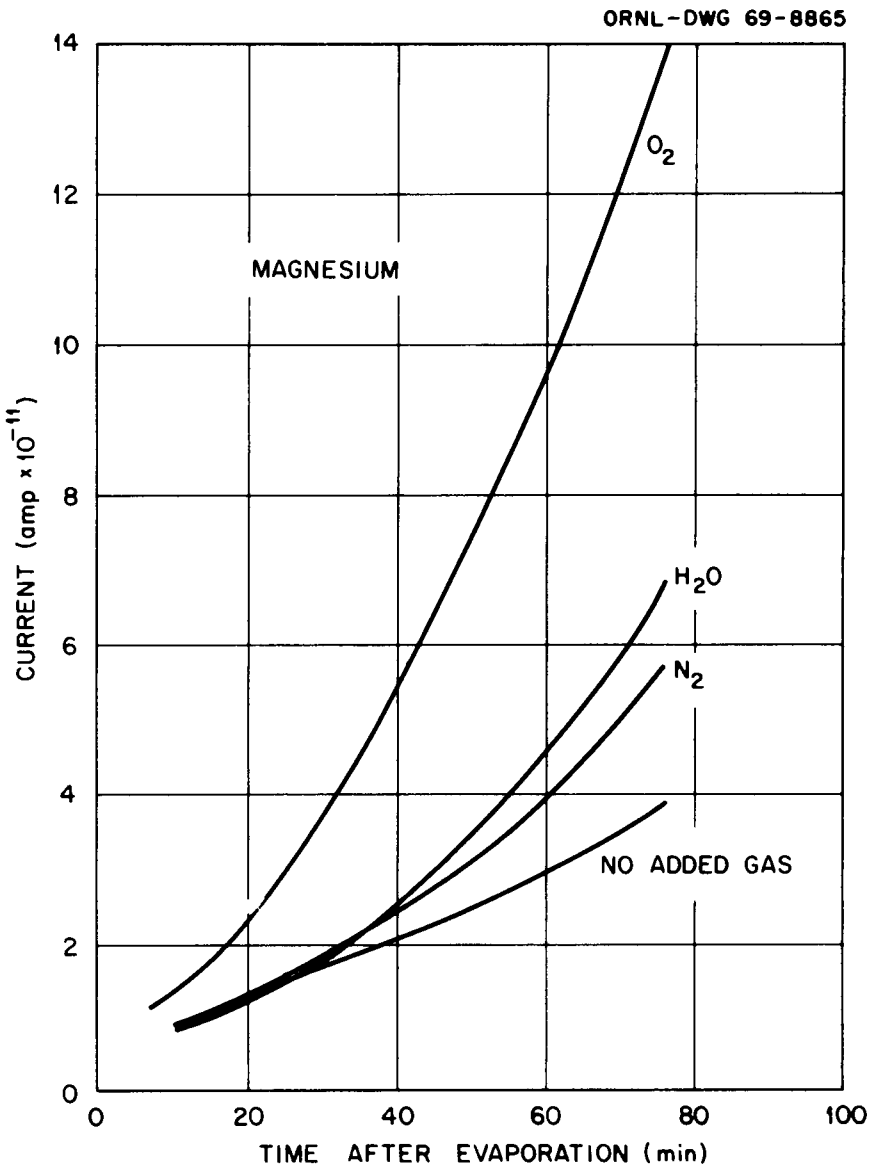

Figure 24. Total yield for magnesium at $h\nu = 10.2$ eV as a function of time for various gases admitted to the vacuum system.

The partial pressure of each added gas was 2×10^{-8} Torr.

trap-electron collector described in Chapter II gives better energy resolution and sample life than the original grid.

III. REFLECTANCE, YIELD, AND ENERGY DISTRIBUTIONS OF MAGNESIUM

Reflectance measurements in the region 2 eV $\leq h\nu \leq$ 12 eV were made on magnesium as described in Chapter III, Section III. In addition, simultaneous reflectance and yield measurements were made as described in Chapter III, Section IV. All of the measurements described in this section were taken at normal or near normal incidence on films greater than 400 Å in thickness.

The results for several of these reflectance measurements are given in Figure 25. The films designated A and B were ~500 Å thick while film C was ~ 1000 Å thick. The difference in thickness is not important except near the plasma energy (~ 10.5 eV) where magnesium becomes transparent. In this region the thinner films exhibit anomalously high reflectances due to reflection from the substrate. The dashed line represents the measurements of Daude et al. (1967). Their data were taken at 20° angle of incidence on ~2000 Å thick films. The solid line is the reflectance calculated from the Drude model. In the Drude model for a nearly free electron gas, the real (ϵ_1) and imaginary (ϵ_2) parts of the dielectric constant are given by

$$\epsilon_1 = 1 - \frac{\omega_p^2}{\omega^2 - \gamma^2}$$

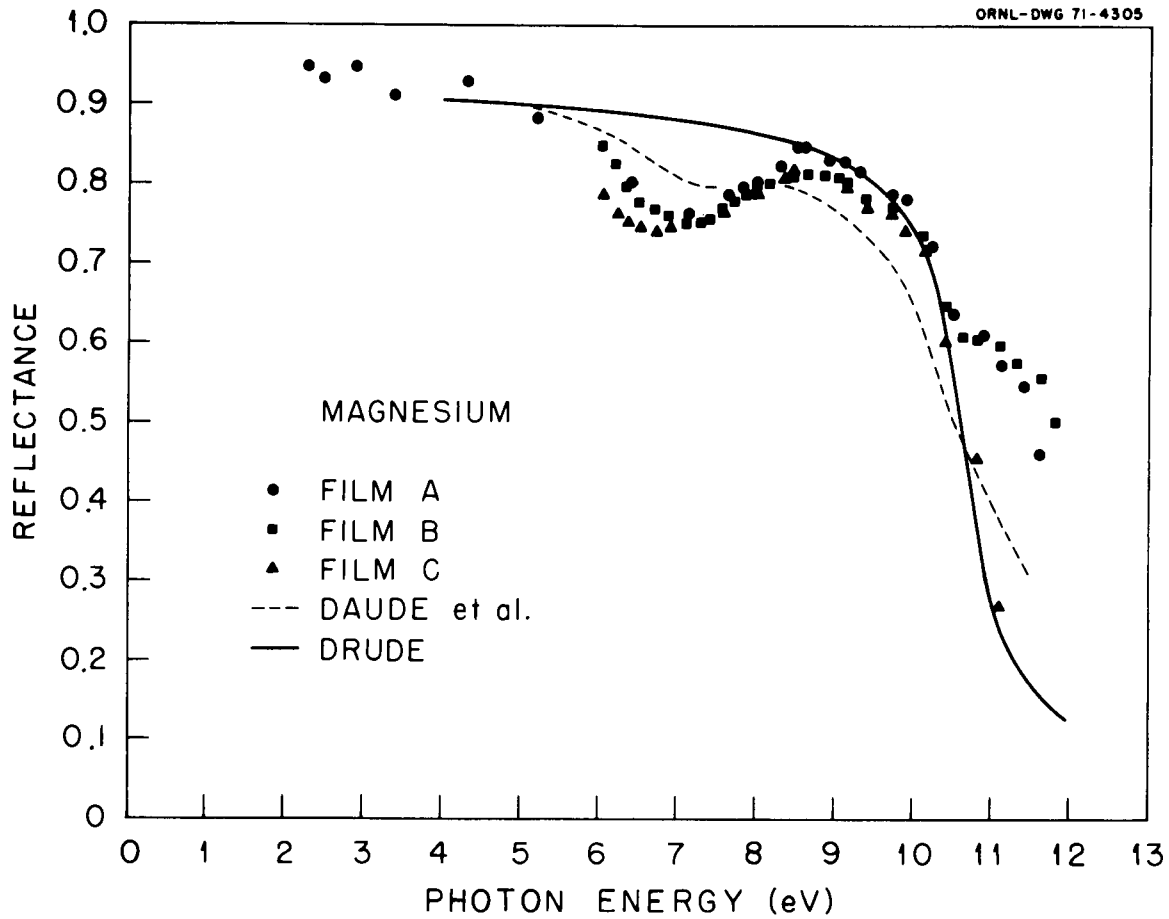

Figure 25. Near normal incidence reflectance of magnesium in the 2-12 eV range.

$$\epsilon_2 = \frac{\gamma}{\omega} \frac{\omega_p^2}{\omega^2 - \gamma^2}$$

where ω_p is the plasma frequency and γ is a damping constant. The Drude curve in Figure 25, page 105, was obtained by setting $\hbar\omega_p = 10.5$ eV and varying γ until a fit was obtained at the high and low energy portions of the curves. A value of $\hbar\gamma = .5$ eV was found to give the fit shown.

It is apparent from Figure 25, page 105, that magnesium exhibits the reflectance characteristics of a damped free electron gas except for the region from 6-8 eV. A prominent dip in the reflectivity in this region is evident in our data and in the data of Daude et al. (1967). The energy location of this dip is near that of the surface plasmon energy for magnesium ($\sim\hbar\omega_p/\sqrt{2}$; see Chapter II, Section V). Analogous dips have been observed in silver (Jasperson and Schnatterly, 1967; Stanford et al., 1968) and in aluminum (Williams et al., 1967; Feuerbacher and Steinman, 1969) and have been interpreted as absorption by non-radiative surface plasmons.

Endriz and Spicer (1971a) have analyzed the dip in the reflectivity of aluminum using the recent theory of Elson and Ritchie (1970; 1971). We have made a similar analysis of the dip in the reflectance of magnesium with the Elson and Ritchie theory which is described in Chapter II, Section V.

The analysis of the surface plasmon dip was carried out by first calculating ΔR as the difference between the Drude reflectance in Figure 25, page 105, and the set of reflectance data under examination and then fitting

the theoretical expressions for surface plasmon excitation and diffuse scatter (Equations 52 and 61). Volume damping (process 1, page 50) and $\vec{k} \rightarrow \vec{k}$ damping (process 5, page 51) were included. The commonly used Gaussian form of the autocorrelation function was used. Equations 52 and 61 were computer integrated by means of Gaussian quadrature.

The results for three films are shown in Figure 26 together with a theoretical fit made by adjusting only two parameters, the autocorrelation length, and the surface roughness. the fits obtained were reasonably good with the greatest deviation at energies above the surface plasmon energy. Lack of a perfect fit in this region is not too surprising because a quite arbitrary choice for the surface roughness spectrum was made. Inclusion of more damping would serve to broaden the theoretical curves which might then be adjusted to give a better fit. This was not done, however, because it was felt that the number of adjusted parameters should be kept to a minimum.

Several important features are evident in Figure 26. Firstly, the effect is not a small one, amounting to $\sim 15\%$ for these films. Secondly, despite careful attempts to prepare the films in a standard fashion, the shape and magnitude of ΔR as well as the theoretical parameters necessary to give a good fit vary from film to film. Thirdly, the parameters necessary to give a good fit are completely plausible. Endriz and Spicer (1971a), for example, found a surface roughness of 12 Å for aluminum deposited on a float glass substrate. Feuerbacher and Steinmann (1970) find that only roughness

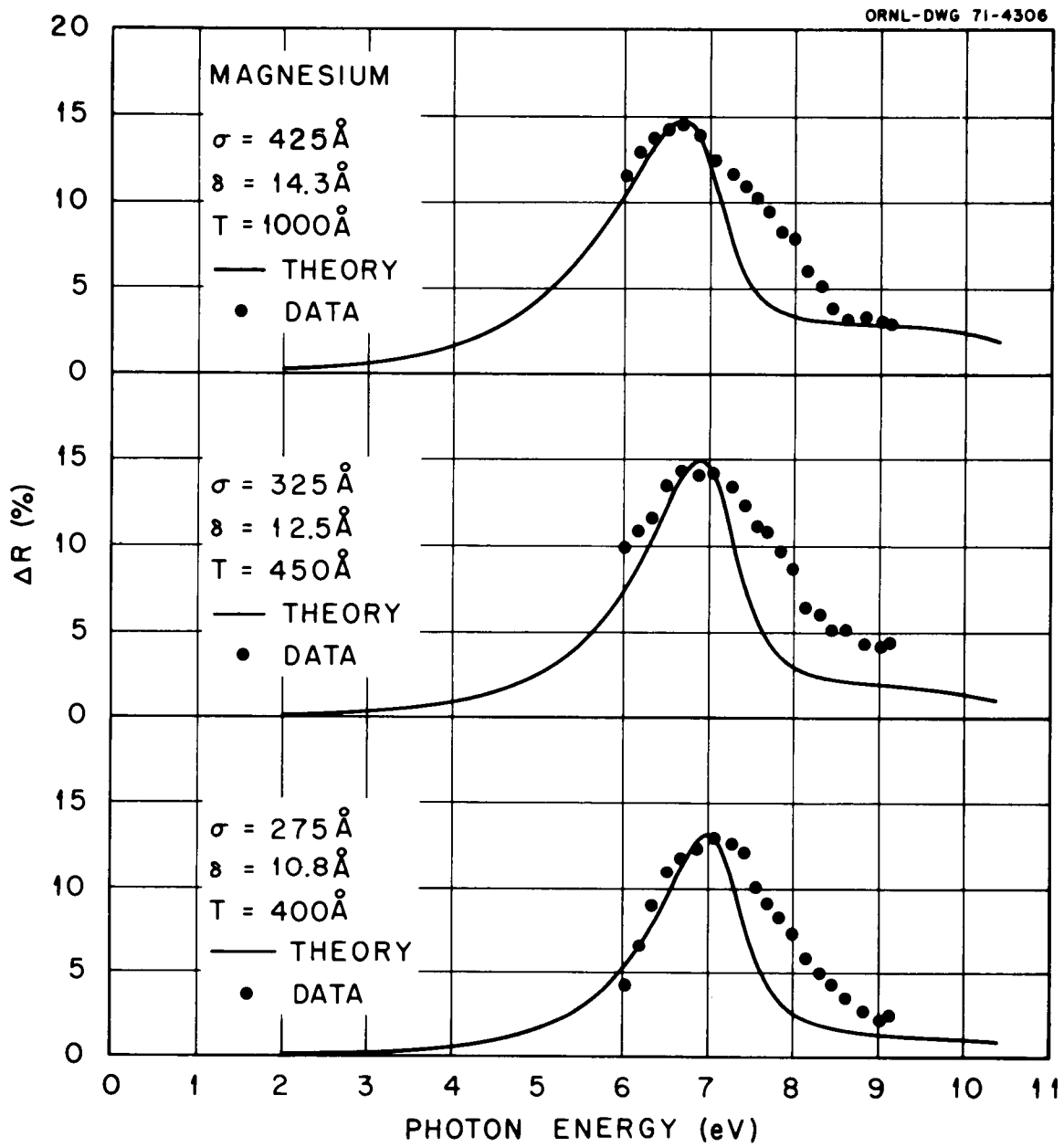

Figure 26. Experimental decrease in the reflectance of magnesium due to surface plasmon absorption for three films together with a theoretical fit to each.

components corresponding to spatial structures closer than 1000 Å contribute to the surface plasmon dip in aluminum.

There is evidence of one trend in Figure 26. As the film thickness is increased, both the rms roughness and the autocorrelation length increase. All the roughnesses shown in Figure 26 are larger than the 7-8 Å reported for the substrate (Stanford, 1970) so it is tempting to postulate that as the film thickness is increased, the roughness and the autocorrelation length increase. Although more data would be necessary to make a conclusive judgement, it is significant that Braundmeier et al. (1970) have concluded that the roughness of aluminum films increases as a function of thickness as the thickness is increased up to about 1000 Å. Their conclusions were based upon measurements of the intensity of radiation emitted by non-radiative surface plasmons.

Simultaneous measurements of the absolute yield and reflectance were made on magnesium films according to the procedures detailed in Chapter IV, Section IV.

In Section II of this chapter the effects of contamination upon the yield at 10.2 eV were presented. The measurements made in this section afforded an opportunity to observe the effects of contamination upon the yield for the range of photon energies $6 \leq h\nu \leq 12$ eV. Figure 27 shows the results of this study. The curve labeled T_o was the first measurement taken after evaporation of the film. The scan was completed in eight minutes and a second scan (T_1) was started immediately. Following this second scan the sample was deliberately exposed to the monochromator pressure by

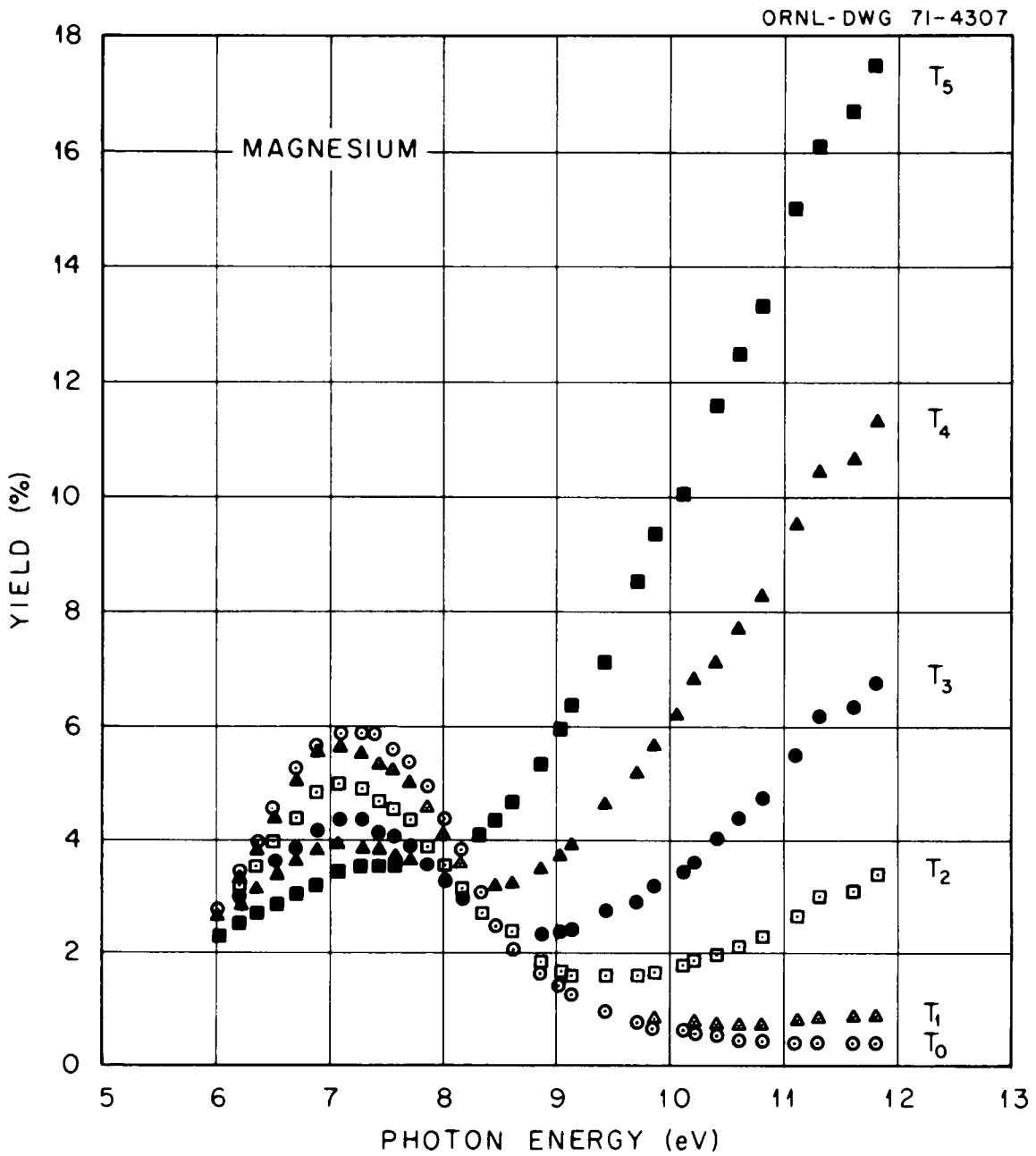

Figure 27. Photoelectric yield for magnesium as a function of photon energy and time.

opening the window for a short time and then measured again (T_2). This procedure was repeated three more times. The photoelectric current at 10.2 eV was monitored during each exposure and exposure times were chosen to give roughly equally spaced increases in the photoelectric current at 10.2 eV. Thus only the shapes of the yield curves are significant since it is not possible to correlate the yield changes with specific exposures. Quantitative results at 10.2 eV were given in Figure 24, page 105, for various gases.

The results shown in Figure 27 are entirely consistent with the contamination mechanism proposed in Section II of this chapter. For energies greater than 8.5 eV the yield increases monotonically with exposure while for energies less than 7.5 eV the yield decreases monotonically with exposure. This behavior is consistent with the growth of an insulating layer on the surface. For the higher energies, photoelectrons from the growing insulating layer serve to increase the yield while at lower energies (below the band gap of the insulator) the insulator not only has no emission but attenuates the emission of electrons from the metal. Similar behavior in aluminum has been observed by Stanford et al. (1966) in which case the transition from the yield increasing with contamination to the yield decreasing with contamination takes place at 11.5 eV. Stanford et al. (1966) interpret the decrease as being due to a shift in the surface plasmon energy from 10.5 to 7 eV as a result of Al_2O_3 buildup on the surface. It should be noted, however, that more than 20 Å of dielectric coating is required to shift the surface plasmon energy to the asymptotic value of $\omega_p/\sqrt{1+\epsilon}$ (Braundmeier et al., 1970) where ϵ is the

dielectric constant of the coating. It is generally known that it takes several hours at atmospheric pressure to build up 20 Å of oxide coating on an aluminum surface so it seems unlikely that this buildup would occur in a reasonable length of time in the reported vacuum of 3×10^{-8} Torr. Values as low as 5 Å for the attenuation length of low energy electrons in aluminum oxide have been reported (Thomas, 1965; Collins and Davies, 1963) so the direct attenuation mechanism is plausible.

The quantum yield and reflectance data for two films are presented in Figure 28. The quantum yield for a third film has been presented in Figure 27, page 112. The yield measurement in each case is the first run after evaporation. Referring to Figure 27, page 112, it is seen that the change due to contamination is so small for the first two runs that the first run can be considered representative of a clean surface. The yield is plotted in terms of electrons per incident photon.

The yield curves exhibit minor variations, but the gross shapes are consistent. Interpretation of the shape of the curves appears at first to be straightforward. The initial rise from 6 eV might be interpreted as the ordinary increase from threshold and the decrease above 7 eV might be explained by the increasing optical transparency of the magnesium plus the decrease in the electron attenuation length. When a quantitative analysis is made using Equation 19, however, this simple explanation fails to account for the magnitude of the peak centered near 7 eV. As pointed out in the

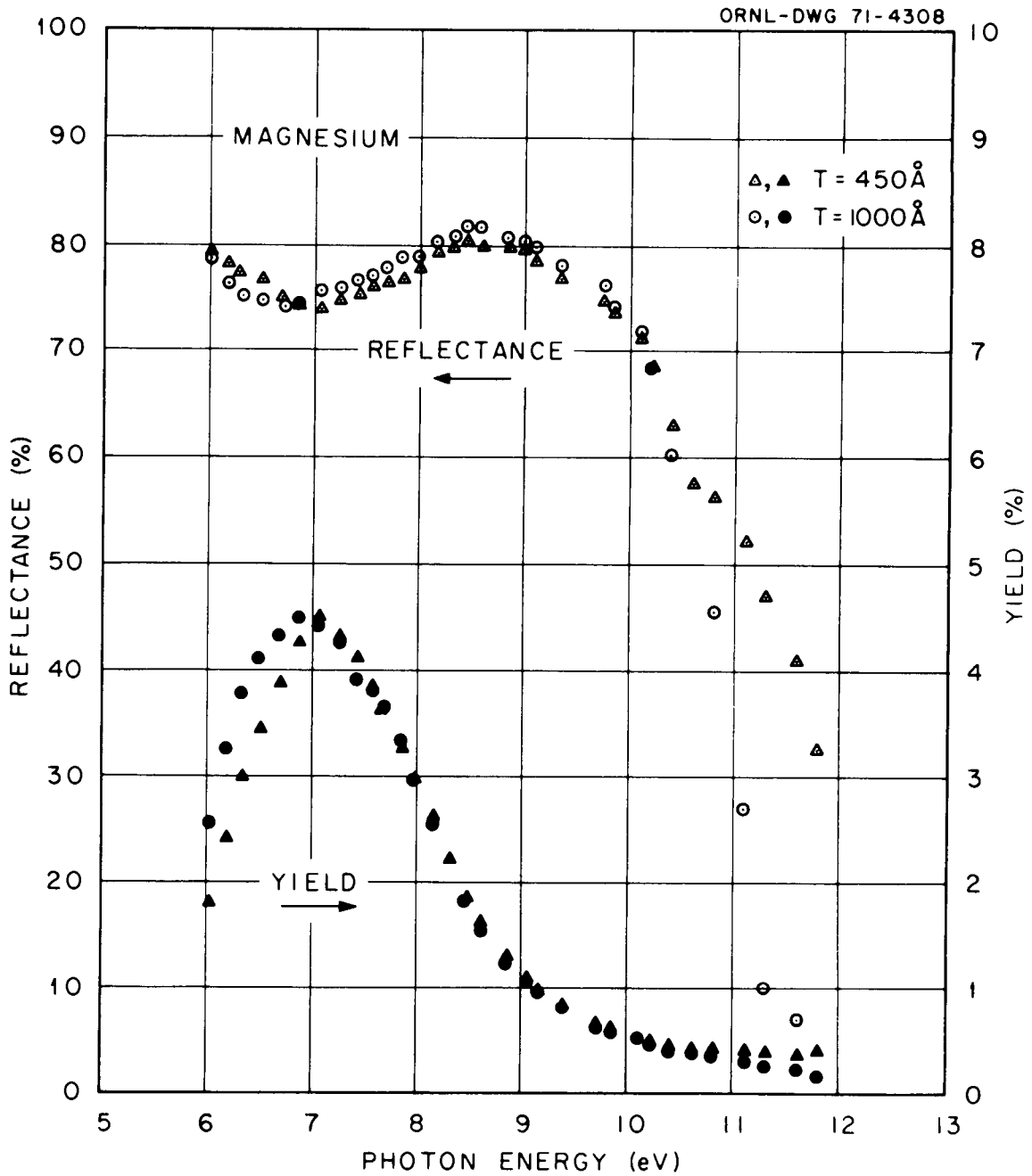

Figure 28. Simultaneously measured yield and reflectance data for magnesium.

example in Chapter II, Section V the quantum yield predicted for magnesium at 7 eV by Equation 19 is .013 electrons per absorbed photon or 1.3%. When one considers that the reflectance in this region is ~75%, the predicted yield per incident photon is only .33%. This must be compared with the experimental yield of 4.5%. Clearly this interpretation will not suffice.

As pointed out earlier in this section the dip in the reflectance in the 6-8 eV region is attributed to photon absorption by surface plasmons. Referring to Figure 26, page 110, it is seen that ~15% of the incoming photons create surface plasmons on our experimental films. According to the example presented in Chapter II, Section V, surface plasmons have a much higher probability of producing external electrons by either volume or surface decay than do photons. Thus it seems very likely that the large peak in the yield near the surface plasmon energy in magnesium is due to photon → surface plasmon → one electron transitions. This explanation was first applied to similar data for aluminum (Endriz and Spicer, 1970).

Electron energy distributions were measured according to the description in Chapter IV, Section V. Improvements in the vacuum and the electron energy resolution resulted in a significant improvement in the sample lifetime and energy distribution data. These measurements can be conveniently grouped into two categories, those taken with the H_2 continuous discharge light source and the LiF window and those taken at higher energies with the condensed discharge lamp and the thin film metallic windows.

Figure 29 shows a time study of the electron energy distribution for magnesium at 10.2 eV. A comparison with Figure 21, page 100, which shows distributions taken at 10.2 eV with the old retarding cage illustrates the improvement in resolution and sample life effected by the combination cold trap-electron retarding can.

Figure 30 shows energy distributions for photon energies between 6.65 and 11.2 eV. Each curve represents an average of first distributions taken on several films. The distributions are normalized so that the area under each curve is proportional to the yield at that photon energy. The change in shape is due to the appearance of scattered electrons in the low energy tail as the photon energy is increased. The overall decrease with increasing photon energy is due to the decrease in total yield discussed previously. There is no sharp structure in the distributions.

Toward the end of the study an apparatus became available at the University of Tennessee with ultimate pressures in the low 10^{-10} Torr region. In addition the new apparatus had nearly ideal spherical electron retarding geometry. Consequently, the magnesium energy distribution measurements were repeated in this new apparatus to verify the data taken in the Oak Ridge apparatus. The results of these measurements are given in Figure 31. These energy distributions are a single measurement on a single film. The general shapes of the energy distributions are the same as those taken in the Oak Ridge apparatus. The energy distributions taken in the

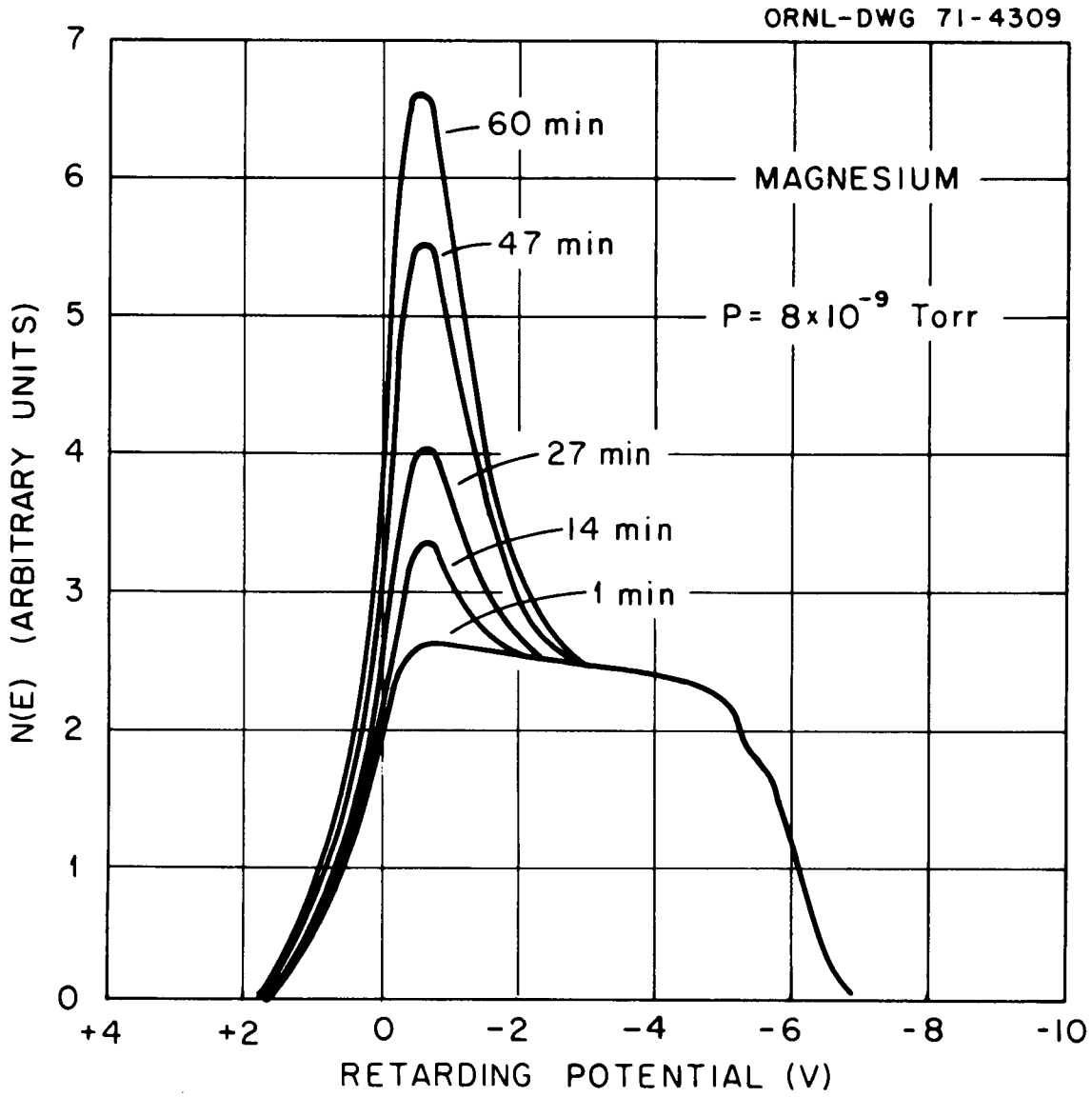

Figure 29. Photoelectron energy distributions taken as a function of time for magnesium ($h\nu$ = 10.2 eV) in the improved apparatus.

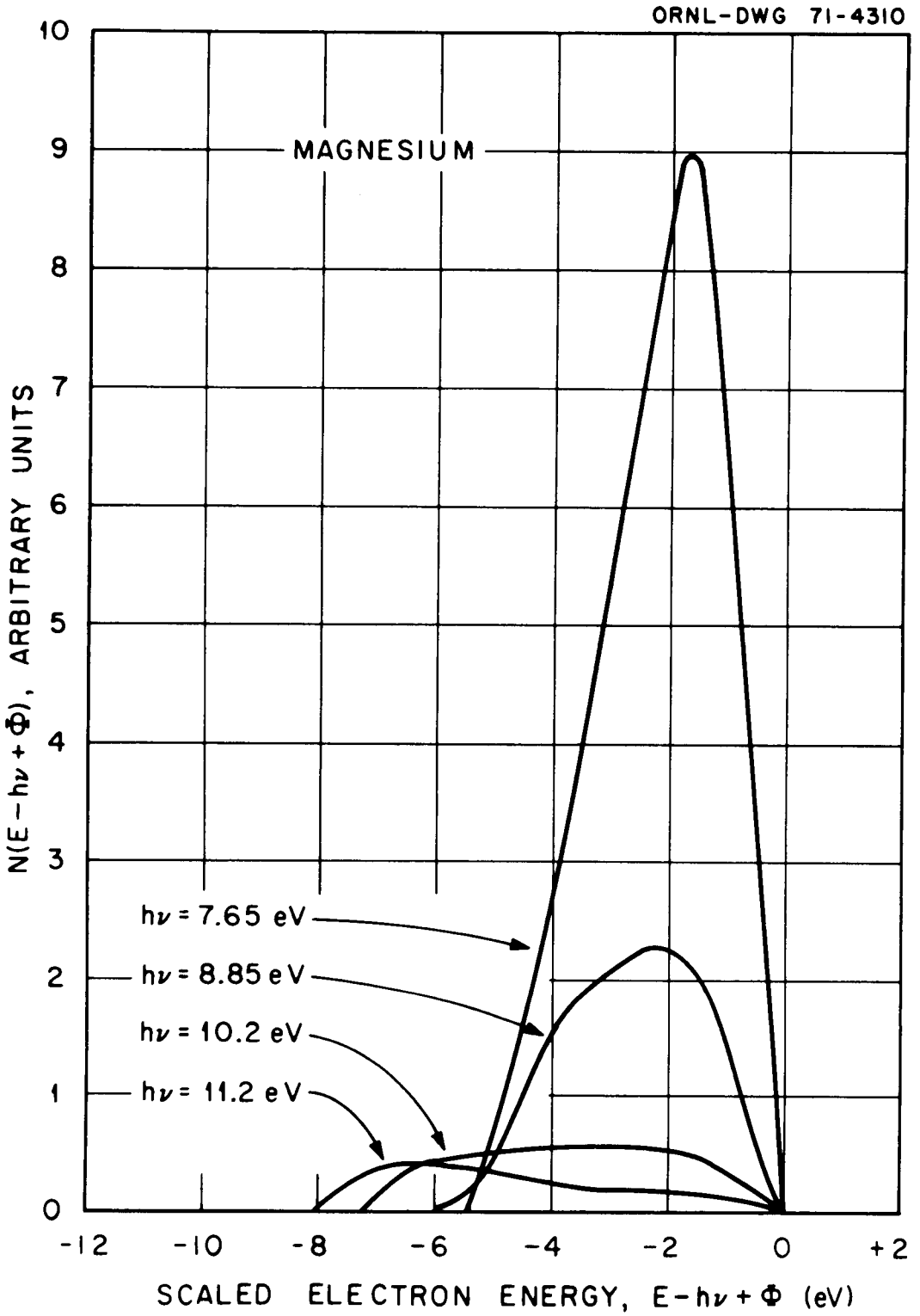

Figure 30. Photoelectric energy distributions taken at various photon energies and normalized to total yield.

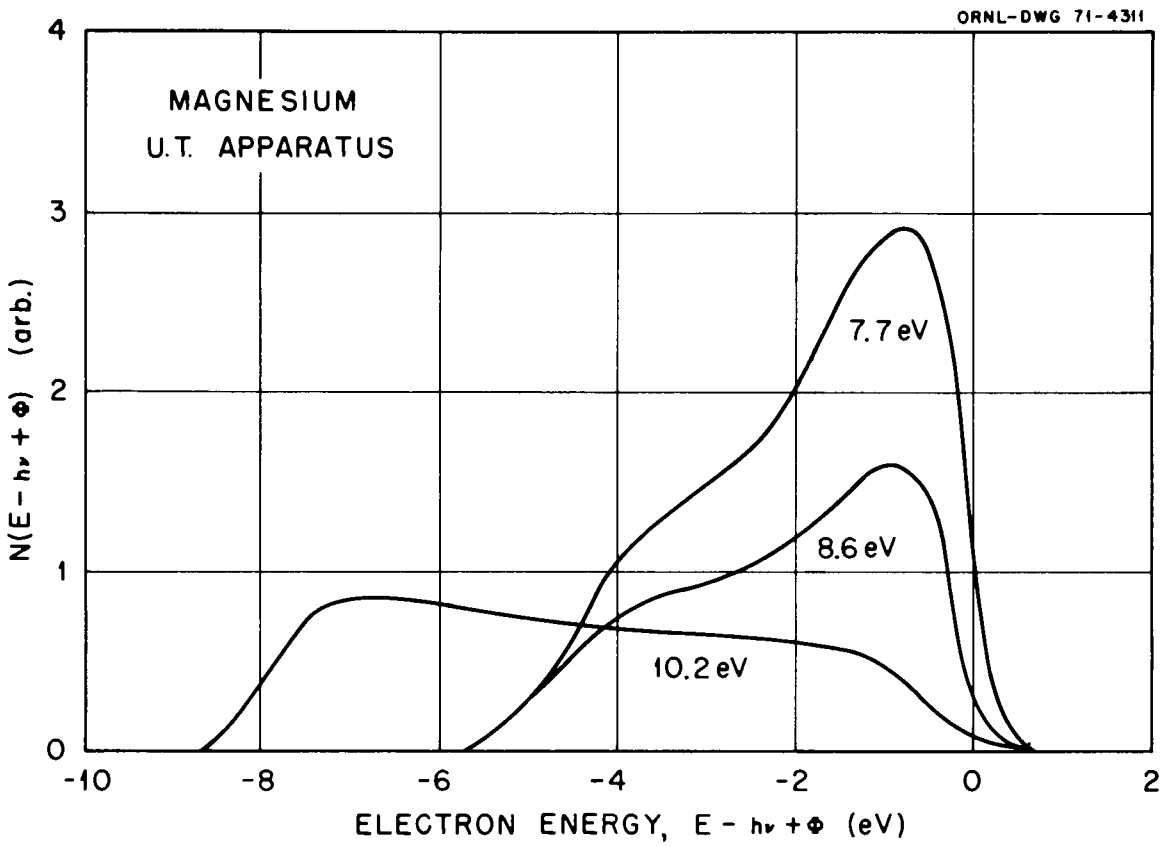

Figure 31. Unnormalized photoelectron energy distributions for magnesium at various photon energies taken in the University of Tennessee apparatus.

University of Tennessee apparatus are not normalized so only the shapes of the curves are significant.

The lower pressures obtained in the University of Tennessee apparatus gave a longer sample life. The high energy edges of the distributions taken in the University of Tennessee apparatus rise more sharply than the high energy edges of the distributions taken in the Oak Ridge apparatus. This sharper rise is presumably due to the better energy resolution afforded by the spherical retarding geometry.

Energy distributions taken at high photon energies using thin metallic windows and the condensed discharge light source are shown in Figure 32 together with energy distributions taken at lower energies. In this figure the distributions were not normalized to total yield but were set equal at 2 eV below the maximum. This was done because the absolute yield was not known above 11.75 eV and because normalization at 2 eV below the maximum illustrates how the relative importance of scattered electrons increases with photon energy. The Fermi energy of magnesium is ~6.2 eV (Watson et al., 1968) so no primary electrons are expected below -6.2 eV in Figure 32. By normalizing the distributions at -2 eV where most of the electrons are primary, the area under the curves at energies less than -6.2 eV is a measure of the number of scattered electrons.

Magnesium is a nearly-free-electron-like metal (Ketterson and Stark, 1967; Watson et al., 1968) whose density of states is nearly parabolic. The

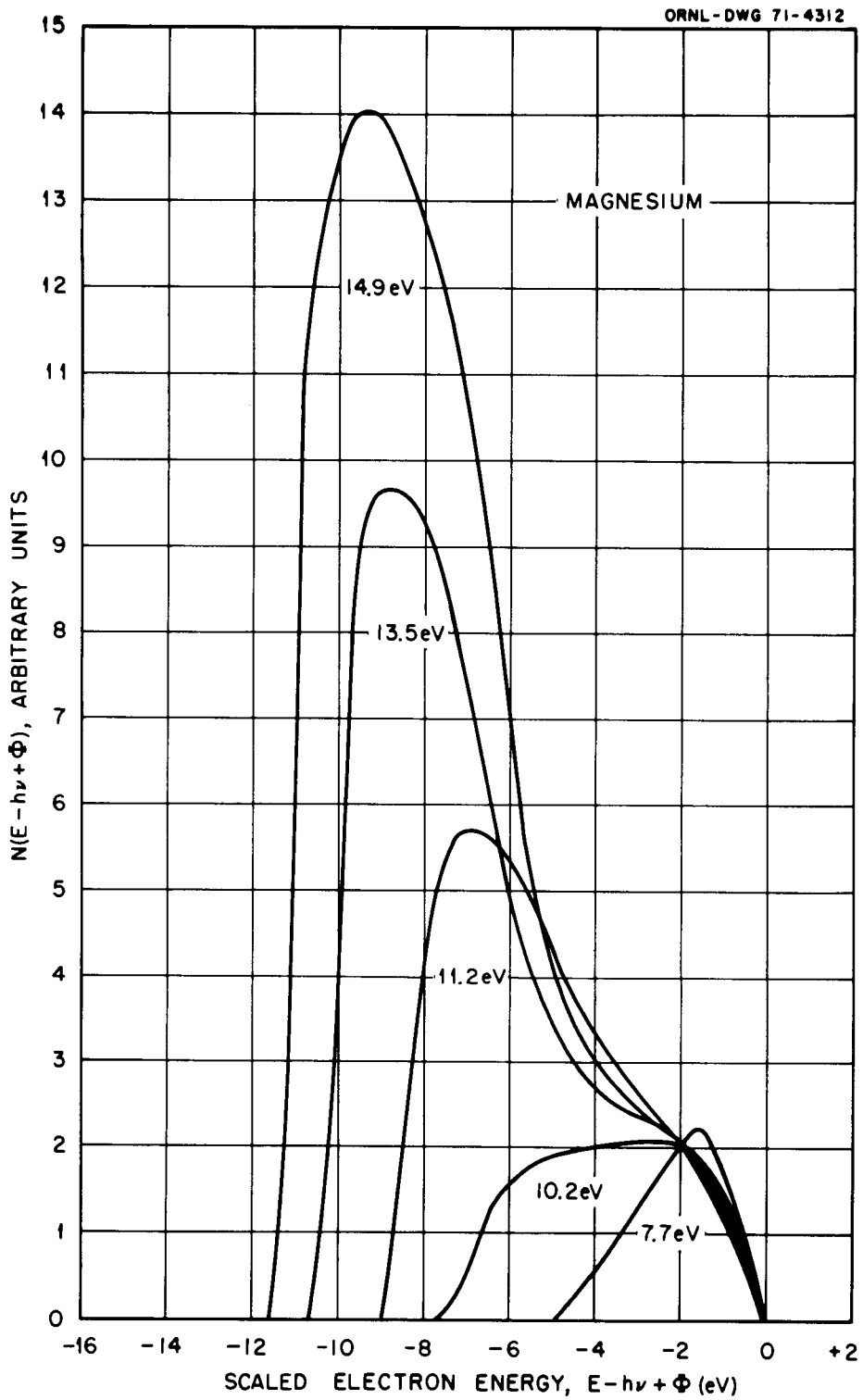

Figure 32. Photoelectron energy distributions for magnesium taken at energies above the LiF cut off together with energy distributions taken at the lower energies.

deviation from the parabolic nature consists of small structure within 2 eV of the Fermi level introduced by energy gaps at the Brillouin zone surfaces. The density of states has been obtained both theoretically and experimentally from soft x-ray emission by several investigators. Watson et al. (1968) give several references. In the framework of the indirect transition model (Chapter II, Section II) one expects that the high energy portion of an energy distribution should approximate the high energy portion of the valence band density of states.

Our data do not show strong structure in the high energy portion of the electron energy distributions but a small shoulder is evident in the high energy edge of the 10.2 eV distribution (see Figure 29, page 118) which may be due to the structure in the density of states. Improved electron energy resolution will be necessary to verify this shoulder. For the lower photon energies our energy distribution curves are roughly parabolic in shape which is expected from the indirect transition model. For the higher photon energies, the scattered electrons overshadow the primaries except in the high energy portion of the distribution. As pointed out in Chapter II, Section II, it is necessary to study the behavior of identifiable peaks as a function of photon energy in order to distinguish between direct and indirect transitions.

One of the initial goals of this study was to look for evidence of discrete surface or volume plasmon energy losses by photoexcited electrons. These losses are described in Chapter II, Section IV. A strong surface plasmon loss, for example, would shift a substantial portion of the primary electrons in

an energy distribution lower in energy by an amount equal to the surface plasmon energy. It was expected that this shift would show up as a peak or shoulder in the energy distributions taken at the higher photon energies. In magnesium, the surface plasmon energy is ~ 7.5 eV so one would expect structure in Figure 32, page 122, near -7.5 eV. Structure is not evident so we may conclude that the loss is overshadowed by electrons that have suffered one or more inelastic electron-electron scattering events. Structure corresponding to discrete surface plasmon losses has been reported in the alkali metals (Smith and Spicer, 1970).

IV. ELECTRON ATTENUATION LENGTHS

In Chapter II, Section III two methods for obtaining electron attenuation lengths from photoelectric data were described. In this section the magnesium photoelectric data of the previous section as well as the aluminum photoelectric data of Stanford are analyzed by the first method. In addition, aluminum photoelectric data as a function of the angle of incidence of the exciting radiation are presented and analyzed to obtain the attenuation length by means of the second method described in Chapter II, Section III.

Referring to Equation 46 it is evident that we must know the internal density of excited states $N'(E)$, the reflectance R, the optical absorption coefficient α, the critical angle for electron emission θ_c, and the density of

emitted electrons N(E) in order to obtain the attenuation length ℓ. Magnesium and aluminum are free electron-like metals so $N'(E)$ was obtained by assuming transitions from a parabolic initial density of states to final states whose density is independent of energy (Chapter II, Section II). The reflectance was experimentally measured, α was calculated from the data of Daude et al. (1967; 1969) and θ_c was obtained from Equation 26. The density of emitted electrons was obtained by normalizing the energy distributions to the total yield.

In practice, the most energetic 2 eV of the emitted electrons were compared with theory. A plot was made of the fraction f of electrons contained in the most energetic 2 eV of the energy distributions vs. photon energy. This fraction multiplied by the absolute yield, Y, gave the absolute yield of electrons with energies within 2 eV of the maximum energy. Most of these high energy electrons are primary electrons that have not suffered energy loss, and they must have originated from the most energetic 2 eV of the internal density of excited states. Recalling that $N'(E)$ is normalized, the fraction of the internal density of excited states that contributes to the top 2 eV of the external distribution f' is

$$f' = \int_{h\nu + E_F - 2}^{h\nu + E_F} N'(E)\, dE$$

For magnesium, assuming that the Fermi level E_F is 6.2 eV, f' is .442.

The critical angle for electron emission, θ_c was evaluated at $E = h\nu + E_F - 1$, which is the midpoint of the most energetic 2 eV of the distribution. The result of the calculation is necessarily an average attenuation length for electrons in the most energetic 2 eV of the distribution for a given photon energy. We have assigned a typical energy of $h\nu + E_F - 1$ to these electrons. For this analysis then, Equation 46 takes the form

$$\ell(h\nu + E_F - 1) = \frac{4\, fY}{[1 - R(h\nu)]\, \alpha(h\nu) \sin^2\left[\theta_c(h\nu + E_F - 1)\right] f'} \tag{73}$$

Equation 46 is an analytic approximation to Equation 19 so for actual calculations Equation 19 was numerically inverted. Equation 46 was used in the discussion for clarity.

The results of the attenuation length analysis for seven magnesium films is shown in Figure 33 together with the electron-electron scattering theory of Ritchie and Ashley (1965). Electron-electron scattering is the only important inelastic volume scattering mechanism in the energy region under consideration. The scatter in the data as well as the divergence of experiment and theory at lower energies deserve comment. The scatter in the attenuation length at all energies is due to the scatter in the photoelectric yield of the various films.

The strong deviation from the theory in the 8-9 eV region can be understood in terms of surface plasmon-one electron transitions. The theory

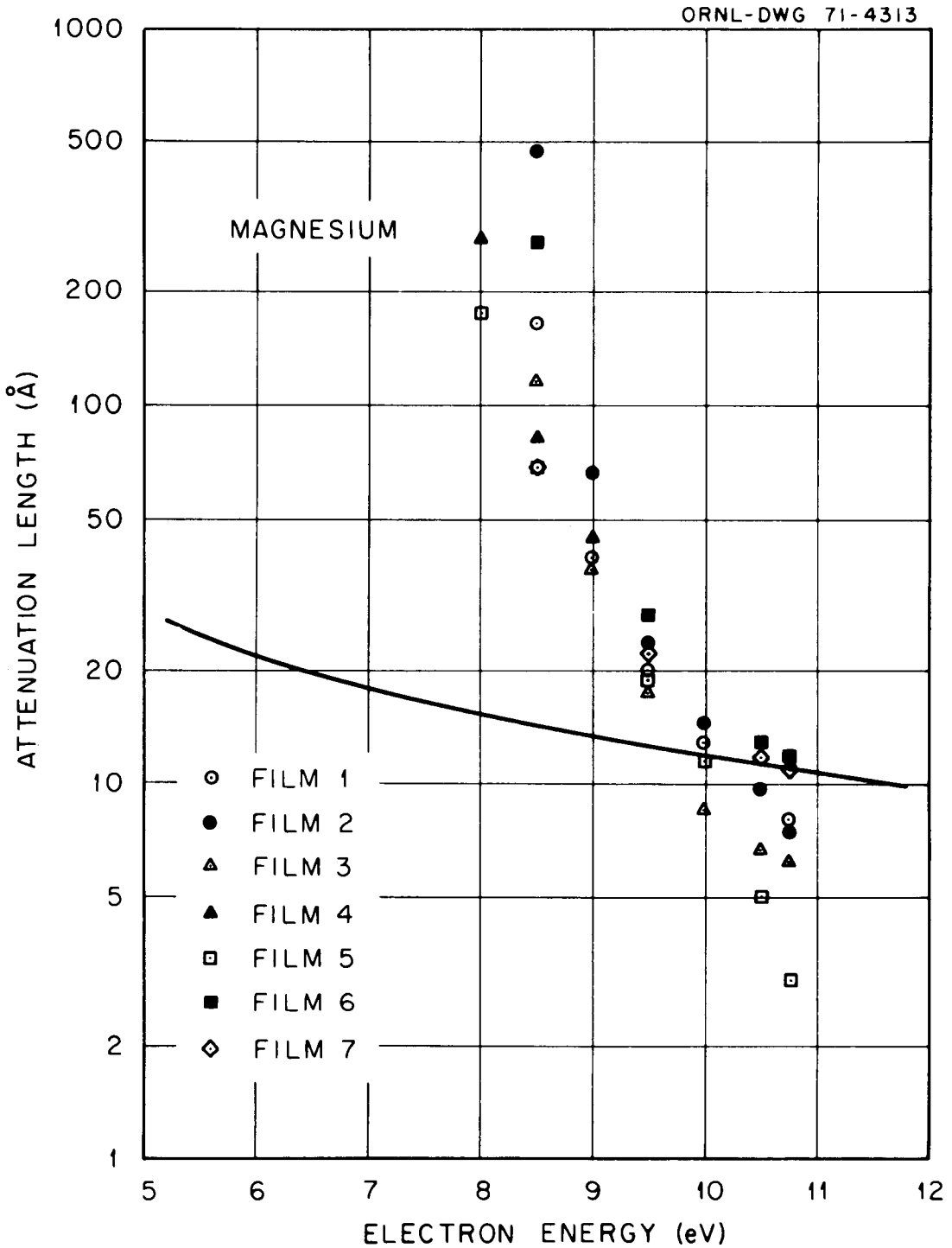

Figure 33. Attenuation length for electrons in magnesium as a function of energy above the Fermi level obtained from the absolute yield model.

The data are compared with theory of Ritchie and Ashley [J. Phys. Chem. Solids 26, 1689 (1965)].

of these transitions is discussed in Chapter II, Section V, and the experimental evidence for them is discussed in the previous section of this chapter. The important property of these transitions that is of interest here is that they cause an increase in the measured photoelectric yield that is not taken into account by the volume photoemission model. It is clear from Equation 73 that an increase in the yield, Y, leads to an increase in ℓ, all other factors being constant. Thus surface plasmon-one electron transitions have raised the yield of our experimental films and increased the attenuation length extracted from the photoelectric data.

Surface plasmons may also act to suppress the photoelectric yield of electrons whose energies lie above the surface plasmon energy of the metal. As discussed in Chapter II, Section IV, the possibility exists that a surface plasmon can be created by an electron crossing the metal-vacuum interface. Thus the electron which would otherwise escape with its full energy would be degraded in energy by an amount equal to the surface plasmon energy. The generated surface plasmon could then decay by any of the mechanisms discussed in Chapter II, Section V. A small fraction of the decaying surface plasmons would generate external electrons, but their energy would be less than that of the primary. The mechanism described in the preceding paragraph should not be confused with the mechanism described in this paragraph. In the former mechanism the observed yield of electrons with energies on the order of or less than the surface plasmon energy is enhanced by photon-surface plasmon-one electron transitions while in the latter case the yield of electrons with

energy above the surface plasmon energy is suppressed by electron-surface plasmon transitions.

A closely related method for obtaining the attenuation length for photoelectrons is to compare the energy distributions with those predicted by the model using the attenuation length as a fitting parameter. This scheme has the advantage that one can excite the electrons by photons whose energies are well removed from the surface plasmon energy, thus avoiding the complication introduced by photon→ surface plasmon→ one electron transitions. The disadvantage of the method is that only the high energy portion of an electron energy distribution is entirely free from scattered electrons. Thus one would expect this method to give good attenuation length results for electrons with energies near that of the photons used to excite them and to give attenuation lengths that are too large for lower energies. Figure 34 which shows attenuation lengths calculated from 10.2 eV and 11.1 eV energy distributions shows the expected behavior. The experimental attenuation lengths shown in this figure are closer to the theory at lower energies than the values shown in Figure 33, page 127, and are no doubt nearer the truth.

Aluminum is also a free-electron-like material so the analyses just described for magnesium should be suitable for aluminum. Figure 35 shows the attenuation lengths extracted from the aluminum photoelectric data of Stanford et al. (1966). The first method described in the previous description of the electron attenuation length analysis of magnesium was used. The

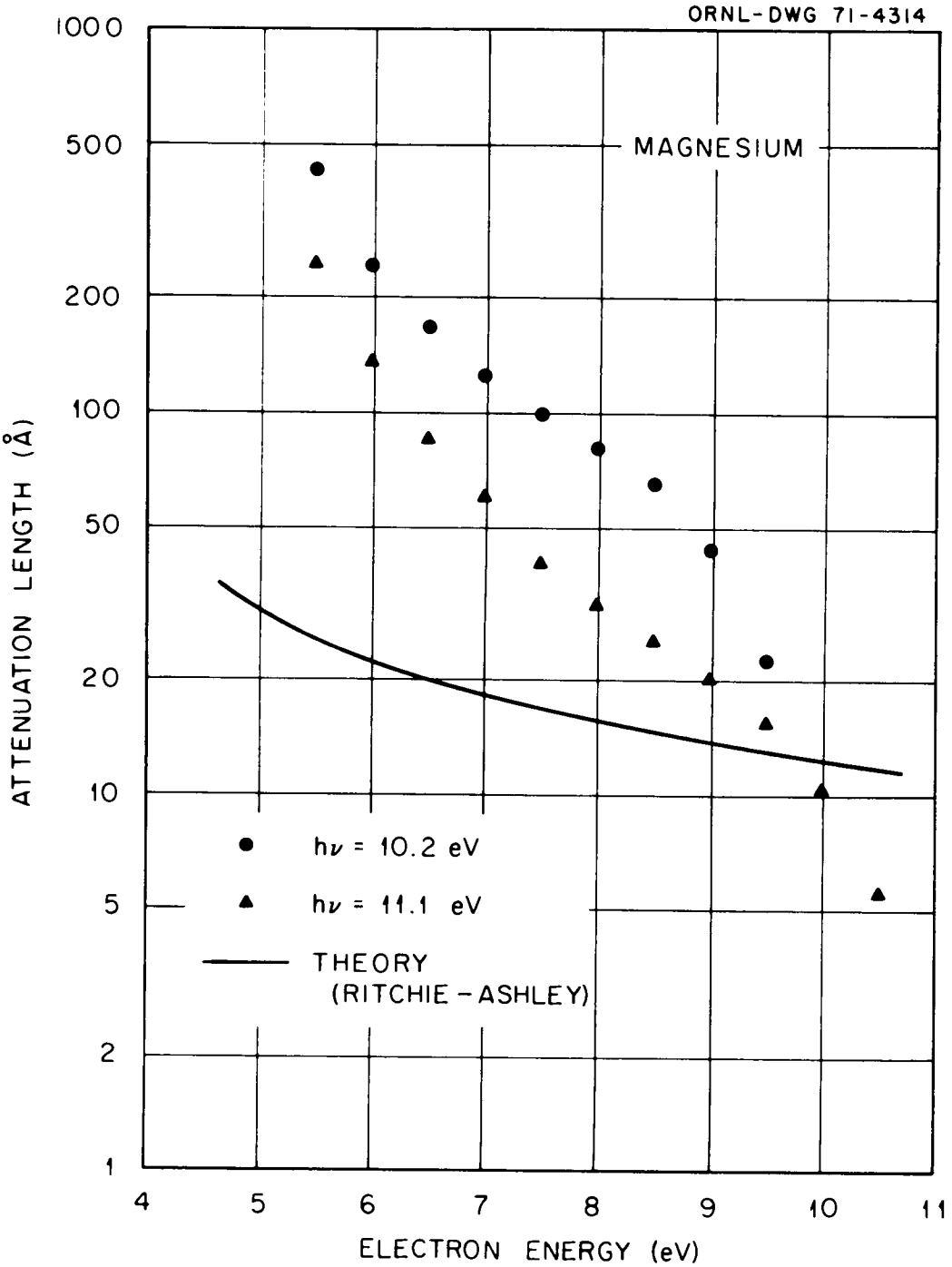

Figure 34. Attenuation length for electrons in magnesium as a function of energy above the Fermi level obtained by comparing experimental and theoretical energy distribution curves.

The data are compared with the theory of Ritchie and Ashley [J. Phys. Chem. Solids 26, 1689 (1965)].

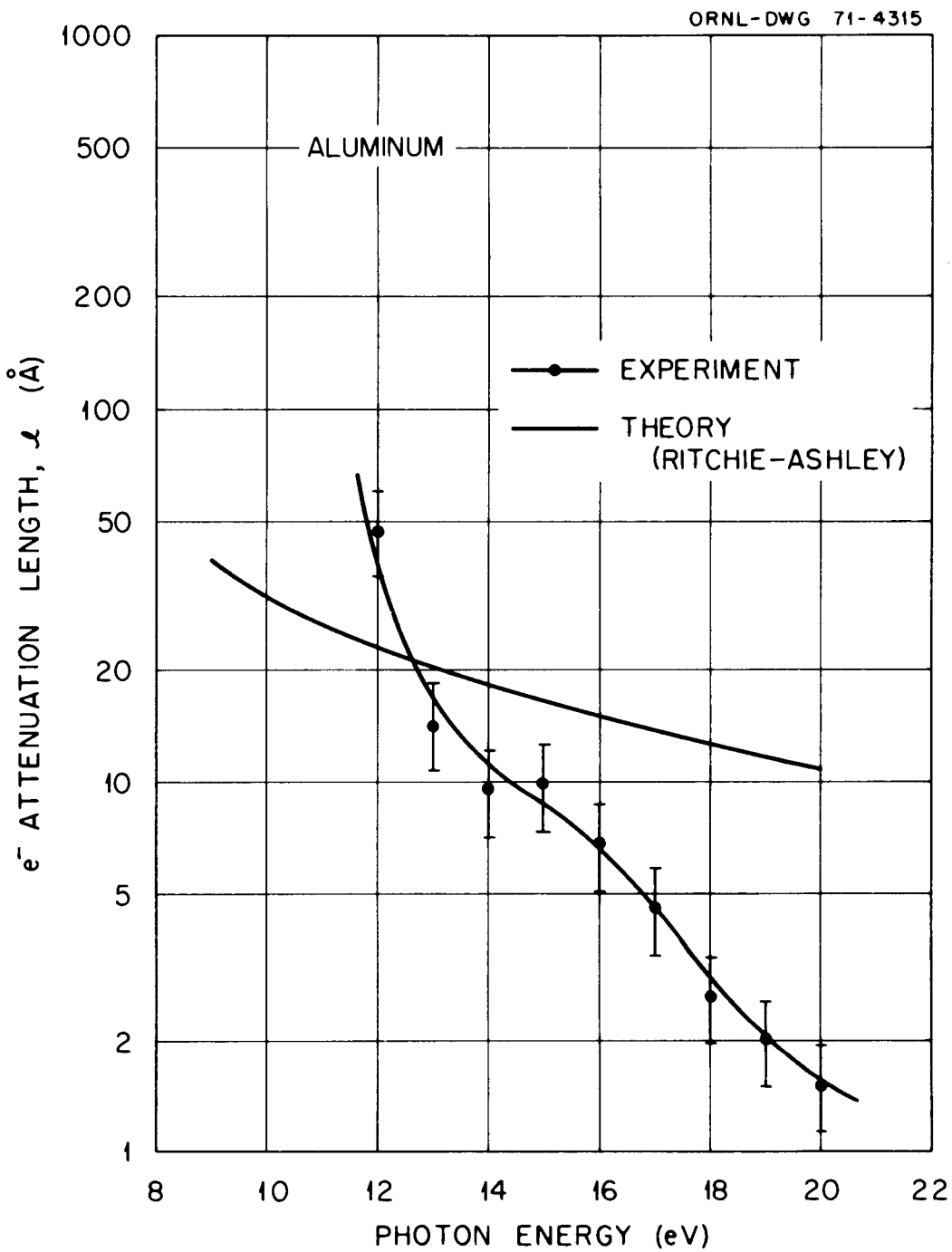

Figure 35. Attenuation length for electrons in aluminum as a function of energy above the Fermi level obtained from the absolute yield model.

The data are compared with the theory of Ritchie and Ashley [J. Phys. Chem. Solids 26, 1689 (1965)].

aluminum data exhibit the same general trends as the magnesium data of Figure 33, page 127, and the same interpretation of the deviations from the theory can be made. The sharp rise in the attenuation length as the surface plasmon energy (10 eV in aluminum) is approached is attributed to photon-surface plasmon-one electron transitions. At higher energies experimental values of the attenuation length are lower than the theoretical values. This is interpreted as a suppression of the yield due to electron surface plasmon transitions. The arguments are the same as for magnesium which was previously treated.

In Chapter II, Section III, an independent method for obtaining the attenuation length of photoelectrons based upon the variation of the yield with the angle of incidence of the exciting radiation is described. In what follows, the experimental measurements and results of the analysis are described. The angle method has the advantage of not requiring measurement of the absolute yield. Measurement of the yield as a function of angle with respect to the yield at O° is sufficient.

Data were taken on five aluminum films in accordance with the procedures in Chapter IV, Section VII. Analysis was made by making a least squares fit to Pepper's (1970) equations. The index of refraction, attenuation length and thickness of the film were used as fitting parameters. In Pepper's (1970) model for the yield it was assumed that all the escaping electrons traveled through the photoemitter normally to the surface. This model is not too realistic at higher energies because the escape cone is fairly

large and a correspondingly large fraction of the escaping electrons travel through the film nonnormally. For this reason we rederived Pepper's yield equations for the more general case of electrons exiting non-normally and reanalyzed the data. Assuming a maximum escape angle of 45° for electrons photoexcited in aluminum by 21.2 eV photons we found that the attenuation lengths were increased by $\sim 15\%$ over those found using Pepper's yield equations. This is a small correction compared with the spread in attenuation lengths found using various fitting methods, so the table and figures prepared using Pepper's original equations were retained. This study has been published (Gesell and Arakawa, 1971).

Pepper (1970) calculated the absorption of the radiant energy throughout the photoemissive material and then treated the diffusion and escape aspects of the photoemission process with a simple model attributable to Spicer (1958). According to this model the probability that an electron excited at a depth y in the photoemissive medium escapes into the collecting medium is given by $C \exp(-y/\ell)$. The electron attenuation length is ℓ which depends upon the diffent physical mechanisms which de-excite the electron such as e^--e^- scattering and e^--phonon scattering. The factor C takes into account the excitation probability of penetrating the surface barrier.

If the absorption of the radiant energy is given by $\eta(y)$, then the quantum yield for a photoemitter of thickness d may be written as

$$Y = C \int_0^d e^{-y/\ell} \eta(y)\, dy = CF(\ell)$$

where $F(\ell)$ is a function of the optical constant of the photoemissive material and substrate, the thickness of the photoemitter, the wavelength, polarization and angle of incidence of the light, and the attenuation length. The expressions for $\eta(y)$ and $F(\ell)$ are given in Equations 16a, 16b, and 22. In the absence of vectorial effects, the quantity C is independent of the angle of incidence of the exciting light and so a direct comparison of theory and experiment is possible by simply comparing measured values of the $Y(\theta)$ with the calculated values.

All the parameters in the theory are independently measurable except for the attenuation length ℓ. In practice, however, we have found that the equations are quite sensitive to two other parameters, the thickness of the film, d, and the index of refraction of the aluminum, n.

Figure 36 shows plots of the predicted relative yield for a single attenuation length (5.4 Å) and film thicknesses ranging from 1210 Å to 1250 Å. The sensitivity to film thickness is so great that a two parameter (attenuation length and film thickness) fitting routine was devised to fit the data to the theory. The sensitivity of the attenuation length to other parameters in the theory was evaluated by allowing the two parameter fitting routine to fit a single set of data using different values of the other parameters. The result of fitting this set of data using the literature values (Madden et al., 1962) for the optical constants of aluminum and glass and the calculated value for the polarization is ℓ = 5.4 Å. Figure 37 shows the attenuation length found by the fitting routine as a function of the

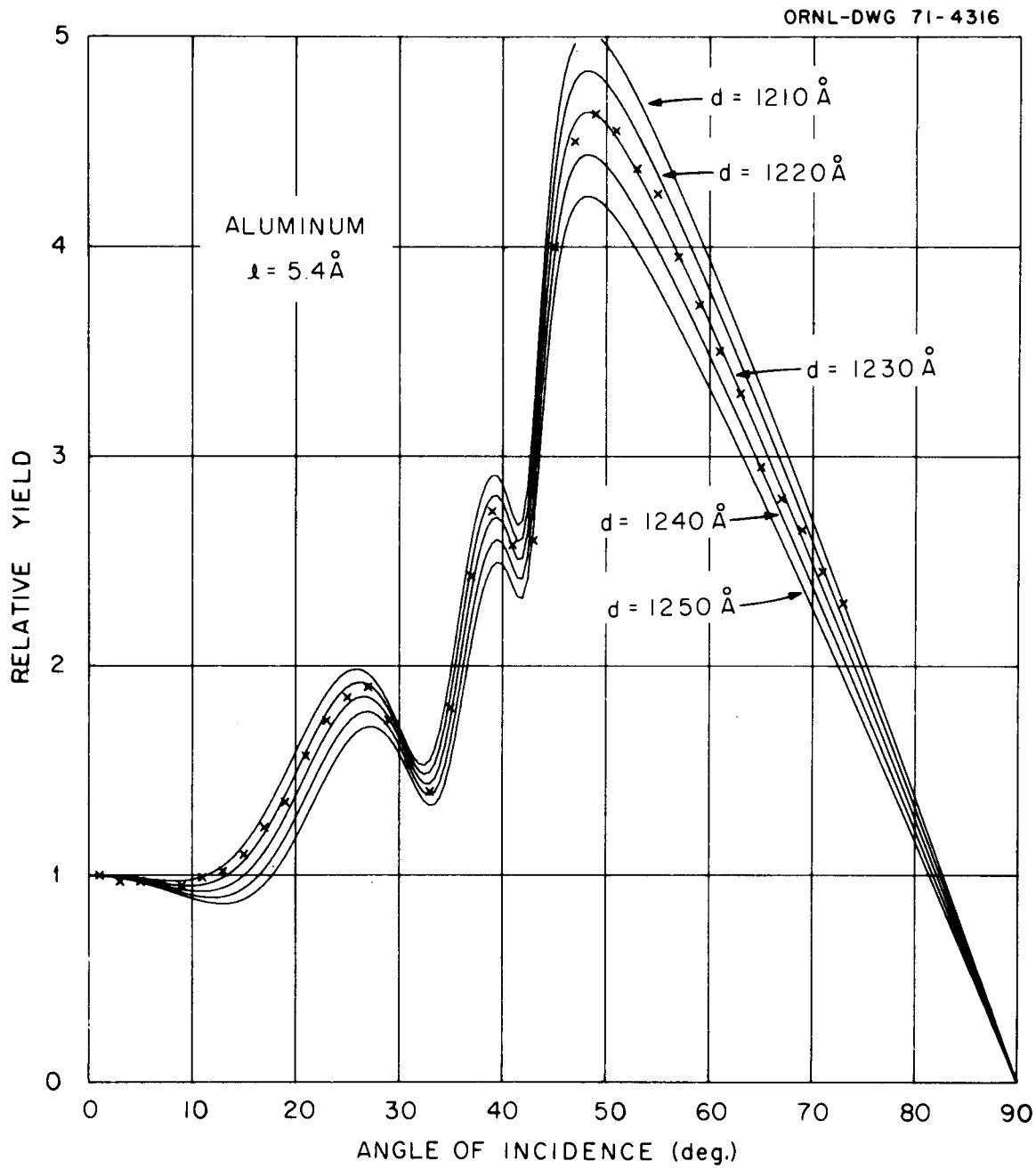

Figure 36. Thickness dependence of the relative photoelectric yield as a function of angle for aluminum.

In this figure the attenuation length is assumed to be 5.4 Å.

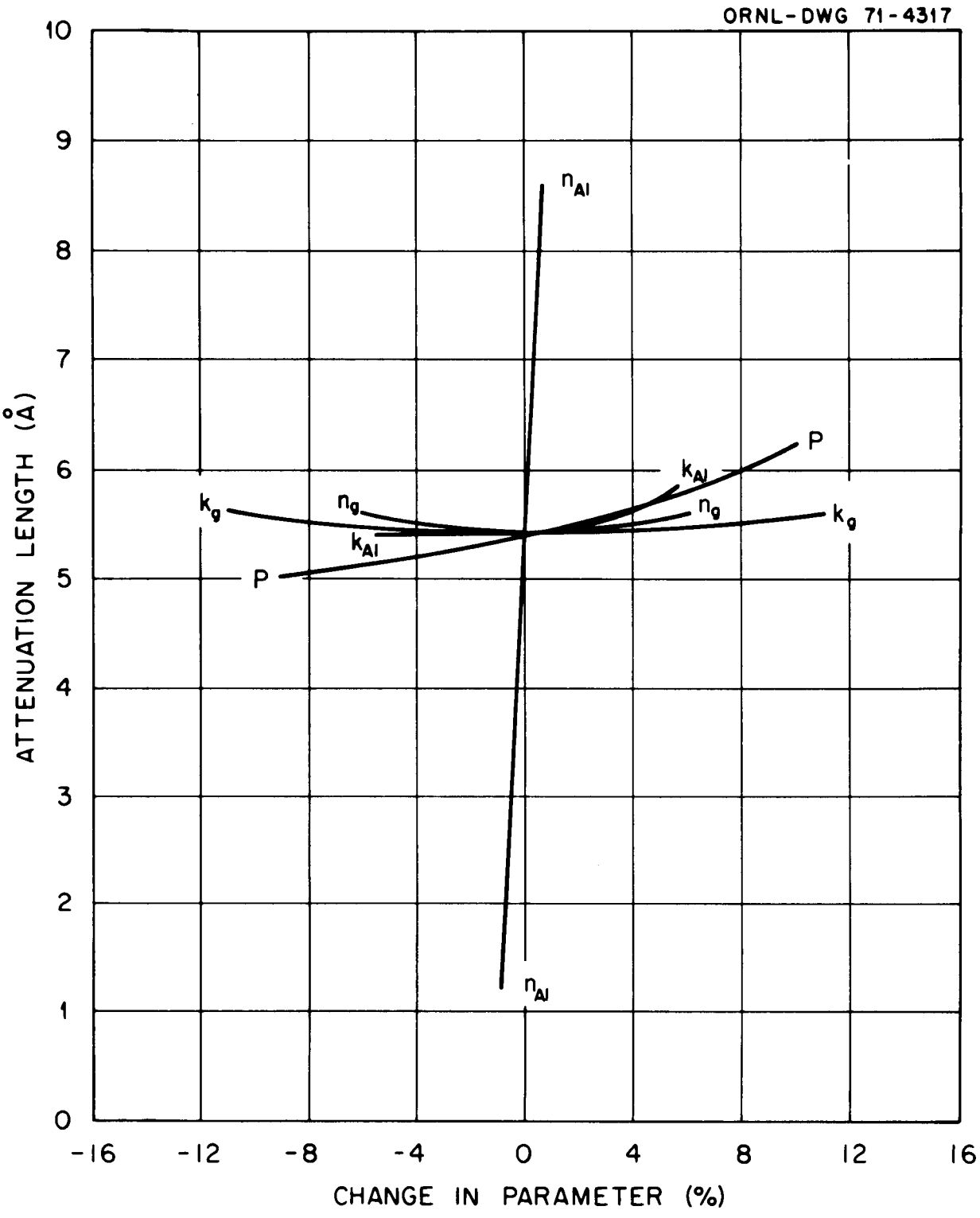

Figure 37. Dependence of the attenuation length obtained by fitting aluminum data with the angle model upon the parameters of the model.

percentage change in each parameter. It is clear that the method is extremely sensitive to the index of refraction of aluminum but quite insensitive to the remaining parameters. Thus an error in the polarization of the radiation, the optical constants of the substrate or the absorption coefficient of aluminum would not strongly affect the result but a very small error in the index of refraction of aluminum would lead to a large error in the attenuation length.

The sensitivity to d is such that the method provides an accurate means of obtaining film thickness from photoemission measurements alone. Because of this sensitivity to d and n the data were compared with the theory using two (d and ℓ) or three (d, ℓ, and n) parameter least squares fits. A fit was considered valid only if the values for d and/or n that gave the best fit fell within reasonable limits of their independently measured values. Two fitting criteria, absolute least squares, for which the quantity

$$\sum_{\theta = 0}^{\theta = \theta_{max}} \left\{ \left(Y(\theta)/Y(0) \right)_{exp} - \left(Y(\theta)/Y(0)_{theo} \right\}^2$$

was minimized, and relative least squares for which the quantity

$$\sum_{\theta = 0}^{\theta = \theta_{max}} \left\{ \frac{\left(Y(\theta) \right)_{exp} - \left(Y(\theta)/Y(0) \right)_{theo}}{\left(Y(\theta)/Y(0) \right)_{exp}} \right\}^2$$

was minimized, were employed.

Altogether, measurements were made on five films. Data from the last two films which were measured reliably to larger angles than the first three are presented here. Figure 38 shows the data for the first run of the two films, the best three-parameter fit obtained for each, and calculated results for attenuation lengths of 1 and 20 Å. It can be easily seen that the fit is very good and that it is possible using this method to distinguish between different escape lengths. The predicted relative yields for a larger range of attenuation lengths together with a set of data are shown in Figure 39. It is very clear that the curves for the larger attenuation lengths are quite different in shape and magnitude from the one giving the best fit.

The sensitivity of the angular dependence of the yield to the attenuation length is a function of the film thickness. If we define the sensitivity as the change in the relative yield per unit change in the attenuation length, $\Delta[Y(\theta)/Y(0)]/\Delta\ell$, then this sensitivity goes through several maxima and minima as the film thickness is increased. Referring to Figure 38, the thickness of film a was near that for a minimum in sensitivity, while the thickness for film b was near that for a maximum in sensitivity.

Table I summarizes the results of the fitting calculations. Except in the three-parameter fit, where n for aluminum was allowed to vary, the optical constants used were those of Madden et al. (1962). The main result is that the best fit for the electron attenuation length lies in the region $4\ \text{Å} \leq \ell \leq 12.8\ \text{Å}$.

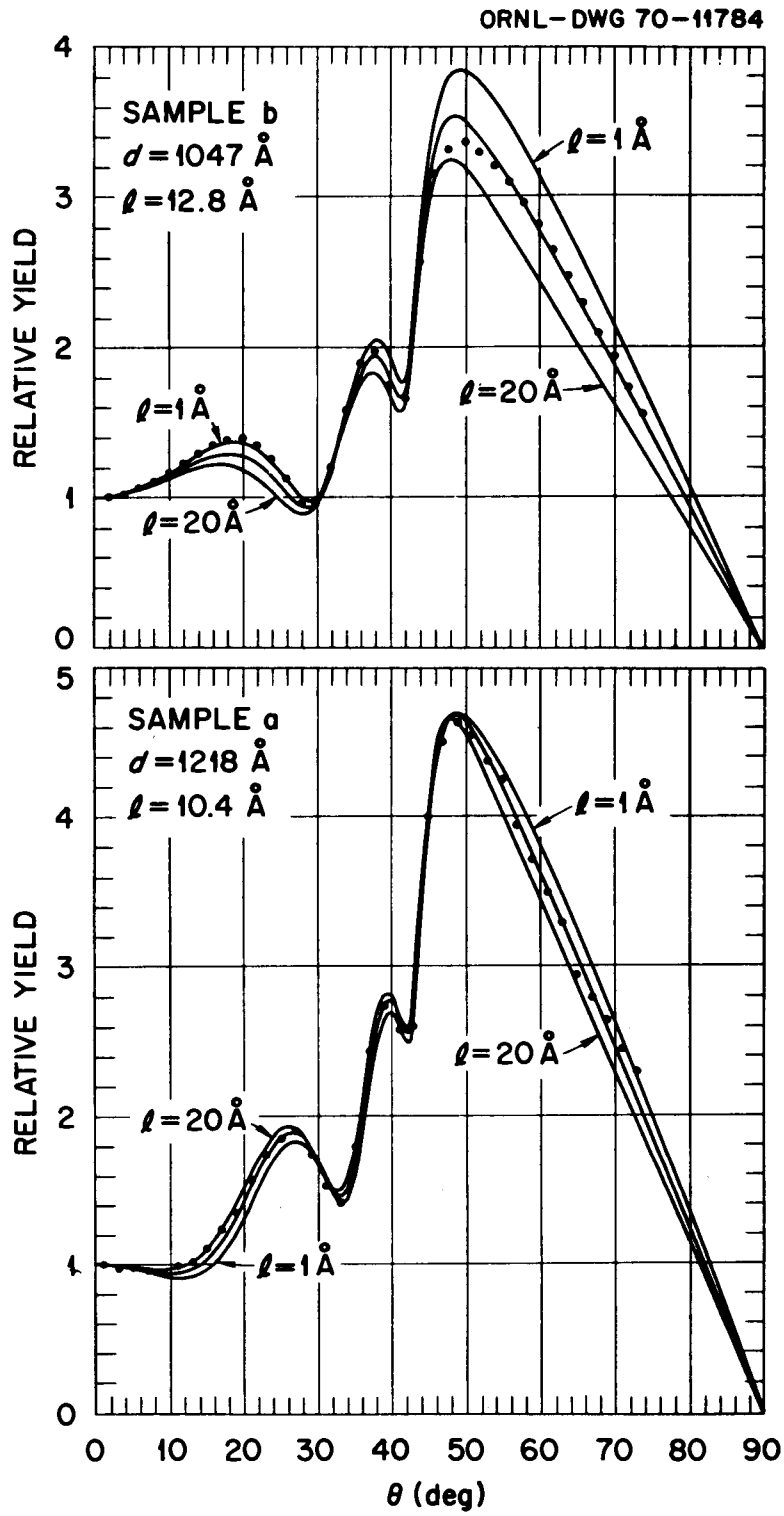

Figure 38. The relative yield as a function of angle for two aluminum films together with the best three parameter absolute least squares fit plus calculated curves for ℓ = 1 Å and ℓ = 20 Å for comparison.

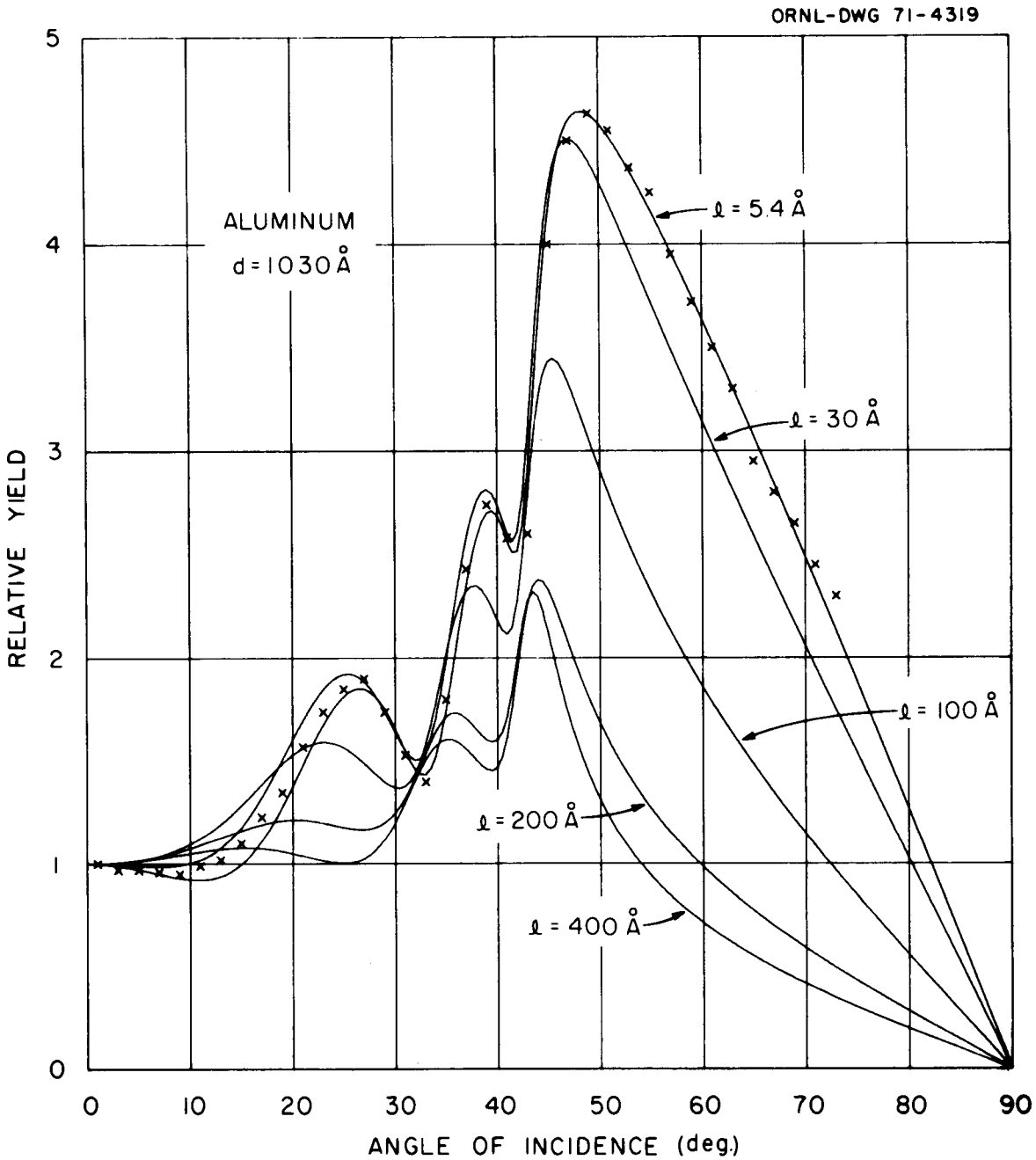

Figure 39. The relative yield as a function of angle for an aluminum film together with the best two parameter absolute least squares fit plus calculated curves for longer attenuation lengths for comparison.

TABLE I

RESULTS OF FITTING THEORY TO DATA

Fitting Parameters	Attenuation length ℓ (Å)	Film thickness d (Å)	Index of refraction n	Sum of squares
		Film a		
ℓ, d, n, abs.[a]	10.4	1218	0.716	0.157
ℓ, d, n, rel.[a]	11.4	1216	0.716	0.033
ℓ, d, abs.	5.4	1230	0.71[b]	0.245
ℓ, d, rel.	7.8	1227	0.71[b]	0.049
	Measured thickness 1250 ± 50 Å			
		Film b		
ℓ, d, n, abs.	9.8	1047	0.720	0.203
ℓ, d, n, rel.	12.8	1056	0.722	0.042
ℓ, d, abs.	4.0	1051	0.71[b]	0.382
ℓ, d, rel.	7.2	1064	0.71[b]	0.100
	Measured thickness 1050 ± 50 Å			

[a]The abbreviations abs. and rel. refer to the fitting criteria, either absolute least squares or relative least squares.

[b]Taken from R. P. Madden, L. R. Canfield, and G. Hass, J. Opt. Soc. Am. 53, 620 (1962).

The theoretical calculations of Quinn (1962) and Ritchie et al. (1965; 1969) as well as the experiments of Kanter (1970) who directly measured the attenuation of an electron beam indicate that the attenuation of an electron beam indicate that the attenuation length for electrons in aluminum is less than 50 Å for electron energies greater than ~ 5 eV above the Fermi level. On the other hand, the photoelectric experiments and analysis by Stuart and Wooten (1967) indicate that electrons which are about 9 eV above the Fermi level have a mean free path for electron-electron scattering of ~ 510 Å and a mean free path for phonon scattering of 130 Å. In support of Stuart and Wooten is the recent work of Pong et al. (1970) who find an attenuation length of ~ 230 Å for photoelectrons excited by 7.5 to 11 eV photons. Pong shows that his attenuation length, which includes all types of scattering, is equivalent to the separate e^--e^- and e^--phonon mean free paths of Stuart and Wooten.

Our results can be shown to be in substantial agreement with the calculations of Ritchie et al. (1965, 1969) if we average their values for the attenuation length over the energy distribution of initially excited electrons. For a free electron-like metal such as aluminum, the initial density of states is nearly parabolic. If we assume transitions to final states whose density is independent of energy, the average attenuation length $\bar{\ell}$ takes the form

$$\bar{\ell} = \frac{\int_0^{E_f} E^{1/2}\, \ell(E + h\nu - E_f)\, dE}{\int_0^{E_f} E^{1/2}\, dE}$$

where E_f is the Fermi energy. The result of this calculation is $\bar{\ell} = 12.7$ Å. If, on the other hand, a simple direct transition theory is used, the density of initial excited states is rectangular, and for this case the result is $\ell = 14.5$ Å. The result of Kanter (1970) is that the attenuation length for electrons in the energy range $4.5 \text{ eV} \leq E \leq 5.5 \text{ eV}$ is ~ 50 Å. Thus, our results agree qualitatively with those of Kanter since mean free paths are known in general to decrease with increasing energy. We disagree with the results of Stuart and Wooten (1967) and those of Pong (1970). A possible reason for this disagreement has been given by Endriz (1970) who suggested that the results of Stuart and Wooten may be in error because of surface plasmon-one electron transitions that were not considered by the authors. Pong's results may have been similarly influenced. The effect of these transitions is to raise the yield and thus make the attenuation length appear larger.

Figure 40 shows the experimental results for the attenuation length of electrons in aluminum found by others, our results on aluminum using both the absolute yield method and the angle method and the theory for electron-electron scattering of Ritchie and Ashley (1965). The single point obtained

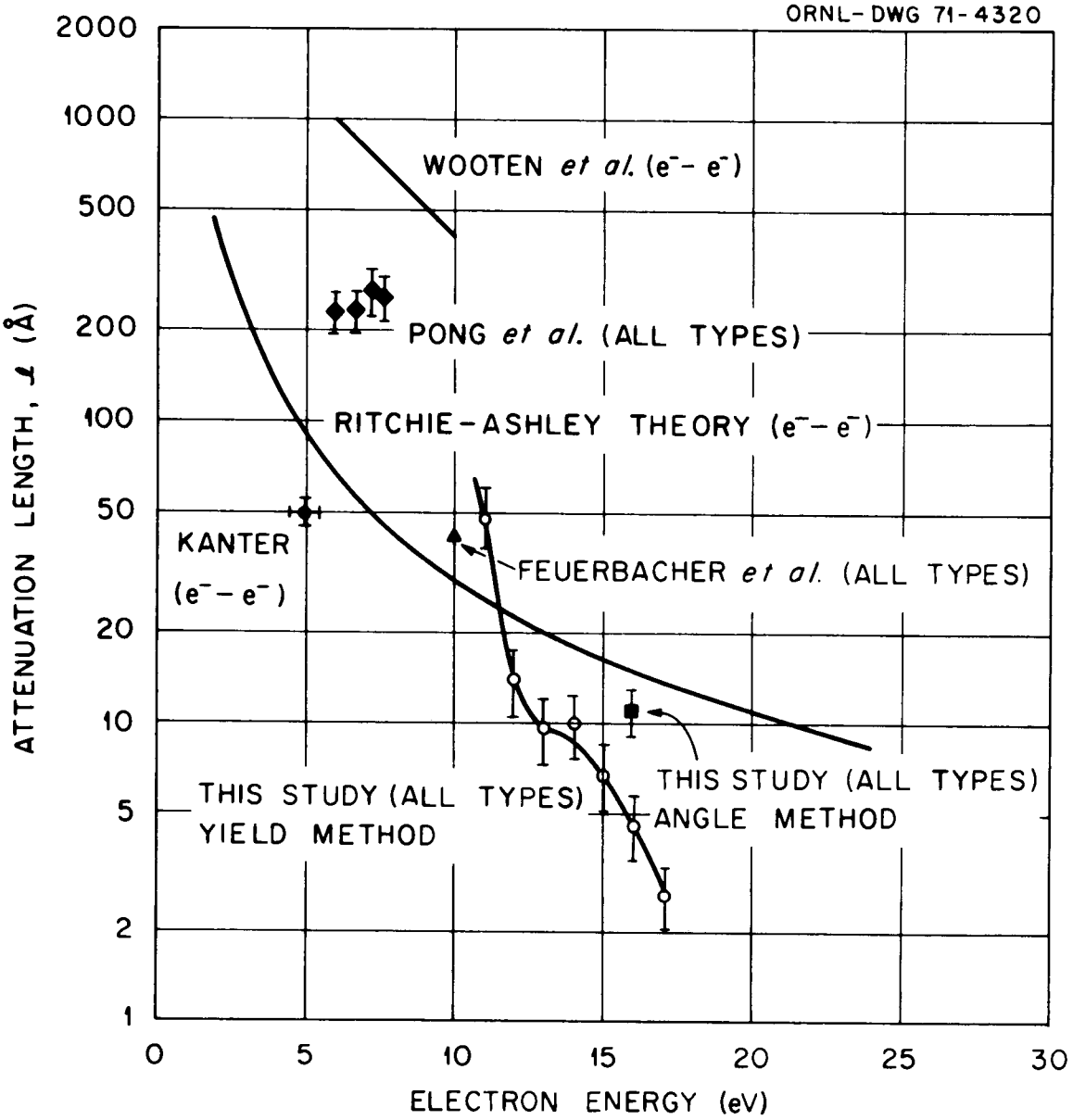

Figure 40. Attenuation lengths for electrons in aluminum as a function of electron energy above the Fermi level obtained from the angle method and the absolute yield method plus the experimental results of other investigators.

The results are compared with the theory of Ritchie and Ashley [J. Phys. Chem. Solids 26, 1689 (1965)].

from the angle method is plotted at 16 eV, which is the average energy of electrons excited in aluminum by 21.2 eV photons assuming indirect transitions to energy-independent final states. Our photoelectric results give reasonable values of the attenuation length when excitation is made by photons with energy greater than $\sim$ 12 eV but can be seen to diverge sharply from the theory toward lower energies. The results of Wooten et al. (1967) and Pong et al. (1970) are also seen to be higher than the theory. The method of Kanter (1970), in which the attenuation of electrons bombarding self supporting foils is measured, does not suffer from the problems associated with the photon-surface plasmon-one electron transitions. Kanter's valus is also seen to be in reasonable agreement with the theory. The value found by Feuerbacher et al. (1969) was obtained from the relative magnitude of the yield due to s and p components of light near the volume plasma wavelength. We derived their average energy using the same method used for our angle method. The result of Feuerbacher et al. is in reasonable agreement with the theory.

The attenuation length analyses performed by Pong et al. (1970) and by Stuart and Wooten (1967) were based upon photoelectric data taken with photons near the surface plasma energy of aluminum and appear to be too large. Our analyses for both aluminum and magnesium also appear to give values for the attenuation length which are too large near the surface plasma energies of the respective metals. A conclusion that can be drawn from these results is that extreme care must be used in interpreting photoemission data taken with

photons near the surface plasma energy. Any interpretation depending upon the absolute yield is likely to be in error.

V. PHOTOELECTRIC MANIFESTATION OF THE OPTICAL PLASMON RESONANCE

The theoretical basis for the photoelectric resonance due to the radiative surface plasmon is described in Chapter II, Section VI. The resonance was observed in the alkali metals in 1938 (Ives and Briggs, 1938) and studied recently in magnesium by Feuerbacher and Fitton (1970) and by Braundmeier et al. (1970).

Feuerbacher and Fitton (1970) studied the photoelectric yield as a function of incident angle of vacuum deposited films ~ 80 Å thick and found that the energy of the resonance extrapolated to 10.21 eV at an angle of 0°. The dispersion relation predicted by Equation 65 was not found, however. Instead of increasing in energy with increasing angle in accordance with Equation 65, the peak in the resonance decreased in energy with increasing angle.

Braundmeier et al. (1970) studied the inverse process. Electrons were allowed to bombard ~ 200 Å thick magnesium films and the photon emission was measured as a function of wavelength and angle. The resonance measured by Braundmeier et al. (1970) extrapolated to 10.43 eV at 0° angle of observation and the dispersion possessed the proper slope.

We have repeated the experiment of Feuerbacher and Fitton (1970) using thicker foils (~ 200 Å). The experiment was carried out in accordance

with the procedures described in Chapter IV, Section VI. Attempts were made to study the thin (~ 80 Å) foils described by Feuerbacher and Fitton (1970), but we were unable to obtain continuous (and hence conducting) films for thicknesses $\leqslant 200$ Å.

The results of our measurement are shown in Figure 41 together with the results of Braundmeier et al. (1970) and Feuerbacher and Fitton (1970). The present measurement extrapolates to a value of 10.46 eV which is consistent with the results of Braundmeier (10.43 eV) and somewhat higher than the result of Feuerbacher and Fitton (1970). The dispersion or slope of the present work is of the correct sign and is consistent with a film thickness of 200 Å if the point at 40° is disregarded. The quartz crystal thickness monitor gave ~ 200 Å for the thickness of the film as did a subsequent interferometric measurement.

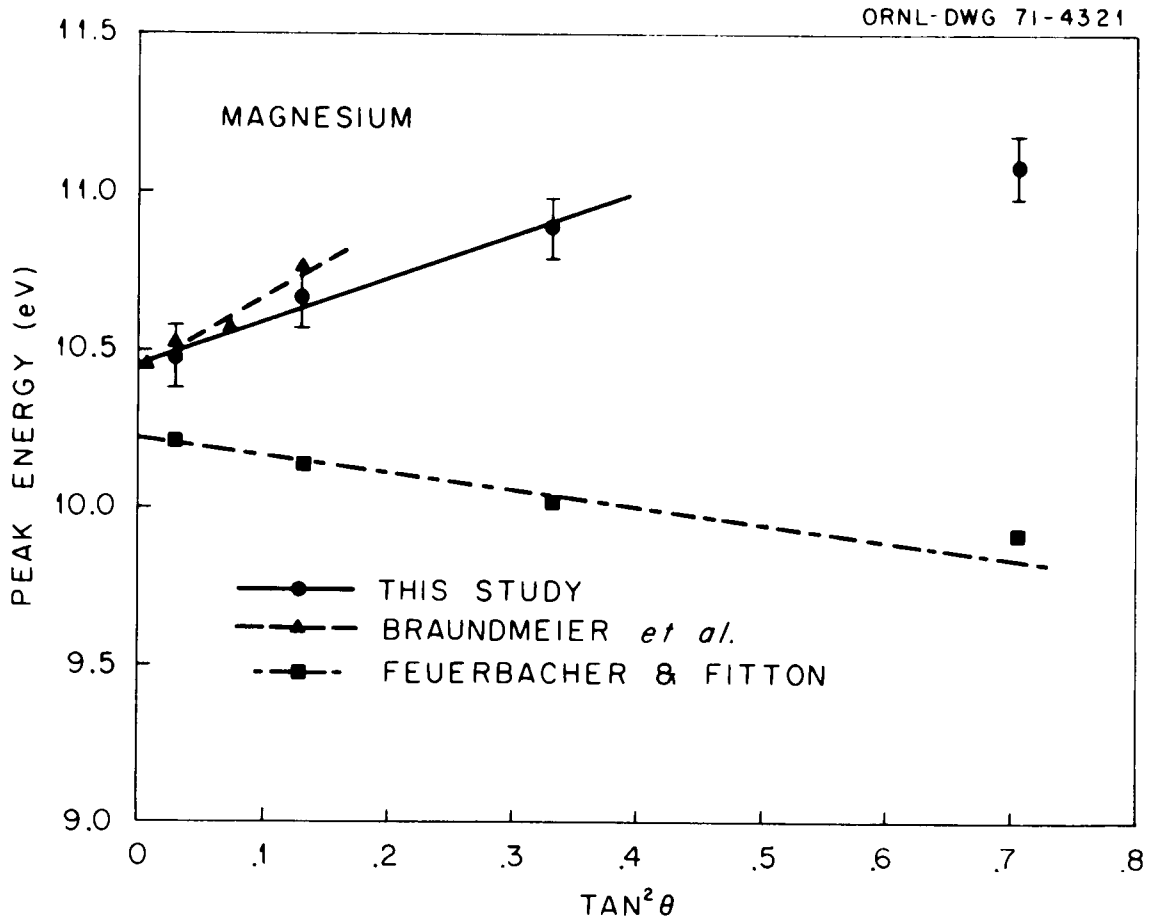

Figure 41. Energy of the peak in the photoelectric plasmon resonance as a function of $\tan^2 \theta$ together with the results of other investigators.

CHAPTER VI

SUMMARY AND CONCLUSIONS

I. THEORETICAL RESULTS

The optical excitation formalism of Pepper (1970) was combined with the transport and escape model of Berglund and Spicer (1964a) to give a complete model for the volume photoemission of unscattered electrons. The model is sufficiently general that it may be used to calculate energy distribution curves and yields for unaxially anisotropic films of arbitrary thickness upon arbitrary substrates as functions of the angle of incidence, polarization and wavelength of the exciting radiation. The model was extended to include once-scattered electrons for the case of a semi-infinite photoemitter.

II. APPARATUS

Electronic equipment for measuring electron energy distribution curves was built. A combination electron retarding can and cold trap was constructed to minimize sample contamination. Thin metallic windows were made and successfully employed to separate the 10^{-5} Torr monochromator pressure from the mid-10^{-9} Torr sample chamber pressure. These changes and additions speeded the data acquisition and improved the sample life.

III. CONTAMINATION MEASUREMENTS

A major goal of this research was to make photoelectric and optical measurements upon clean films of free-electron-like metals. It became obvious in the beginning of the study that time dependent changes occurred in the optical and photoelectric properties of magnesium films so these changes were studied carefully. The photoelectric yield decreased with time below 7.5 eV and increased with time above 8.5 eV. The number of low energy electrons grew with increasing time for photoelectrons excited with photons of energy greater than 8.5 eV. The width of the photoelectron energy distributions increased with time.

All of the phenomena described above can be explained by the growth of a thin insulating substance [such as MgO or $Mg(OH)_2$] with a band gap of ~ 8 eV upon the surface. Above ~ 8.5 eV electrons emitted from the insulator contribute to the increased yield and to the low energy peak in the energy distributions while below ~ 7.5 eV the insulator attenuates the electrons from the metal and the yield is suppressed. The increase in the width of the energy distribution curves is due to the lowering of the work function of the surface by the contaminant.

IV. REFLECTANCE, YIELD AND ENERGY DISTRIBUTION MEASUREMENTS

Near-normal incidence reflectance measurements were made on magnesium in the spectran range $2 \leq h\nu \leq 12$ eV. The data were analyzed

in terms of the Drude model and the surface plasmon absorption and diffuse scattering theories of Elson and Ritchie (1970; 1971). The reflectance was found to fit the Drude model except in the 6-8 eV region where a prominent dip in the reflectance occurred. This dip was analyzed with the Elson and Ritchie (1970; 1971) surface plasmon absorption and diffuse scatter theories. We found that the rms roughness and the autocorrelation length (an indication of the extent of surface roughness structures) increased with increasing film thickness for films in the 400 to 1000 Å thickness region.

Absolute yield measurements were made on magnesium films in the 6 to 12 eV region. The yield data exhibited a strong peak centered just below the surface plasmon energy. This peak is attributed to surface plasmon → one electron transitions.

Electron energy distribution measurements were made on magnesium in the 7.5 - 15 eV range. The lower energy distributions had shapes reminiscent of the expected parabolic density of states of magnesium while energy distributions taken at higher energies were dominated by large numbers of scattered electrons. No structure corresponding to discrete energy losses was identified. This should not be construed to mean that discrete energy losses do not take place in magnesium but rather that if they occur, they are obscured by the continuous distribution of low energy electrons arising from electron-electron scattering.

V. ATTENUATION LENGTHS

Experimental electron attenuation lengths were obtained for magnesium in the 5-11 eV range for aluminum in the 11-19 eV range by analyzing the photoelectric yield, reflectance and energy distribution data. In addition, measurements of the relative yield of aluminum as a function of angle were analyzed to obtain the attenuation length for all electrons emitted by 21.2 eV photons. This measurement provided the first confirmation of the recent theory of Pepper (1970).

Reasonable agreement with theory was found for the attenuation length measurements provided the energy of the exciting radiation was well removed from the surface plasmon energy of the metal under study. For photon energies near the surface plasmon energy, photon → surface plasmon → one electron transitions augmented the yield and led to attenuation lengths which appeared too large. We conclude that while photoelectric methods for obtaining electron attenuation lengths are useful, extreme care must be used in interpreting photoemission data taken with photons whose energies are near the surface plasmon energy.

VI. PHOTOELECTRIC MANIFESTATION OF THE OPTICAL PLASMA RESONANCE

Photoelectric yield measurements taken on a thin film ($\sim$ 200 Å) of magnesium were analyzed to obtain the bulk plasma energy of magnesium.

We found the plasma energy to be 10.46 eV by this method which compares favorably with the 10.5 found by fitting the reflectance to the Drude model.

VII. EXO-ELECTRON EMISSION FROM MAGNESIUM

It was found that a fresh magnesium surface will emit electrons in the absence of light when exposed to low pressures of oxygen or water vapor. The emission reaches a maximum in times comparable with calculated monolayer formation times of the gas and subsequently decays. We have concluded that the energy to excite the electrons over the surface barrier is derived from the chemical reaction of the magnesium with the adsorbed gas and that, for a given pressure, the emission rate is controlled by the height of the surface barrier and by the amount of magnesium available for reaction. This discussion is given in an appendix.

BIBLIOGRAPHY

BIBLIOGRAPHY

Baer, Y., P. F. Heden, J. Hedman, M. Klasson, and C. Nordling, Solid State Comm. 8, 1479 (1970).

Becker, K., Principles of TSEE Dosimetry, IAEA Atomic Energy Review 8, No. 1 (1970).

Bennett, H. E., and J. O. Porteus, J. Opt. Soc. Am. 51, 123 (1961).

Berglund, C. N., and W. E. Spicer, Phys. Rev. 136, A1030 (1964a).

Berglund, C. N., and W. E. Spicer, Rev. Sci. Instr. 35, 1665 (1964b).

Birkhoff, R. D., in Physical Processes in Radiation Biology, Leroy G. Augenstein, ed., p. 145, Academic Press, New York (1964).

Braundmeier, A. J., E. T. Arakawa, and M. W. Williams, Oak Ridge National Laboratory Report ORNL-TM-3158, 1970a (unpublished).

Braundmeier, A. J., E. T. Arakawa, and M. W. Williams, Phys. Letters 32A, 241 (1970b).

Callcott, T. A., and A. U. MacRae, Phys. Rev. 178, 966 (1969).

Cashman, R. J., and W. S. Huxford, Phys. Rev. 48, 734 (1935).

Collins, R. E., and L. W. Davies, Appl. Phys. Letters 2, 213 (1963).

Conrad, M. A., and S. Levy, Nature 189, 887 (1961).

Crowell, J., and R. H. Ritchie, J. Opt. Soc. Am. 60, 794 (1970).

Daude, A., M. Priol, and S. Robin, C. R. Acad. Sc. Paris 264, 1489 (1967).

Daude, A., A. Savary, G. Jezequel, and S. Robin, Optics Comm. 1, 237 (1969).

Delchar, T. A., J. Appl. Phys. 38, 2403 (1967).

Denisoff, A. K., and O. W. Richardson, Proc. Roy. Soc. A150, 495 (1935).

DiStefano, T. H., and D. T. Pierce, Rev. Sci. Instr. 41, 180 (1970).

Eden, R. C., Rev. Sci. Instr. 41, 252 (1970).

Eastman, D. E., J. Appl. Phys. 40, 1387 (1969).

Eastman, E. D., Solid State Comm. 8, 41 (1970).

Eastman, D. E., in Techniques of Metals Research VI, E. Passaglia, ed., Interscience, New York (1971).

Ehrlich, G., private communication (1969).

Elson, J. M., and R. H. Ritchie, Phys. Rev. Letters 33A, 255 (1970).

Elson, J. M., and Ritchie, Phys. Rev., to be published (1971).

Endriz, J., Stanford Electronics Laboratory Technical Report No. 5207-3, Stanford University, 1970 (unpublished).

Endriz, J. G., and W. E. Spicer, to be published (1971a).

Endriz, J. G., and W. E. Spicer, to be published (1971b).

Feuerbacher, B. P., and W. Steinmann, Optics Comm. 1, 81 (1969).

Feuerbacher, B. P., R. B. Bodwin, and M. Skibowski, Z. Physik 224, 172 (1969).

Feuerbacher, B., and B. Fitton, Phys. Rev. Letters 24, 499 (1970).

Fintelmann, D., Fourth Czechoslovak Conference on Electronics and Vacuum Physics, Transactions, Prague 1968.

Fowler, R. H., Phys. Rev. 38, 45 (1931).

Gesell, T. F., E. T. Arakawa, and T. A. Callcott, Surface Sci. 20, 174 (1970).

Gesell, T. F., and E. T. Arakawa, Phys. Rev. Letters 26, 377 (1971).

Grant, D., and R. H. Ritchie, Bull. Am. Phys. Soc. 15, 1356 Abstract DE14 (1970).

Grunberg, L., Brit. J. Appl. Phys. 9, 85 (1958).

Hamm, R. N., R. H. Ritchie, and J. C. Ashley, Oak Ridge National Laboratory Report ORNL-TM-2072, 1968 (unpublished).

Hoenig, S. A., and R. A. Pope, Appl. Phys. Letters 14, 271 (1969).

Holland, L., Vacuum Deposition of Thin Films, p. 111, Chapman and Hall, Ltd., London (1956).

Holland, L., The Properties of Glass Surfaces, Chapter 5, John Wiley and Sons, Inc., New York (1964).

Ives, H. E., and H. B. Briggs, J. Opt. Soc. Am. 26, 247 (1936).

Jasperson, S. N., and S. E. Schnatterly, Bull. Am. Phys. Soc. 12, 399 (1967).

Kane, E. O., Phys. Rev. 159, 624 (1967).

Kanter, H., Phys. Rev. B1, 522 (1970).

Ketterson, J. B., and R. W. Stark, Phys. Rev. 156, 748 (1967).

Kleinman, L., Phys. Rev. to be published (1971).

Kliewer, K. L., and R. Fuchs, Phys. Rev. 153, 498 (1967).

Krolikowski, W. F., Stanford Electronics Laboratories Technical Report No. 5218-1, Stanford University, 1967 (unpublished).

Krolikowski, W. F., and W. E. Spicer, Phys. Rev. 185, 882 (1969).

Krolikowski, W. F., and W. E. Spicer, Phys. Rev. B1, 478 (1970).

Lohff, J., and H. Raether, Z. Phys. 142, 310 (1955).

Madden, R. P., L. R. Canfield, and G. Hass, J. Opt. Soc. Am. 53, 620 (1962).

Mahan, G. D., Phys. Rev. Letters 24, 1068 (1970).

Markstein, G. H., in Eleventh Symposium on Combustion, p. 219, The Combustion Institute, Pittsburg (1967).

McConnell, W. J., R. D. Birkhoff, R. N. Hamm, and R. H. Ritchie, Rad. Res. 33, 216 (1968).

Mitchell, K., Proc. Roy. Soc. (London) A146, 442 (1934).

Mitchell, K., Proc. Roy. Soc. (London) 153, 513 (1936).

Mueller, H. J., U. S. Army Eng. R. and D. Labs. Res. Dept. ERDL 1704RR (20 Dec. 1961).

Ngai, K. L., E. N. Economou, and M. H. Cohen, Phys. Rev. Letters 24, 61 (1970).

Pepper, S. V., J. Opt. Soc. Am. 60, 805 (1970).

Piepenbring, F. J., in Optical Properties and Electronic Structure of Metals and Alloys, p. 316, F. Abeles, ed., North-Holland, Amsterdam (1966).

Pong, W., R. Sumida, and G. Moore, J. Appl. Phys. 41, 1869 (1970).

Quinn, J. J., Phys. Rev. 126, 1453 (1962).

Quinn, J. J., Appl. Phys. Letters 2, 167 (1963).

Raether, H., in Springer Tracts in Modern Physics, Vol. 38, p. 84, Springer, Berlin (1965).

Ramsey, J. A., and G. F. S. Garlick, Brit. J. Appl. Phys. 15, 1353 (1964).

Ramsey, J. A., J. Aust. Inst. of Metals 10, 323 (1965).

Ramsey, J. A., J. Appl. Phys. 37, 452 (1966).

Ramsey, J. A., Surface Sci. 8, 313 (1967).

Ritchie, R. H., F. W. Garber, M. Y. Nakai, and R. D. Birkhoff, "Low-Energy Electron Mean Free Paths in Solids," in Advances in Radiation Biology, vol. 3, L. G. Augenstein, R. Mason, and Max Zelle, eds., Academic Press, New York (1969).

Ritchie, R. H., and J. C. Ashley, J. Phys. Chem. Solids 26, 1689 (1965).

Samson, J. A. R., Techniques of Vacuum Ultraviolet Spectroscopy, p. 200, John Wiley and Sons, Inc., New York (1967).

Semov, Y. I., Ukrainskii Fizicheskii Zhurnal 13, 1751 (1968). Translation: Ukranian Phys. J. 13, 1249 (1969).

Simoi, C., I. Hrianca, and P. Craciun, Phys. Stat. Sol. 29, 761 (1968).

Smith, N. V., and W. E. Spicer, Phys. Rev. 188, 593 (1969).

Spencer, L. V., and U. Fano, Phys. Rev. 93, 1172 (1954).

Spicer, W. E., Phys. Rev., 112, 114 (1958).

Stanford, J. L., E. T. Arakawa, and R. D. Birkhoff, Oak Ridge National Laboratory Report, ORNL-TM-1392, 1966 (unpublished).

Stanford, J. L., H. E. Bennett, J. M. Bennett, E. J. Ashley, and E. T. Arakawa, Bull. Am. Phys. Soc. 13, 989 (1968).

Stanford, J. L., private communication (1970).

Steinmann, W., Phys. Stat. Sol. 28, 437 (1968).

Stern, E. A., and R. A. Ferrell, Phys. Rev. 120, 130 (1960).

Stuart, R. N., and F. Wooten, Phys. Rev. 156, 364 (1967).

Sutton, L., Phys. Rev. Letters 24, 386 (1970).

Sze, S. M., J. L. Moll, and T. Sugano, Solid State Electronics 7, 509 (1964).

Thomas, H., Z. Physik 147, 395 (1957).

Thomas, H., in Basic Problems in Thin Film Physics, p. 307, R. Niedermayer and H. Mayer, eds., Vandenhoeck and Ruprecht, Gottingen, Germany (1965).

Vehse, R. C., and E. T. Arakawa, Oak Ridge National Laboratory Report ORNL-TM-2240, 1968 (unpublished).

Von Voss, W. D., and F. R. Brotzen, J. Appl. Phys. 30, 1639 (1959).

Watson, L. M., R. K. Dimond, and D. J. Fabian, Soft X-Ray Band Spectra, p. 45, D. J. Fabian, ed., Academic Press, London (1968).

Weast, R. L., ed., Handbook of Chemistry and Physics, 46th Edition, p. D-24, Chemical Rubber Co., Cleveland (1965).

Wilems, R. E., and R. H. Ritchie, Oak Ridge National Laboratory Report ORNL-TM-2101, 1968 (unpublished).

Williams, M. W., E. T. Arakawa, and L. C. Emerson, Surface Sci. 6, 127 (1967).

Williams, M. W., and E. T. Arakawa, J. Appl. Phys. 38, 1272 (1967).

Wolf, P. A., Phys. Rev. 95, 56 (1954).

Wooten, F., T. Huen, and R. N. Stuart, in Optical Properties and Electronic Structure of Metals and Alloys, p. 333, F. Abeles, ed., North-Holland, Amsterdam (1966).

APPENDIX

APPENDIX

EXO-ELECTRON EMISSION DURING OXYGEN AND WATER VAPOR CHEMISORPTION ON FRESH MAGNESIUM SURFACES

During the course of work function measurements on vacuum evaporated magnesium films a liquid nitrogen cold trap warmed up. Subsequently, a current was observed from the film in the complete absence of light. This phenomenon which has been identified as chemiemission was investigated and the results published (Gesell et al., 1970). The following is an expanded version of the published account.

The term exo-electron emission has been applied to a small electron current from a solid when the process supplying the energy to excite internal electrons over the surface barrier is clearly not related to external stimuli such as is the case with photoemission, secondary emission, field emission, or thermionic emission. Four reviews of exo-electron emission phenomena exist in English (Grunberg, 1958; Mueller, 1961; Ramsey, 1965; Becker, 1970). The very small emission currents of 10^{-17} to 10^{-15} amperes/cm^2 reported have usually been measured using particle counting techniques. The single exception to this is the early work of Richardson and several co-workers, all of which is referenced by Denisoff and Richardson (1935). Richardson and co-workers reported current densities as high as 10^{-8} amperes/cm^2 from liquid alkali metal alloys exposed to certain halogens

and halogen compounds. Phase changes, annealing of mechanical damage following abrasion or evaporation, surface adsorption reactions and thermal release of trapped electrons have all been cited as processes supplying energy to the escaping electrons. For metals, some authors have attributed most published results to low levels of photoemission from stray light (Ramsey, 1966; Conrad and Levy, 1961; Semov, 1969) but others claim small currents in the absence of light (Simoi et al., 1968; Von Voss and Brotzen, 1959; Fintelmann, 1968). For metals it is well established that exo-electron emission is strongly dependent upon the type and pressure of the background gas in which the sample is immersed (Hoenig and Pope, 1969; Ramsey, 1966; 1967). This dependence can reflect either the effect of the gases on the height of the surface barrier, measured by the work function, or their effect on adsoprtion reaction rates driving the emission process, or both.

We have found exo-electron emission currents as high as 2×10^{-11} amperes/cm^2. They were obtained by exposing a fresh magnesium surface prepared by abrading a bulk specimen to water vapor or oxygen in the range from 5×10^{-10} to 1×10^{-6} Torr partial pressure. Similar results were found when a vacuum evaporated film was used for a sample. We conclude on the basis of the experiments described below that energy given to the excited electrons is derived from the reaction of O_2 or H_2O with a freshly exposed magnesium surface. These currents arise when highly energetic reactions occur on a surface with a very low work function. Such surfaces, with work functions of about 1.8 eV are attained at approximate monolayer coverages of oxygen or perhaps of OH or H_2O on magnesium.

The experiments were performed in complete darkness and at room temperature in a liquid nitrogen trapped, valveless stainless steel vacuum system pumped with a four inch oil diffusion pump using Dow Corning 705 and capable of 1.5×10^{-8} Torr without baking. The apparatus is shown schematically in Figure 42. The sample area was about 5 cm^2. The electrons were collected at + 8 volts on a seven inch diameter stainless steel grid. The current was measured with a Keithley 417 picoammeter connected directly to the sample. To make a measurement, the partial pressure was set by admitting the desired gas via a high vacuum leak valve while monitoring the total pressure with an ionization gauge connected to a strip-chart recorder. The difference in total pressure was taken as a reasonable measure of the partial pressure of the added gas. The ionization gauge was then turned off and covered with a light tight cover. The fresh surface was prepared by either vacuum evaporation (from a tungsten filament) or by abrading a bulk sample for ten seconds with a stainless steel wire brush operated through a rotary feedthrough. Following evaporation or abrasion, the picoammeter and recorder were switched on to record the current. Current versus time curves taken at the same pressure were quite reproducible.

Figure 43 shows the time development of the exo-electron emission of abraded magnesium exposed to various partial pressures of oxygen. The two maxima in the exo-electron current for the intermediate pressures indicate that the process is not a simple one. It is possible, however, that the second maximum is due to water vapor contamination in the vacuum system.

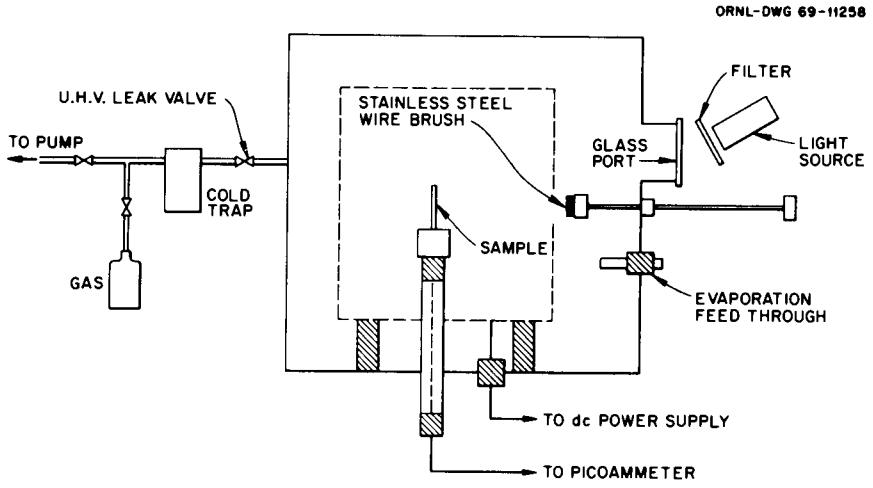

Figure 42. Side view of the experimental apparatus used for exo-electron emission studies.

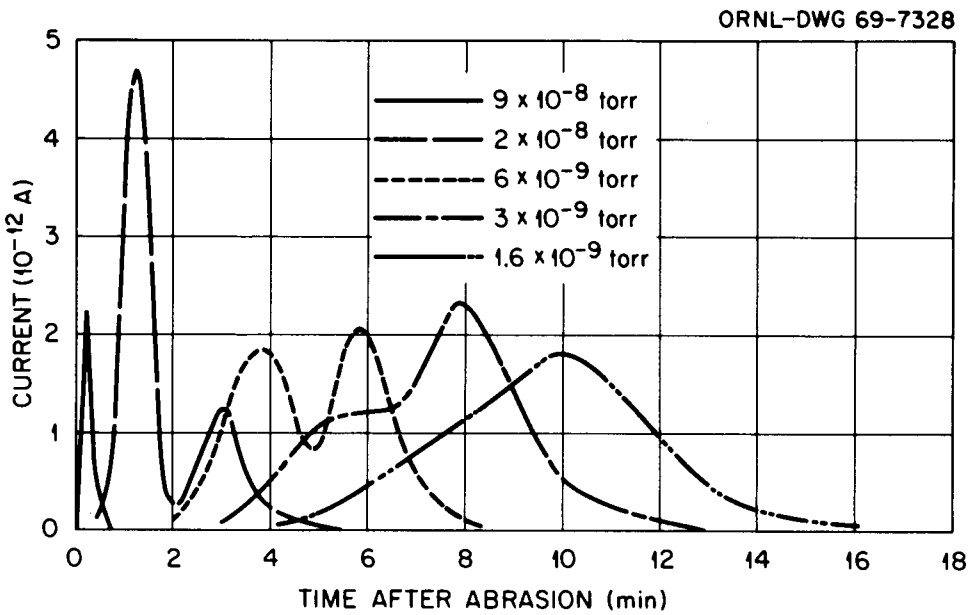

Figure 43. Time development of exo-electron emission from magnesium in the presence of oxygen for various pressures.

In separate experiments we have measured the photoelectric work function of the abraded sample by shining slowly chopped, filtered light onto the sample during the course of the electron emission and observing the threshold for photoemission as a function of wavelength. We were not able to use the more sensitive Fowler (1931) method because the work function changed too rapidly. This experiment was performed in the same fashion as the exo-electron emission experiments described previously except for the addition of the chopped filtered light. The data were recorded on the strip chart recorder and took the form of a series of steps. The top of the steps represented the sum of the photoemission and exo-electron currents, and the bottom of the steps represented the exo-electron current. The difference between the steps represented the photoelectric current. The experiment was repeated many times at the same pressure but with different optical filters. The results of this experiment are shown in Figure 44. The top curve shows the work function, as determined by the onset of photoemission, as a function of time while the lower curves show the photoemission for a photon energy of $1.93 \pm .05$ eV and the exo-electron emission as functions of time. These measurements show that the photoelectric work function drops to 1.8 eV during the course of the emission and rises as the emission decreases. The second maximum in the emission during oxygen exposure at certain pressures may be augmented by work function changes since the measurements indicate that the photoelectric work function goes through two minima, the second of which corresponds to the second exo-electron emission maximum. It was

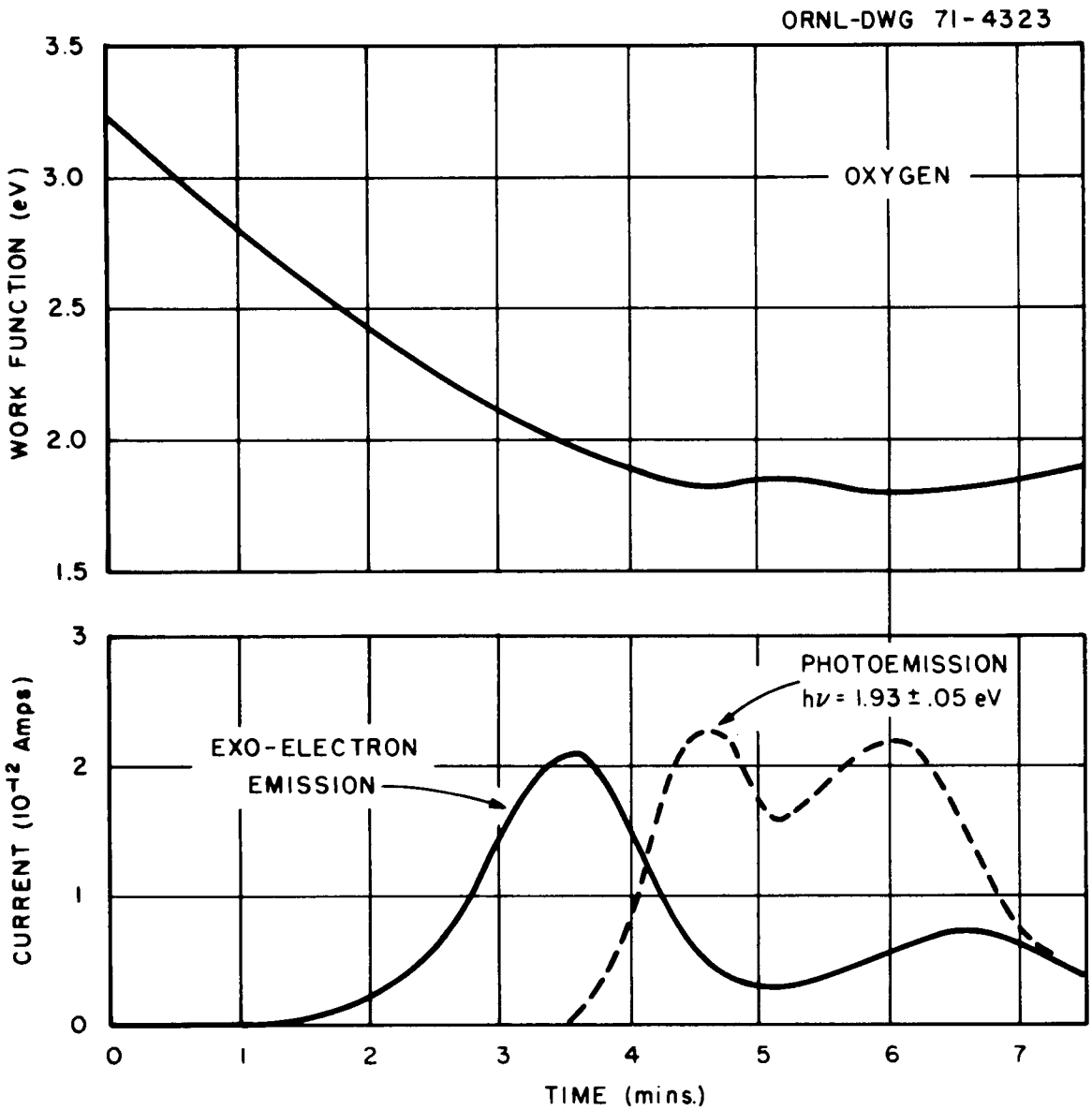

Figure 44. Time development of the work function and the exo-electron emission and of the photoemission ($h\nu = 1.93 \pm .05$ eV) from a fresh magnesium surface.

reported by Cashman and Huxford (1935) that the work function of a freshly evaporated magnesium film changed in time from 3.6 to 2.2 eV and subsequently rose when exposed to "trace amounts" of oxygen.

The maxima in the emission occur at times which are close to monolayer formation times calculated assuming a unit sticking coefficient. Figure 45 shows the calculated monolayer formation time for oxygen as a function of pressure together with data which show the position in time of the first peak in the oxygen exo-electron emission curve as a function of pressure. The solid points are the actual data and the open points were obtained by assuming a background partial pressure of oxygen amounting to 2×10^{-9} Torr. In either case the higher pressure points follow the shape of the monolayer line very well.

We have observed that cutting off the gas leak causes an immediate reduction (on the order of 90%) in the exo-electron emission current. Reopening the leak causes the emission to return to the previous level. This behavior is illustrated in Figure 46. The solid line shows an ordinary exo-electron emission curve. The dashed curve is the result if the oxygen is turned off where indicated and the dotted curve is the result if the oxygen leak is re-opened at the point indicated. The results indicate that the emission is governed only by the presence of the oxygen and not by special active sites whose population is independent of pressure.

Figure 47 shows the time development of the exo-electron emission of abraded magnesium exposed to various partial pressures of water vapor. For

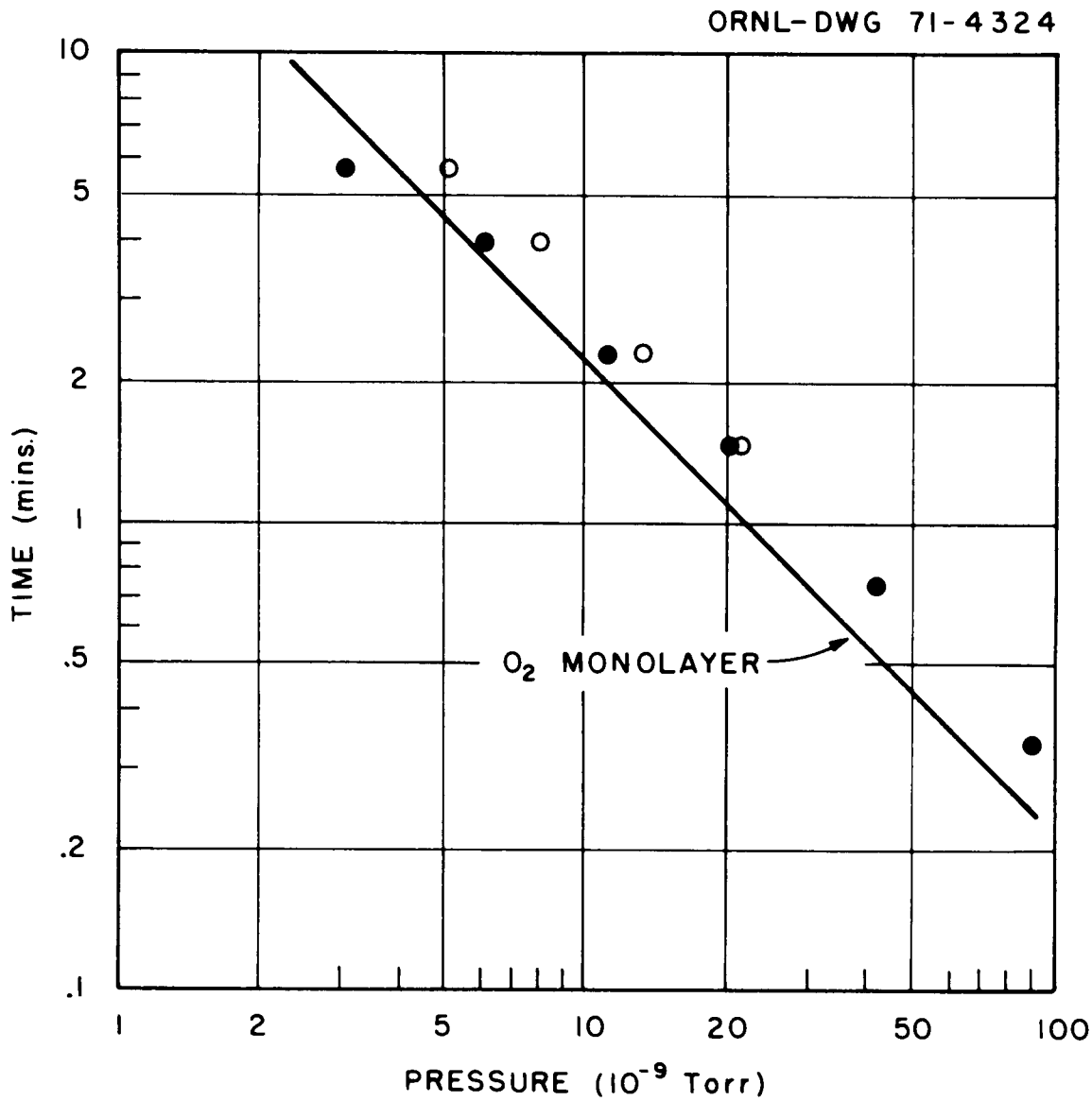

Figure 45. Time to achieve a monolayer of oxygen on a surface as a function of pressure assuming until sticking coefficient together with data which show the position in time of the first peak in the oxygen emission cruves as a function of pressure.

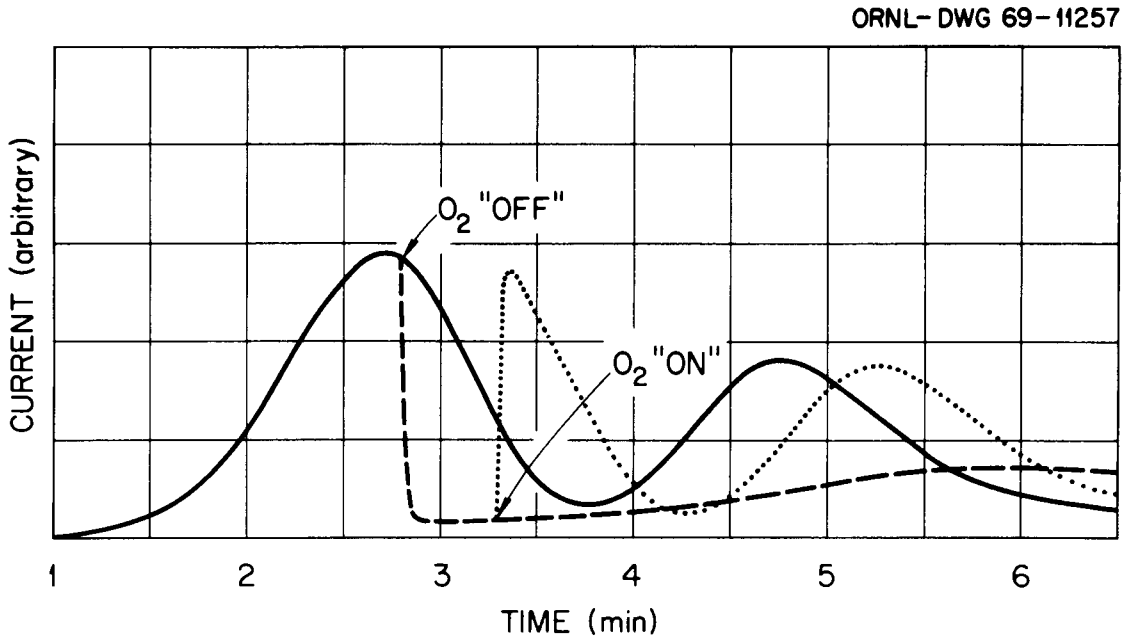

Figure 46. The effect of shutting off and reopening the oxygen leak upon the time development of exo-electron emission.

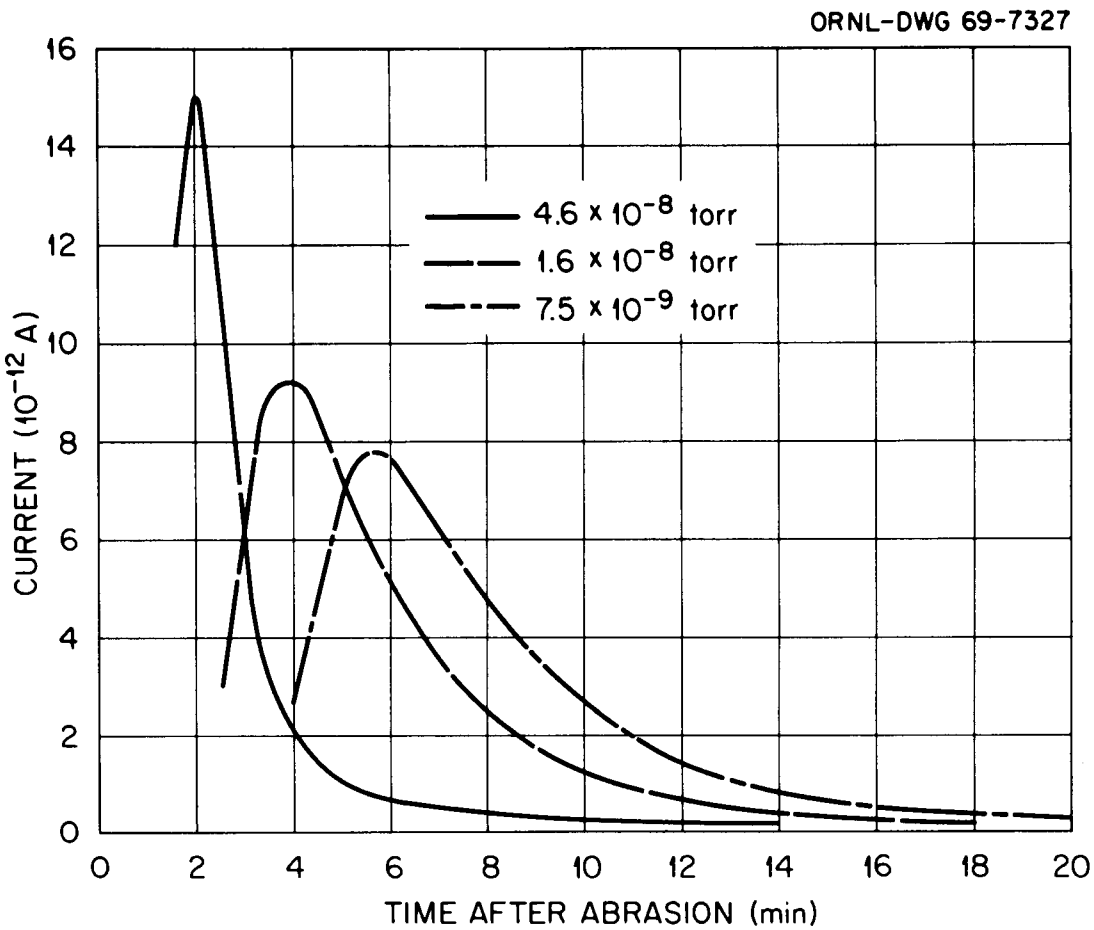

Figure 47. Time development of exo-electron emission in the presence of water vapor for various pressures.

similar pressures the exo-electron emission induced by water vapor took somewhat longer to reach a maximum and persisted longer than the emission induced by oxygen. No double maxima have been observed with water vapor.

We checked aluminum for exo-electron emission under the same experimental conditions used for magnesium and found no measurable emission. This was to be expected from previous results (Ramsey and Garlick, 1964). Several other gases were tested on magnesium. No measurable emission was found with ethanol, nitrogen, acetone, isopropyl alcohol, or hydrogen, but a small emission was found with methanol.

We have calculated the yield of the process in terms of the number of electrons ejected per molecule striking the surface. For an oxygen partial pressure of 1.1×10^{-8} Torr, the maximum yield is 1.2×10^{-6} electrons per molecule assuming 100% collection efficiency. It is interesting to note that Lohff and Raether (1955) reported exo-electron emission from vacuum evaporated magnesium in the presence of oxygen, but they used 2×10^{-5} Torr of oxygen and observed only $\sim 5 \times 10^{-17}$ amps/cm^2 for a yield of 3.7×10^{-12} electrons per incident molecule. We can speculate that most of the electrons were emitted before they turned on their particle counter. Markstein (1967) observed an electron current from a probe immersed in a burning vapor of magnesium and oxygen during combustion studies. Markstein attributed the current to the energy released from excited states during Mg-O reactions taking place on the surface of the probe. In a recent experiment under carefully controlled ultrahigh vacuum conditions, Delchar (1967) measured total

charge collected when measured bursts of oxygen were admitted to a tube containing a vacuum evaporated nickel film and reported an efficiency of 10^{-9} electrons per oxygen molecule. Delchar also observed two maxima in his electron yields which he attributed to incorporation of the oxygen into the nickel lattice.

The yield for electron ejection due to chemisorption of water on magnesium is of the same order of magnitude as the yield for chemisorption of oxygen on magnesium.

We feel that the energy for the ejection of the electrons comes from the energy released by the chemisorption of the oxygen or water molecules on the fresh magnesium surface.

Adequte energies are available from magnesium-oxygen reactions as shown by the following equations (Weast, 1965).

$$Mg + \frac{1}{2}O_2 \rightarrow MgO + (6.18\ eV)$$

$$Mg + O_2 \rightarrow MgO_2 + (6.16\ eV)$$

One possible mechanism for the electron ejection, first suggested to us by Ehrlich (1969), is that an incoming molecule is adsorbed, and then emits an Auger electron in the process of chemically uniting with Mg to form MgO.

We offer the following as a speculative explanation of the phenomenon. Assume that a clean surface exists in the presence of oxygen gas

at low pressure. Oxygen molecules strike the surface and are adsorbed. After adsorption the oxygen molecules are incorporated into the lattice (perhaps first dissociated) with a release of energy resulting in place exchange between the oxygen and the magnesium. This configuration is equivalent to a dipole layer which has the property of lowering the surface barrier. Subsequent oxygen molecules also react on the surface with a release of energy. A fraction of these reactions result in the release of an Auger electron and a fraction of these Auger electrons escape into the vacuum. The fraction of Auger electrons escaping into the vacuum is a function of the surface barrier that they must overcome; the lower the surface barrier, the greater the probability that the Auger electron will escape into the vacuum and be observed. As more and more oxygen molecules are adsorbed and incorporated into the lattice, MgO builds up which reduces the exposed magnesium surface area until eventually no current is observed. Thus the emission current is controlled by two factors, the height of the surface barrier, and the amount of exposed surface available for reaction.

The model just described can explain (qualitatively) the decrease in the surface barrier (as measured by the photoelectric threshold) and the rise and decline of the exo-electron emission current.

The double peak observed in the oxygen data, Figure 43, page 166, can be explained by the structure in the height of the surface barrier shown in Figure 44, page 168. The structure in the surface barrier is possibly due to a

reordering of the oxygen and the magnesium as a certain coverage is achieved or perhaps influenced by a contaminant in the vacuum system.

INTERNAL DISTRIBUTION

1-2. Central Research Library (CRL)
3. Document Reference Section
4-18. Laboratory Records Department
19. Laboratory Records (ORNL RC)
20. ORNL Patent Office
21-30. E. T. Arakawa
31-40. R. D. Birkhoff
41. F. L. Culler
42. L. C. Emerson
43. R. N. Hamm
44. J. L. Liverman
45-46. K. Z. Morgan
47. R. H. Ritchie
48. W. S. Snyder
49. A. M. Weinberg
50. J. E. Cantlon (consultant)
51. C. D. Cooper (consultant)
52. J. C. Frye (consultant)
53. E. Gerjuoy (consultant)
54. J. B. Hursh (consultant)
55. J. L. Magee (consultant)
56. M. R. Williams (consultant)
57. H. O. Wyckoff (consultant)

EXTERNAL DISTRIBUTION

58. F. Abeles, Institute d'Optique, 3, Blvd. Pasteur, Paris, France.
59. N. Axelrod, Bell Telephone Laboratories, Murray Hill, N.J. 07971.
60. G. Arnett, Space Sciences Laboratory, SNE-SSL-TR, George C. Marshall Space Flight Center, Huntsville, Alabama 35812.
61. H. E. Bennett, Physics Optics Branch, Michelson Laboratory, U.S. Naval Ordnance Test Station, China Lake, California 94108.
62. H. Boersch, I. Physikalischen Institut der Technischen Universitat, Berlin, West Germany.
63. A. J. Brauncmeier, Faculty of Physics, Southern Illinois University, Edwardsville, Illinois, 62025.
64. A. Bril, Phillips Eindhoven Project Department, Phillips Laboratory, Eindhoven, Netherlands.
65. W. M. Bugg, Dept. of Physics, University of Tennessee, Knoxville, Tennessee 37916.
66. T. A. Callcott, Physics Department, University of Tennessee, Knoxville, Tennessee 37916.
67. N. Damany, CNRS, 1, Place Aristide-Briand, Bellevue, France.
68. C. B. Duke, University of Illinois, Dept. of Physics, Urbana, Illinois.
69. J. Endriz, University of Linkoping, Department of Physics, S-581 83 Linkoping, Sweden.
70. B. Feuerbacher, Surface Physics, ESTEC, Nordwijke, Holland.
71. B. Fitton, Surface Physics, ESTEC, Nordwijke, Holland.
72. J. C. Garth, Radiation Effects Branch, Solid State Sciences Laboratory, AFCRL, L. G. Hanscom Field, Bedford, Massachusetts 01730.
73-97. T. F. Gesell, University of Texas at Houston, School of Public Health, P. O. Box 20186, Houston, Texas 77025.
98. R. Haensel, Physikalisches Staatsinstitut, II. Institut fur Experimental-Physik, der Universitat Hamburg, Hamburg 50, Lurper Chaussee 149, West Germany.

99. H. D. Hagstrum, Bell Telephone Laboratories, Murray Hill, New Jersey 07971.
100. W. R. Hunter, U. S. Naval Research Laboratory, Washington, D.C. 20390.
101. P. A. Kittle, Rohm and Hass Corporation, Philadelphia, Penn.
102. R. Y. Koyama, National Bureau of Standards, Washington, D.C. 20234.
103. R. J. Lovell, Physics Department, University of Tennessee, Knoxville, Tennessee 37916.
104. R. P. Madden, Far UV Physics, Division 222, National Bureau of Standards, Washington, D.C. 20234.
105. K. P. Miyake, Institute for Optical Research, Kyoiku University, Tokyo, Japan.
106. A. H. Nielsen, College of Liberal Arts, University of Tennessee, Knoxville, Tennessee 37916.
107. P.O. Nilsson, Chalmers University of Technology, Department of Physics, Gibraltargatan 5B, Gotenberg, S Sweden.
108. A. Otto, II. Physikalisches Institute der Universitat Munchen, Munich, West Germany.
109. S. V. Pepper, Lewis Research Center, NASA, Cleveland, Ohio 44135.
110. W. Pong, Dept. of Physics and Astronomy, Univ. of Hawaii, Honolulu, Hawaii 96822.
111. C. J. Powell, Electron Physics Section, National Bureau of Standards, Washington, D.C. 20234.
112. H. Raether, Institute fur Angewandte Physik, Universitat Hamburg, Hamburg, Germany.
113. Mme. S. Robin, Laboratoire de Spectroscopie, Faculte des Sciences, Avenue du General Leclerc, 35 Rennes, France.
114. Mme. S. Robin-Kandare, Faculte desSciences, Laboratoire de Physique, 34-Montepelier, France.
115. T. Sasaki, University of Tokyo, College of General Education, Komaba, Tokyo, Japan.
116. G. Sauerbrey, Physikalisch-Technische Bundensanstalt, Berlin-Charlottenburg, Germany.
117. S. E. Schnatterly, Department of Physics, Palmer Physical Laboratory, Princeton University, P.O. Box 708, Princeton, New Jersey 08540.
118. L. Skolil, Dept. of Physics, San Diego State College, San Diego, Calif.
119. W. E. Spicer, Stanford Electronics Lab., Stanford Univ., Stanford, California 94305.
120. J. L. Stanford, J.S. Naval Testing Station, China Lake, Calif. 93555.
121. W. Steinmann, Section Physik der Universitat Munchen, Munich, Germany.
122. J. R. Stevenson, Phys. Dept., Georgia Inst. of Technol., Atlanta, Ga. 30332.
123. J. B. Swan, Department of Physics, University of Western Australia, Nedlands, Western Australia.
124. W. N. Unertl, Univ. of Wisconsin, Dept. of Physics, Madison, Wisconsin.
125. R. C. Vehse, Bell Telephone Labs., P.O. Box 241, Reading, Pa. 19603.
126. G. L. Weissler, Univ.of Southern California, Dept. of Physics, Los Angeles, California 90007.
127. F. T. Wooten, Lawrence Radiation Lab., University of Calif, Berkeley, California 94720.
128. Laboratory and University Division, AEC, ORO.
129-130. Division of Technical Information Extension, ORO.